

https://dspace.org/

Thermo-mechanical behaviour of rocks from the Busveld Igneous Complex with relevance to deeper mining

Oniyide, Gafar

2016
http://hdl.handle.net/10539/20030

Downloaded from a DSpace repository. https://dspace.org/

THERMO-MECHANICAL BEHAVIOUR OF ROCKS FROM THE BUSHVELD IGNEOUS COMPLEX WITH RELEVANCE TO DEEPER MINING

Gafar Oniyide

A thesis submitted to the Faculty of Engineering and the Built Environment, University of the Witwatersrand, Johannesburg, in fulfilment of the requirements for the degree of Doctor of Philosophy.

Johannesburg, 2015

DECLARATION

I, Gafar Oniyide, declare that this thesis is my own unaided work. Where use has been made of the work of others, it has been duly acknowledged. It is being submitted for the Degree of Doctor of Philosophy in the University of the Witwatersrand, Johannesburg. It has not been submitted before in any form for any degree or examination in any other University.



Gafar Oniyide

6th day of October 2015

ABSTRACT

The Bushveld Igneous Complex (BIC) is the world's largest layered igneous intrusion. It is about seven to nine kilometers thick and divided into eastern, western and northern limbs. Its upper critical zone hosts the world's largest deposit of platinum group elements (PGE). The Merensky Reef has been traced for 300 km around the entire outcrop of the eastern and western limbs of the BIC, and to depths of 5 km and beyond. The temperature gradient of the BIC approximately doubles that of the Witwatersrand Basin, which makes the platinum mines face more heat challenges with increasing depth of mining than their counterparts in the gold mines. Rock lithology at great depth are subjected to high virgin temperatures and stresses before mining. The air temperature reduces down to around 27 to 30°C for workers' comfort, while exposed rock surface would still have higher temperatures than the mine air. The response of rock to temperature variation, coupled with increased in-situ stresses, may pose serious challenges to the future of platinum mining in South Africa.

From the literature survey, it has been established that variation in temperature has influence on the behaviour of rocks. These effects have been studied for cases of underground fire accidents, thermal repositories, geothermal intrusions and underground storage caverns. The question as to what would be the influence of virgin rock temperature on the behaviour of rock and the stability of underground openings, particularly those located in areas of high geothermal gradient remains unanswered. This thesis presents the results of investigation on the response of rocks, particularly from BIC, to variation of temperature from rock engineering point of view through laboratory, microscopic and numerical analyses.

The uniaxial and triaxial compression testing of the specimens at various temperatures were carried out using MTS 793 servo-controlled testing machine. The results of the laboratory testing revealed that increase in temperature led to reduction in the Young's modulus and peak strength of the rocks and increase in the coefficient of thermal expansion as well as dilation angle. From the Young's modulus and yield strength, determined in the laboratory, relationship between Young's modulus, temperature and strength versus temperature, were developed.

The microscopic analyses examine the effect of heat on rocks from the BIC, in terms of initiation or extension of micro-cracks in the rock structure and changes in their chemical composition. Optical and scanning electron microscopes were used for image capturing. The results of the optical microscope analyses show that there are some physical changes observed on the rocks subjected to heat treatment, however, the observed changes are not significant. The scanning electron microscope images revealed that crack initiation starts at lower temperature and extends with increasing temperature. The chemical analyses of the specimen show that the temperature range considered for this research is not high enough to induce chemical changes in the specimens.

The numerical analyses looked into the effect of temperature on the behaviour of underground excavations by considering variation of temperature and in-situ stresses with increasing mining depth. Comparisons were made for mining at depths of 1073, 2835 and 5038 m below surface. The general observation is that the increase in the in-situ stress and temperature led to higher scale of failure around the excavation with corresponding depth increase. At depth of 1073 m, there was no observation of shear and tensile failure. At depth of 2835 m, shear and tensile failure became evidenced in the state, convergence and failure plots. The tensile and shear failures at depth of 5038 m is quite high due to the high temperature and in-situ stresses. There were increases in the magnitudes of the horizontal and vertical convergence at this depth. Recommendations were made on appropriate support systems that would suit the rock behaviour at deep mining levels.

A sensitivity analysis was done to evaluate the influence of increasing temperature on failure. This was achieved by assigning the temperature (50°C) and thermal properties for 1073 m below surface to depth of 5038 m. Similarly, temperature (140°C) and the thermal properties of 5038 m was assigned to 1073 m, while keeping the in-situ stresses and all other modelling parameters constant. Reduction of temperature and thermal properties at 5038 m resulted in the reduction of the extent of tensile and shear failures. The reverse was observed at 1073 m due to temperature increase. Generally, the numerical modelling revealed that the extent of tensile failure is a function of excavation geometry, temperature and in-situ stresses.

ACKNOWLEDGEMENTS

I am greatly indebted to my supervisor, Dr. H. Yilmaz for his invaluable contributions, guidance and time towards the successful completion of this research. I also express my appreciation to Prof. T. R. Stacey for his contribution and advice during the stage of conceptualizing this research. Prof F. Cawood (Head, School of Mining Engineering, University of the Witwatersrand) is much appreciated for the funding received during the course of the research. I am grateful to Prof. Aly Karam (Deputy Dean, Research, Faculty of Engineering and Built Environment, University of the Witwatersrand) for his intervention when I was at crossroad. The invitation for collaborative research given by Prof. E. Nordlund (Division of Mining and Geotechnical Engineering, Luleå University of Technology, Sweden) for the numerical modelling aspect of this research is acknowledged.

I thank Mr. G. Priest (Anglo Platinum), Mr. T. Muzondo, (Anglo Platinum, Mogalakwena mine), S. Mampa (Anglo Platinum, Siphumelele mine), Mrs. F. Steven (Anglo Platinum, Khomanani mine), Mr K. Le Bron (Bafokeng Rasimone Platinum mine) for supplying rock samples, in-situ stress measurements and data on virgin rock temperature. I appreciate my late father, who passed away during the course of this research. I thank my mother, wife and children for their support and patience since the inception of the programme.

DEDICATION

To Almighty God and my late father, Mr. Aliu Oniyide.

CONTENTS

DECLARATION.....I
ABSTRACT II
ACKNOWLEDGEMENTS IV
DEDICATION.....V
CONTENTS VI
LIST OF FIGURES.....IX
LIST OF TABLES XX
LIST OF SYMBOLS AND ACRONYMS.....XXII

CHAPTER ONE.....1

1.0 INTRODUCTION.....1

1.1 Study Area.....1

1.2 Problem statement.....2

1.3 Objectives of the research.....3

1.4 Research methodology.....4

1.5 Scope of the research and limitations.....5

1.6 Content of the thesis.....6

CHAPTER TWO.....7

2.0 LITERATURE REVIEW.....7

2.1 The Bushveld Igneous Complex (BIC) 9

2.2 Factors influencing the behaviour and mechanical properties of rock.....18

2.3 Thermal properties of rocks.....38

2.4 Review of laboratory test methods for rocks applicable in this research.....48

2.5 Class I and Class II post-peak behaviour of rocks.....56

2.6 Measurement of coefficient of thermal expansion.....60

2.7 Determination of dilation angles (ψ) from laboratory triaxial test.....61

2.8 Measurement of P- and S-wave velocities.....69

2.9 Prediction of depth of brittle failure.....75

2.10 Discussion.....78

2.11 Chapter Summary.....79

CHAPTER THREE.....81

3.0 LABORATORY TESTS.....81

3.1 Rock samples and their sources.....81

3.2 Brazilian (Indirect tensile) test.....84
3.3 Compressive strength testing using Amsler testing machine.....87
3.4 Influence of temperature on Young's modulus and strength.....107
3.5 Effect of temperature on cohesion and angle of internal friction.....114
3.6 The determination unconfined Coefficient of Linear Thermal Expansion (CLTE).115
3.7 Dilations angles of BIC rocks.....121
3.8 Influence of temperature and loading on P- and S-wave velocities.....124
3.9 Chapter summary.....131
CHAPTER FOUR.....132
4.0 MICROSCOPIC ANALYSES OF ROCK SAMPLES.....132
4.1 Microscopes used for image capturing.....132
4.2 Specimen preparation.....134
4.3 Heat treatment of specimens.....136
4.5 Results of the scanning electron microscope (SEM) analysis.....142
4.6 Result of Energy-dispersive X-ray Spectrometry 148
4.7 Chapter summary.....152
CHAPTER FIVE.....153
5.0 NUMERICAL MODELLING.....153
5.1 Model input parameters.....154
5.2 FLAC 2D modelling of laboratory intact rock in triaxial testing.....156
5.3 FLAC 2D modelling of rock mass.....171
5.4 Discussion.....197
5.5 Sensitivity analysis.....202
5.6 Modelling of Circular Excavation.....204
5.7 Sensitivity analysis.....210
5.8 Chapter summary.....212
CHAPTER SIX 213
6.0 CONCLUSIONS AND RECOMMENDATIONS.....213
6.1 Conclusions.....213
6.1 Recommendations for future research.....216

REFERENCES.....218
APPENDICES.....235

LIST OF FIGURES

Figure 1.0: Map of the Bushveld Igneous Complex (Watson et al, 2010) 2

Figure 2.1: Map of the Bushveld Igneous Complex, (Cawthorn, 2010) 10

Figure 2.2: Detailed geology map of the Bushveld Igneous Complex, (Naldrett et al, 2009).....11

Figure 2.3: A comparison of the stratigraphic succession between the Merensky reef and the top chromite layer of the UG-2 in the Rustenburg (Naldrett et al, 2009).....13

Figure 2.4: Normative mineral compositions for rock samples from the Merensky and Bastard units of the Bushveld Igneous Complex (Wilson et al, 2005).....14

Figure 2.5: Photographs of units HW1 to HW5 of the Bastard reef in hand held specimen (Mitchell and Manthree, 2002) 15

Figure 2.6: stress-strain plot of Merensky reef and immediate footwall and hangingwall tested under triaxial condition (York et al, 1998). 18

Figure 2.7: Relationship between UCS and mineralogical content of some rocks (Tandon and Gupta, 2013) 20

Figure 2.8: Relationship between uniaxial compressive strength and texture coefficient for quartzite (Tandon and Gupta, 2013).....21

Figure 2.9: Influence of porosity on uniaxial compressive strength (Palchik, 2006).....22

Figure 2.10: Comparison of UCS of dry and saturated 35 British sandstones (Vásárhelyi, 2003) 23

Figure 2.11: Schematic diagram of creep deformation (adapted from Okamoto et al, 2004).....24

Figure 2.12: Effect of loading rate on the strength of tuff (Peng and Podnieks, 1972).....25

Figure 2.13: Effect of discontinuities on (a) UCS and (b) modulus of elasticity of Pendali marble blocks (Tsoutrelis and Exadaktylos, 1993).....26

Figure 2.14: Stress-strain curves during triaxial compression tests of Tournemire shale at 10 MPa confining pressure and with different temperatures (Masri et al, 2014).....27

Figure 2.15: Effect of temperature and relative humidity on strength of Hawkesbury sandstone (Smith and Pells, 2008).....32

Figure 2.16: Influence of confining pressure on Piosson's ratio (Cristensen, 1996)…..33

Figure 2.17: Influence of temperature on Piosson's ratio (Cristensen, 1996).....34

Figure 2.18: Influence of confining ($\sigma 3$) and hydraulic pressure (Pw) on strength of fine sandstone (Liu and Jin, 2014).....36

Figure 2.19: Geothermal gradient of the Witwatersrand Basin and BIC (Biffi et al, 2007)……..37

Figure 2.20: Percentage contributions of heat sources in underground mines (Payne and Mitra, 2008)..... 39

Figure 2.21: Graph of specific heat capacity against temperature (Vosteen and Schellschmidt, 2003)..... 42

Figure 2.22: Graph of thermal conductivity against temperature (Vosteen and Schellschmidt, 2003) 42

Figure 2.23: Graph of thermal diffusivity against temperature (Vosteen and Schellschmidt, 2003) 43

Figure 2.24: Influence of confining pressure on thermal expansion- when pressure was (i) decreased and (ii) increased (Wong and Brace, 1979). 45

Figure 2.25: Effect of temperature and heating rate on coefficient of thermal expansion of granite (Ramana and Sarma, 1980). 47

Figure 2.26: Apparatus for Brazilian test 49

Figure 2.27: Compression testing machines (a) MTS servo-controlled machine (b) Amsler compression machine. 50

Figure 2.28: Servo-controlled testing machine and pressure intensifier.....51

Figure 2.29: Servo-controlled machine support systems (a) Hydraulic Pump Unit (b) Servo-valves.....52

Figure 2.30: Parts of MTS servo-controlled triaxial cell.....53

Figure 2.31: Axial and circumferential extensometers attached to norite specimen – ready for testing. 55

Figure 2.32 : Complete stress-strain curves of rocks showing Class I and Class II behaviour (ISRM, 1999). 57

Figure 2.33: Illustration of the post-peak energy balance for rocks of Class I and II behaviour (Tarasov and Potvin, 2013). 58

Figure 2.34: Generic stress-strain curves for different levels of confining pressure σ3 showing (a) conventional (b) unconventional rock behaviour. (c) Typical variation of the post-peak brittleness index K with rising σ3 for rocks displaying the conventional and unconventional behaviour (Tarasov, 2014) 59

Figure 2.35: Bilinear idealization for determination of dilation angle (after Vermeer and de Borst, 1984) 62

Figure 2.36: Dilation in relation to crack initiation, growth and coalescence (Zhao and Cai, 2010a). 65

Figure 2.37: Stress-strain diagram showing crack development (Eberhardt et al.,1998).....66

Figure 2.38: Dilation angle-plastic shear strain relationship for Witwatersrand quartzite under different confining stresses (Zhao and Cai, 2010a). 68

Figure 2.39: Layout of essential components of an ultrasonic apparatus (adapted from Aydin, 2014). 70

Figure 2.40: Influence of temperature on P- and S-wave velocities (Kitamura et al, 2006)…....72

Figure 2.41: Influence of confining pressure on P- and S-wave velocities (He and Schmitt, 2006) 73

Figure 2.42 Influence of porosity on P- and S-wave velocities (Paoletti, 2012)).....73

Figure 2.43: (a) Deviatoric stress versus axial strain (b) P- and S-wave velocities versus axial strain for Etna basalt. (Fortin et al, 2011). 74

Figure 2.44: Tunnel failure modes (Martin et al, 1999).....76

Figure 3.1: Brazilian test specimen before testing.....85

Figure 3.2: Some Brazilian test specimens after testing.....85

Figure 3.4: Amsler compression testing machine.....87

Figure 3.5: Specimens with strain gauges and lead-wires…….....88

Figure 3.6: Data acquisition system (a) data acquisition and control unit (b) strain gauge amplifier. 89

Figure 3.9: Stress-strain for BRPM specimens.....90

Figure 3.14: Triaxial cell (After, Franklin and Hoek, 1970) 93

Figure 3.15: Plot of peak stresses versus confining pressures.....95

Figure 3.20: Plot of temperature versus axial stain for norite under 10 MPa confinement……...98

Figure 3.21: Plot of CLTE versus temperature for norite.....99

Figure 3.22: Screen shot of the Multi-Purpose-Testware (MPT) procedure for triaxial testing.....101

Figure 3.23: Illustration of MPT steps.....101

Figure 3.24: Norite tested at ambient temperature and various confinements.....102

Figure 3.25: Norite tested at 50 °C and various confinements.....103

Figure 3.26: Norite tested at 90°C and various confinements.....104

Figure 3.27: Norite tested at 140°C and various confinements.....105

Figure 3.28: Norite tested at 10MPa confinement and various temperatures.....106

Figure 3.29: Young's modulus and temperature relationship for various rock types.....109

Figure 3.30: Comparison of laboratory tested and calculated Young's modulus for two rocks..... 111

Figure 3.31: Strength behaviour against temperature at 10 MPa confinement.....112

Figure 3.32: Comparison of laboratory tested and calculated strength for two rocks.....112

Figure 3.33: Angle of internal friction at various temperatures.....114

Figure 3.34: Cohesion at various temperatures.....115

Figure 3.35: Rock specimens with markers for a) axial and b) transverse thermal strain measurements.....117

Figure 3.36: Experimental set-up for thermal strain measurements…….....117

Figure 3.37: Illustration of barycenter.....118

Figure 3.38: Axial strain versus time for mottled anorthosite at different temperatures…….....120

Figure 3.39: Plot of stress/axial/volumetric strain for chromitite at 70°C /10 MPa.....122

Figure 3.40: Plot of volumetric-axial strain for chromitite.....122

Figure 3.41: Plot of dilation angle against temperature for chromitite.....123

Figure 3.42 Effect of temperature on post-peak dilation angle of BIC rocks.....123

Figure 3.43: Experimental set-up for temperature-ultrasonic tests.....126

Figure 3.44: Sample screen shot of P-wave measurement at 140°C for MA.....126

Figure 3.45: Vp and Vs versus temperature for temperature-ultrasonic tests.....127

Figure 3.46: Experimental set-up compression-ultrasonic experiment.....128

Figure 3.47: Vp and Vs versus axial stress for compression-ultrasonic tests.....131

Figure 4.1: Olympus BX 61 optical microscope.....133

Figure 4.2: FEI Nova 600 Nanolab scanning electron microscope.....134

Figure 4.3: (a) OM and (b) SEM samples for image capturing.....135

Figure 4.4: Micrograph of CR (a) before and (b) after heat treatment to 50ºC.....139

Figure 4.5: Micrograph of CR (a) before and (b) after heat treatment to 100ºC.....140

Figure 4.6: Micrograph of CR (a) before and (b) after heat treatment to 140ºC.....141

Figure 4.7: Chromitite (a) before and (b) after heat treatment to 50ºC.....143

Figure 4.8: Chromitite after heat treatment to (a) 100ºC (b) 140ºC.....144

Figure 4.9: Chromitite after heat treatment to 140ºC with repeated heating and cooling.....145

Figure 4.10: Granite subjected to repeated heating and cooling (a) after sputter coating, (b) before sputter coating.....147

Figure 4.11: Granite subjected to repeated heating and cooling (a) after sputter coating, (b) before sputter coating.....148

Figure 4.12: Element map of chromitite (a) before and (b) after heat treatment to 50ºC.....150

Figure 5.1: Graph of virgin rock temperature against depth for platinum mines.....155

Figure 5.2: Model set up for the triaxial simulation.....159

Figure 5.3: Illustration of shear band on a failed triaxial test specimen.....160

Figure 5.4: FLAC plot of norite tested at 20ºC and confining pressure of 10 MPa.....161

Figure 5.5: Laboratory plot of norite tested at 20°C and confining pressure of 10 MPa.....161

Figure 5.6: FLAC plot of norite tested at 50°C and confining pressure of 10 MPa.....162

Figure 5.7: Laboratory plot of norite tested at 50°C and confining pressure of 10 MPa.....162

Figure 5.8: FLAC plot of norite tested at 90°C and confining pressure of 10 MPa.....163

Figure 5.9: Laboratory plot of norite tested at 90°C and confining pressure of 10 MPa.....163

Figure 5.10: FLAC plot of norite tested at 140°C and confining pressure of 10 MPa.....164

Figure 5.11: Laboratory plot of norite tested at 140°C and confining pressure of 10 MPa.....164

Figure 5.12: Plot of laboratory numerical modelling peak strengths.....166

Figure 5.13: Plasticity indicator plot for norite at ambient temperature under no confinement.....167

Figure 5.14: Plasticity indicator of norite sample at different temperature and confining pressure.....168

Figure 5.15: Plasticity indicator of chromitite sample at different temperature and confining pressure.....169

Figure 5.16: Peak strength of norite at various temperatures and confining pressure.....170

Figure 5.17: Peak strength of chromitite at various temperatures and confining pressure.....171

Figure 5.18: Major horizontal to vertical stress ratio as a function of depth (Stacey and Wesseloo, 1998)..... 174

Figure 5.19: Minor horizontal to vertical stress ratio as a function of depth (Stacey and Wesseloo, 1998)..... 174

Figure 5.20: Plot of consistent stress measurement database (Handley, 2013).....176

Figure 5.21: Screen shot of RocLab software used for the determination of rock mass parameters.....177

Figure 5.22: Model boundary.....184

Figure 5.23: Plot of equation 5.12 (Malan (2015), personal communication).....184

Figure 5.24: Illustration of fixed boundaries and the stope.....183

Figure 5.25: Some of the model properties for excavation at a depth of 1073 m.....183

Figure 5.26: Temperature plot for the stope at 1073 m below surface.....185

Figure 5.27: Plot of the pre-mining in-situ stresses at 1073 m below surface.....185

Figure 5.28: State plot at 1073 m below surface.....187

Figure 5.29: State plot at 2835 m below surface.....188

Figure 5.30: State plot at 5038 m below surface.....188

Figure 5.31: Post-excavation temperature at 5038 m below surface.....189

Figure 5.32: Hypothetical squeezing conditions of ultra-deep mining excavations in hard rocks (Malan and Basson, 1998) 190

Figure 5.33: Illustration of horizontal and vertical displacements.....191

Figure 5.34: Plot of vertical and horizontal displacements at 1073 m below surface.....192

Figure 5.35: Plot of vertical and horizontal displacements at 2835 m below surface.....192

Figure 5.36: Plot of vertical and horizontal displacements at 5038 m below surface.....193

Figure 5.37: Illustration of failure measurement intervals 194

Figure 5.38: Sidewall failure indicator at 1073 m below surface.....194

Figure 5.39: Sidewall failure indicator at 2835 m below surface.....195

Figure 5.40: Sidewall failure indicator at 5038 m below surface.....195

Figure 5.41: Hangingwall failure indicator at 1073 m below surface.....196

Figure 5.42: Hangingwall failure indicator at 2835 m below surface.....196

Figure 5.43: Hangingwall failure indicator at 5038 m below surface.....197

Figure 5.44: Comparison of sidewall and hangingwall failure indicators at different depths.....200

Figure 5.45: Plots of induced stresses at all depths.....201

Figure 5.46: State plot for temperature 140ºC at 5038 m below surface.....203

Figure 5.47: State plot for temperature 50ºC at 5038 m below surface.....203

Figure 5.48: State plot for temperature 140ºC at 1073 m below surface.....204

Figure 5.49: Model set up for circular opening.....205

Figure 5.50: Temperature plot for the stope at 1073 m below surface.....206

Figure 5.51: Plot of induced stresses at 1073 m below surface.....206

Figure 5.52: Plot of induced stresses at 2835 m below surface.....207

Figure 5.53: Plot of induced stresses at 5038 m below surface.....207

Figure 5.54: State plot at 1073 m below surface.....208

Figure 5.55: State plot at 2835 m below surface.....209

Figure 5.56: State plot at 5038 m below surface.....209

Figure 5.57: Post-excavation temperature at 5038 m below surface.....210

Figure 5.58: State plot for temperature 140ºC at 5038 m below surface.....211
Figure 5.59: State plot for temperature 50ºC at 5038 m below surface.....212
Figure 5.60: State plot for temperature 140ºC at 1073 m below surface.....212
Figure A1 1: Stress-strain plot for BRPM uniaxial compressive strength tests.....235
Figure A1 2: Stress-strain plot for Khomanani uniaxial compressive strength tests…..235
Figure A2 1: Temperature versus axial strain for anorthosite-chromitite.....236
Figure A2 2: Temperature versus axial strain for chromitite.....236
Figure A2 3: Temperature versus axial strain for vari-textured anorthosite.....237
Figure A2 4: Temperature versus axial strain for pyroxenite.....237
Figure A2 5: Temperature versus axial strain for leuconorite.....238
Figure A2 6: Temperature versus axial strain for mottled anorthosite.....238
Figure A3 1: Pyroxenite tested at 10 MPa confinement, different temperatures.....239
Figure A3 2: Pyroxenite tested at ambient temperature, different confinements.....239
Figure A3 3: Pyroxenite tested at 50°C, different confinements.....240
Figure A3 4: Pyroxenite tested at 90°C, different confinements.....240
Figure A3 5: pyroxenite tested at 140°C, different confinements.....241
Figure A3 6: Pyroxenite tested at ambient and 140°C, zero confinement.....241
Figure A3 7: Mottled anorthosite tested at 10 MPa confinement, different temperatures.....242
Figure A3 8: Mottled anorthosite tested at ambient temperature, different confinements.....243
Figure A3 9: Mottled anorthosite tested at 50°C, different confinements.....243
Figure A3 10: Mottled anorthosite tested at 90°C, different confinements.....244
Figure A3 11: Mottled anorthosite tested at 140°C, different confinements.....244
Figure A3 12: Mottled anorthosite tested at ambient and 140°C, zero confinement.....245
Figure A3 13: Chromitite tested at 10 MPa confinement, different temperatures.....246
Figure A3 14: Chromitite tested at ambient temperature, different confinements.....246
Figure A3 15: Chromitite tested at 50°C, different confinements.....247
Figure A3 16: Chromitite tested at 90°C, different confinements.....247
Figure A3 17: Chromitite tested at 140°C, different confinements.....248
Figure A3 18: Chromitite tested at ambient and 140°C, zero confinement…..248
Figure A3 19: Leuconorite tested at 10 MPa confinement, different temperatures.....249

Figure A3 20: Leuconorite tested at ambient temperature, different confinements.....250

Figure A3 21: Leuconorite tested at 50°C, different confinements 250

Figure A3 22: Leuconorite tested at 90°C, different confinements 251

Figure A3 23: Leuconorite tested at 140°C, different confinements.....252

Figure A3 24: Leuconorite tested at ambient and 140°C, zero confinement.....252

Figure A3 25: Vari-textured anorthosite tested at 10 MPa confinement, different temperatures.....253

Figure A3 25: Vari-textured anorthosite tested at ambient and 140oC, zero confinement.....253

Figure A3 26: Anorthosite-chromitite tested at 10 MPa confinement, different temperatures.....254

Figure A3 27: Anorthosite-chromitite tested at ambient and 140°C, zero confinement.....255

Figure A4 1 (a) Test setting and (b): and image optimization.....257

Figure A4 2 (a)-(d): Optimization/calibration, search for markers and initialization of test.....258

Figure A4 3 (a) and (b): Specimen with four markers.....259

Figure A5 1: The plot of longitudinal strain against time for leuconorite at different temperatures.....260

Figure A5 2: Longitudinal strain against time for chromitite at different temperatures.....261

Figure A5 3: Longitudinal strain against time for mottled anorthosite at different temperatures.....261

Figure A5 4: Longitudinal strain against time for pyroxenite at different temperatures.....262

Figure A5 5: Longitudinal strain against time for granite at different temperatures….....262

Figure A5 6: Longitudinal strain against time for granite at different temperatures….....263

Figure A5 7: Longitudinal strain against time for granofels at different temperatures.....263

Figure A5 8: Longitudinal strain against time for vari-textured anorthosite at different temperatures.....264

Figure A5 9: Longitudinal and transversal strain against time for chromitite at 140°C……..264

Figure A5 10: Longitudinal and transversal strain against time for mottled anorthosite at 140°C.....265

Figure A5 11: Longitudinal and transversal strain against time for leuconorite at 140°C……..265

Figure A5 12: Longitudinal and transversal strain against time for granofel at 140°C.....266

Figure A5 13: Longitudinal and transversal strain against time for gabbronorite at 140°C.....266

Figure A5 14: The plot of longitudinal and transversal strain against time for granite at 140°C.....267

Figure A5 15: Longitudinal and transversal strain against time for vari-texture anorthosite at 140°C.....267

Figure A5 16: Longitudinal and transversal strain against time for norite at 140°C.....268

Figure A5 17: Longitudinal and transversal strain against time for pyroxenite at 140°C…....268

Figure A6 1: Dilation angle against temperature for pyroxenite.....269

Figure A6 2: Dilation angle against temperature for mottled anorthosite.....269

Figure A6 3: Plot of dilation angle against temperature for norite…..270

Figure A6 4: Dilation angle against temperature for vari-textured anorthosite.....270

Figure A6 5: Dilation angle against temperature for leuconorite.....271

Figure A6 6: Plot of dilation angle against temperature for anorthosite-chromitite……271

Figure A7 1: Micrograph of MA (a) before and (b) after heat treatment to 50ºC……..…..…272

Figure A7 2: Micrograph of MA (a) before and (b) after heat treatment to 100ºC…..…….273

Figure A7 3: Micrograph of MA (a) before and (b) after heat treatment to 140ºC……..…274

Figure A7 4: Micrograph of G (a) before and (b) after heat treatment to 50ºC…….……..…275

Figure A7 5: Micrograph of G (a) before and (b) after heat treatment to 100ºC…….……..….276

Figure A7 6: Micrograph of G (a) before and (b) after heat treatment to 100ºC…….277

Figure A7 7: Micrograph of GN (a) before and (b) after heat treatment to 50ºC……278

Figure A7 8: Micrograph of GN (a) before and (b) after heat treatment to 100ºC…….….279

Figure A7 9: Micrograph of GN (a) before and (b) after heat treatment to 140ºC…….….280

Figure A7 10: Micrograph of GF (a) before and (b) after heat treatment to 50ºC……..……281

Figure A7 11: Micrograph of GF (a) before and (b) after heat treatment to 100ºC…….…….....282

Figure A7 12: Micrograph of GF (a) before and (b) after heat treatment to 140ºC……...…283

Figure A7 13: Micrograph of VTA (a) before and (b) after heat treatment to 50ºC…..…….284

Figure A7 14: Micrograph of VTA (a) before and (b) after heat treatment to 100ºC…….….285

Figure A7 15: Micrograph of VTA (a) before and (b) after heat treatment to 140ºC…..…….286

Figure A7 16: Micrograph of PX (a) before and (b) after heat treatment to 50ºC…….....….287

Figure A7 17: Micrograph of PX (a) before and (b) after heat treatment to 100ºC……288

Figure A7 18: Micrograph of PX (a) before and (b) after heat treatment to 140ºC…..…..289

Figure A7 19: Micrograph of N (a) before and (b) after heat treatment to 50ºC……..…..….290

Figure A7 20: Micrograph of N (a) before and (b) after heat treatment to 100ºC……...…..291

Figure A7 21: Micrograph of N (a) before and (b) after heat treatment to 140ºC……...…..292

Figure A7 22: Micrograph of PX (a) before and (b) after heat treatment to 50ºC.....293

Figure A7 23: Micrograph of PX after heat treatment to 100ºC and 140ºC 294

Figure A7 24: Micrograph of VTA (a) before and (b) after heat treatment to 50ºC…..295

Figure A7 25: Micrograph of VTA after heat treatment to 100ºC and 140ºC.....296

Figure A7 26: Micrograph of N (a) before and (b) after heat treatment to 50ºC.....297

Figure A7 27: Micrograph of N after heat treatment to 100ºC and 140ºC.....298

Figure A7 28: Micrograph of MA (a) before and (b) after heat treatment to 50ºC.....299

Figure A7 29: Micrograph of MA after heat treatment to 100ºC and 140ºC.....300

Figure A7 30: Micrograph of LN (a) before and (b) after heat treatment to 50ºC.....301

Figure A7 31: Micrograph of LN after heat treatment to 100ºC and 140ºC….....302

Figure A7 32: Micrograph of G (a) before and (b) after heat treatment to 50ºC.....303

Figure A7 33: Micrograph of G after heat treatment to 100ºC and 140ºC.....304

Figure A7 34: Micrograph of GF (a) before and (b) after heat treatment to 50ºC.....305

Figure A7 35: Micrograph of GF after heat treatment to 100ºC and 140ºC.....306

Figure A7 36: Micrograph of GN (a) before and (b) after heat treatment to 50ºC.....307

Figure A7 37: Micrograph of GN after heat treatment to 100ºC and 140ºC.....308

Figure A7 38: EDS spectra of chromitite for heat treatments at different temperatures.....310

Figure A7 39: EDS spectra of gabbronorite for heat treatments at different temperatures…….311

Figure A7 40: EDS spectra of granofels for heat treatments at different temperatures.....312

Figure A7 41: EDS spectra of granite for heat treatments at different temperatures.....313

Figure A7 42: EDS spectra of leuconorite for heat treatments at different temperatures.....314

Figure A7 43: EDS spectra of mottled anorthosite for heat treatments at different temperatures.....315

Figure A7 44: EDS spectra of norite for heat treatments at different temperatures.....316

Figure A7 45: EDS spectra of pyroxenite for heat treatments at different temperatures.....317

Figure A7 46: EDS spectra of varitextured anorthosite for heat treatments at different temperatures.....318

Figure A7 47: Elemental composition of chromitite for heat treatments at different temperatures.....319

Figure A7 48: Elemental composition of gabbronorite for heat treatments at different temperatures.....320

Figure A7 49: Elemental composition of granofels for heat treatments at different temperatures.....321

Figure A7 50: Elemental composition of granite for heat treatments at different temperatures.....322

Figure A7 51: Elemental composition of leuconorite for heat treatments at different temperatures.....323

Figure A7 52: Elemental composition of mottled anorthosite for heat treatments at different temperatures.....324

Figure A7 53: Elemental composition of norite for heat treatments at different temperatures.....325

Figure A7 54: Elemental composition of pyroxenite for heat treatments at different temperatures.....326

Figure A7 55: Elemental composition of varitextured anorthosite for heat treatments at different temperatures.....327

LIST OF TABLES

Table 2.1: Classification of igneous rocks (Gill, 2010).....8

Table 2.2: Strength and Young's modulus of rocks from Union section (York et al 1998)…....16

Table 2.3: Strength and Young's modulus of rocks from Amandebult section (York et al 1998).....17

Table 2.4: Some of the reviewed literature on the effect of temperature on rock behaviour…….29

Table 2.5: Thermal expansion of some rocks with increasing temperature (Kjørholt, 1992).....46

Table 2.6: Volumetric and linear thermal expansion coefficient of some rocks (Robertson, 1988).....46

Table 2.7: Summary of peak dilation angles for some rock types.....69

Table 2.8: Summary of some of the factors influencing rock strength.....79

Table 3.1: Details of the samples received from different mines.....82

Table 3.2: Borehole depth of rock samples.....83

Table 3.3: Average tensile strength and standard deviation of specimens.....86

Table 3.4: UCS of specimens from Khomanani, Siphumelele, Mogalakwena and BRPM in MPa.....91

Table 3.5: Strength and physical properties of rocks from BRPM.....92

Table 3.6: Values of m, angle of internal friction and cohesion for BRPM specimens.....95

Table 3.7: Young's modulus, Poisson's ratio and strength of norite.....107

Table 3.8: Reduction in strength and Young's modulus of the tested rocks due to temperature increase from 20°C to 140°C.....108

Table 3.9: Percentage difference between laboratory measured and calculated Young's modulus.....111

Table 3.10: Percentage difference between laboratory measured and calculated strength.....113

Table 3.11: The coefficient of linear thermal expansion (αl) –unconfined.....120

Table 3.12: Specimen dimensions and velocities (temperature-ultrasonic tests).....127

Table 3.13: P-and S-waves travel time for compression-ultrasonic tests.....130

Table 4.1: Average modal mineral abundance of UG1 and UG2 seam (Voordouw et al, 2009).....137

Table 4.2: Maximum visible crack lengths of specimens.....145

Table 4.3: Summary of elemental composition (% weight) of CR for all temperatures.....151

Table 5.1: Model input parameters and their sources.....154

Table 5.2: Temperatures and equivalent depths for BRPM.....156

Table 5.3: Average tensile strength and density of specimens.....157

Table 5.4: Summary of friction angle (φ) and cohesion (c).....157

Table 5.5: Post-peak and residual dilation angles for the rocks tested.....157

Table 5.6: Heat capacities, thermal conductivity and coefficient of thermal linear expansion of the rocks.....158

Table 5.7: Principal stresses from platinum mines (Priest, 2012).....173

Table 5.8: Densities (kg/m^3) of rocks from the platinum mines.....175

Table 5.9: Vertical and horizontal stresses used for numerical modelling.....177

Table 5.10: Intact σci , mi and Young's modulus.....179

Table 5.11: Rock mass cohesion, friction angle, Young's modulus and tensile strength as determined from RockLab.....179

Table 5.12: Rock mass shear (G) and bulk (K) modulus and dilation angle (ψ).....180

Table 5.13: Summary of horizontal and vertical displacements.....191

Table 5.14: horizontal and vertical displacements-sensitivity analyses.....204

Table A3 1: Young's Modulus and Poisson's Ratio of pyroxenite 242

Table A3 2: Young's modulus and Poisson's Ratio of mottled anorthosite.....245

Table A3 3: Young's modulus and Poisson's Ratio of chromitite.....249

Table A3 4: Young's modulus and Poisson's Ratio of leuconorite 252

Table A3 5: Young's modulus and Poisson's Ratio of vari-textured anorthosite.....254

Table A3 6: Young's modulus and Poisson's Ratio of anorthosite chromitite.....255

LIST OF SYMBOLS AND ACRONYMS

σ_c	Compressive strength (MPa)
σ_t	Tensile strength (MPa)
σ_1	Major principal stress (MPa)
σ_2	Intermediate principal stress (MPa)
σ_3	Minor principal stress (MPa)
c	Cohesion (MPa)
ψ	Dilation angle (°)
E_{rm}	Rock mass Young's modulus (GPa)
E_i	Intact rock Young's modulus (GPa)
φ	Angle of internal friction (°)
K	Bulk modulus (GPa)
G	Shear modulus (GPa)
EDS	Energy dispersive X-ray spectrometry
FLAC	Fast Langrangian Analysis of Continua
RMR	Rock mass rating
GSI	Geological strength index
N	Norite
LN	Leuconorite
GN	Gabbronorite
MA	Mottled anorthosite
VTA	Varitextured anorthosite
CR	Chromitite
ANCR	Anorthosite-chromitite
G	Granite
GF	Granofels
PYX	Pyroxenite
OM	Optical microscope
SEM	Scanning electron microscope
ISRM	International Society of Rock Mechanics
HPU	Hydraulic Pump Unit

MPT	Multi-purpose testware
UCS	Uniaxial compressive strength
BIC	Bushveld Igneous Complex
BRPM	Bafokeng Rasimone Platinum Mine

CHAPTER ONE

1.0 INTRODUCTION

Many challenges are faced with increasing depth of mining in underground mines. The most obvious are heat, stress and logistical issues. Issues related to underground heat have focused mainly on the side effect of heat on workers' health, increase in production costs as a result of higher cost of ventilation (Biffi *et al*, 2007; Brake and Bates, 2000; Payne and Mitra, 2008). The effect of increase in temperature with increasing depth on the behavior of rock has not been given much consideration.

Generally, gold mines in South Africa are deeper than the platinum mines however the latter has higher temperature gradient, which makes it hotter as compared to similar depths in gold mines. Although, the study of the effect temperature on the behaviour of rock can be beneficial to both gold and platinum mines, the focus of the research is on the rock types encountered in the platinum mines.

1.1 Study Area

The platinum mines are in the Bushveld Igneous Complex (BIC), which is located in the northern part of South Africa. The Bushveld Igneous Complex is the world's largest layered intrusion. It is about seven to nine kilometers thick and is divided into eastern, western and northern limbs. Its upper critical zone hosts the world's largest deposit of platinum group elements (PGE), (Schouwstra and Kinloch, 2000). Figure 1.0 shows the map of the BIC.

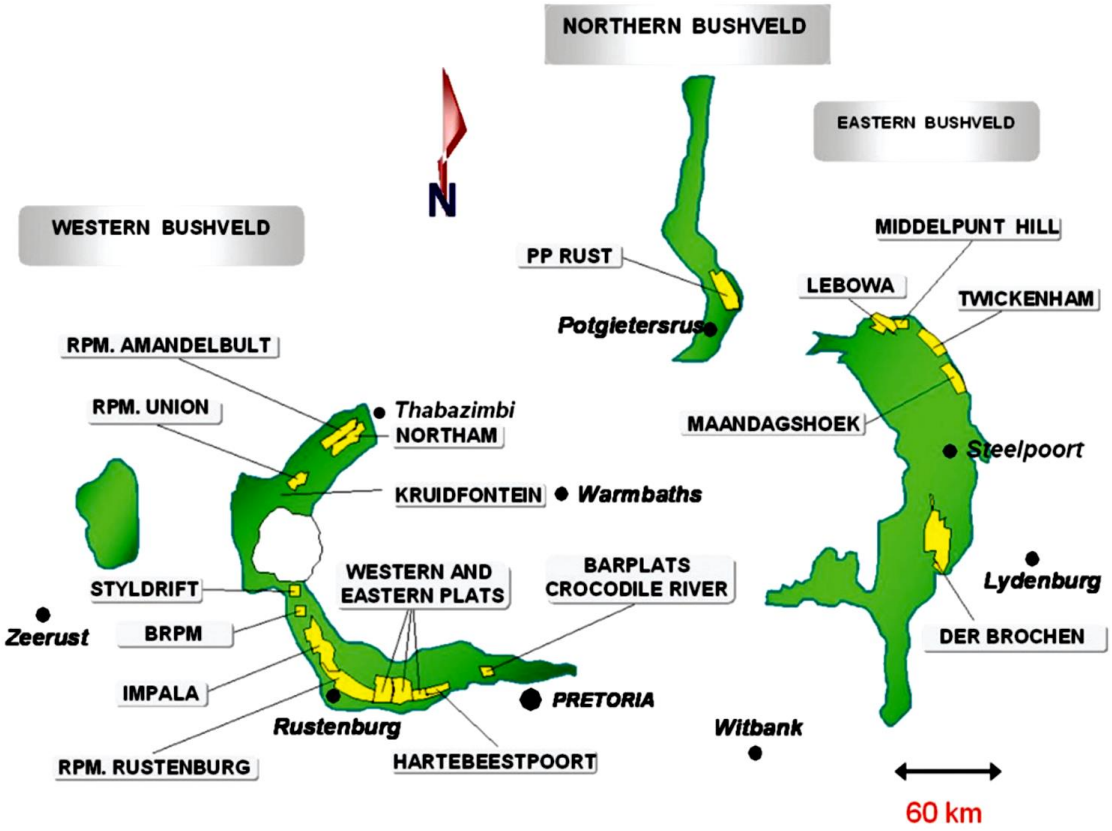


Figure 1.0: Map of the Bushveld Igneous Complex (Watson *et al*, 2010)

1.2 Problem statement

South Africa has the deepest mines in the world. Some of the gold mines are planning for ultra-deep mining, that is, mining below the surface at a depth range of 3500m to 5000m. Amongst the platinum mines, on the other hand, Northam Platinum Mine (located in the northern part of the western limb of the BIC in Limpopo Province) is the deepest platinum mine in South Africa and is already mining at more than 2km below surface. Geological exploration information revealed the possibility of the platinum mines going for ultra-deep mining in future. Schouwstra *et al* (2000) stated that the Merensky Reef has been traced for 300 km around the entire outcrop of the eastern and western limbs of the BIC, and to depths of 5 km and beyond.

Cawthorn (1999) proposed adapting the knowledge from deep mining on the gold-bearing Witwatersrand mines to Merensky and UG2 ores. He however, noted

that high temperature will be additional challenge that will be faced by platinum mines in ultra-deep mining. Since it has been established that high stress and high temperature are serious challenges to deep platinum mines, it becomes necessary to investigate the influence of these parameters on rock behaviour from rock engineering perspective. There are no records of research conducted to establish the effect of temperature on the behaviour of rock in relation to depth of mining neither in South Africa nor in any other part of the world. Testing of rocks from South African mines to establish the effect of temperature variation on the physical, chemical and mechanical properties of rocks has not been done. The only relevant research in South Africa was done by Jones (2003), where the thermal properties of stratified rocks from the Witwatersrand gold mining areas were measured.

This research, however, will study the response of rocks, particularly from BIC, to variation of temperature from rock engineering point of view through laboratory, microscopic and numerical analyses. Rock lithologies at great depth are subjected to high virgin temperatures and stresses before mining. The air temperature reduces down to around 27.30^{o}C for workers' comfort. While exposed rock surface would still have higher temperatures than the mine air. Nevertheless, rock behaviour in its virgin state is largely unknown. The determination of this behaviour would assist in the support measures that need to be taken to ensure more stable and safer mining environment at great depth.

1.3 Objectives of the research

The major objective of this research is to quantify the influence of temperature and rock stresses on rock behaviour. The understanding of such behaviour would help in the remedies that would be taken for safer mining in the future. This objective will be achieved through:

1) Laboratory testing and numerical modelling by using temperature and stress variation as the control parameters on rock behaviour in deep underground mines of BIC.

2) Microscopic investigation on the influence of temperature on crack generation and propagation with a view to understanding what happens to the excavation when cooled by ventilation.
3) Establishment of a mathematical relationship between temperature, rock strength and stiffness, which will serve as a guide for better rock engineering calculations and design.

The research will contribute to better understanding of the behaviour of rock with increasing depth of mining. Rock failures in the form of rockburst, squeezing, spalling and rock fall at the Bushveld Igneous Complex underground mines will continue to be major causes of accidents. One of the fundamental information required for the planning of stope-support systems is the details of strength and deformation properties of rock particularly in high temperature environment.

1.4 Research methodology

The outline of the research methodology is given below:

- A detailed review of literature that link the work of the previous researchers to the proposed research.
- Understanding of the in-situ stress field from the available stress measurements. That is, the virgin stress condition and the changes in the stress field with mining and time.
- Understanding of temperature variation with depth and virgin rock temperatures from the published articles at mines.
- Collection of rock samples from mines.
- Development of test set-up for the measurement of the thermo-mechanical properties of the rock samples.
- Determination of the thermal properties of the rock samples. These thermal properties are used as input parameters for numerical modelling.
- Numerical modelling of response of rocks to variation in temperature and stress that resemble underground working conditions at BIC.

- Examination of rock samples for crack density after being heated from ambient temperature of approximately 20°C to 50°C, 100°C and 140°C with the aid of Scanning Electron Microscope (SEM) and optical microscope.
- Determination of compressive strengths of rock samples at ambient temperature in accordance with ISRM standards using Amsler testing machine in order to compare the strength of the rocks sourced from different mines and tested in ambient condition. The rock strengths will also be used as input parameters during numerical modelling.
- Determination of the strength parameters of rocks from a particular mine at ambient temperature and up to 140°C at an interval of 20°C using MTS servo-controlled testing machine in order to observe the effect of temperature variation on the strength and the post peak stress behaviour. It should be noted that the rocks are sourced from current workings that are shallow depths. Therefore, they were not subjected to high temperature in their natural form.
- The tests with temperature variation were also done at confining stress of 10, 20 and 30 MPa in order to observe the effect of confinement on the rock behaviour and to calculate the internal angle of friction.
- Data analyses and establishment of the relationship between changes in geo-thermal rock condition and rock strength.

1.5 Scope of the research and limitations

In order to be able to have good understanding of the effect of temperature and stress on the mechanical properties and deformation of rock, other influential parameters in deformation such as discontinuities, non-homogeneity, anisotropy are not considered. There is a limit to the type of rocks from the BIC available for testing. Only the ones released by the mines were tested. For instance, Merensky reef was not made available from any of the mines visited. Numerical modelling was done with FLAC 2D and only in inelastic mode. Elastic modelling was not considered. Temperature and confinement were the test variables during

laboratory testing of rocks using MTS servo-controlled testing machine. Creep test and dynamic loading were not done. The MTS testing machine has a maximum testing temperature of 150°C and cannot test samples below ambient temperature. Due to this limitation, the samples were tested between ambient temperature and 140°C. There are also limitations on the test controls such as specimen dimensions. For instance, the ISRM recommended specimen diameter is at least 50 mm (NQ2) however most of the cores received from mines are 36 mm (BQ). Also, there are challenges with having complete stress-strain plots for the selected rocks because of their brittleness. Therefore, a combination of displacement, axial and circumferential strain controls were used with the MTS servo-controlled testing machine to achieve the complete stress-strain plots.

1.6 Content of the thesis

The thesis describes the effect of temperature on the mechanical behaviour of rocks from the BIC. Chapter 1 introduces the subject matter of the research, stating the reasons for embarking on the research and a summary of how it will be conducted. The second chapter presents a literature survey on the previous published researches on the effect of temperature on the behaviour of rocks and detail description of the BIC. All the thermal and mechanical laboratory testing conducted, are discussed in Chapter 3. Chapter 4 describes the microscopic image capturing of the rock samples after being subjected to heat treatment using optical and scanning electron microscope (SEM). Numerical modelling of the rocks to investigate the effect of increasing stress and temperature with mining depth is explained in Chapter 5, while Chapter 6 concludes the research with recommendations.

CHAPTER TWO

2.0 LITERATURE REVIEW

This chapter presents some background information on mechanical and thermal behaviour of rocks within the context of previous researchers and what has been identified as the gap to be filled from the previous works. It reviews the effect of parameters on behaviour of rocks other than temperature. It also gives background information about the study area and establishes link between previous works and the current research. It should be noted that the rocks obtained from the mines are of igneous origin. Prior to delving into the broad topic, there is need for a brief classification of igneous rock and detailed description of the study area. The reason for including this classification and description in the literature review is that the classification is linked to understanding the strength of the rocks in one hand, and the reaction of the rock minerals to temperature as explained in Chapters 3, and 4.

Table 2.1 gives a summary of the characteristics of igneous rocks based on position, chemical and mineralogical composition.

Table 2.1: Classification of igneous rocks (Gill, 2010)

	Classification	Description	Examples
A	**Ocurrence/ Position**		
1	Intrusive	Crystallized in great depth and forming large rock bodies	Granite, Anorthosite, Pyroxenite, Norite
2	Extrusive	Rocks reaching the surface before crystallization	Pumice, Basalt, Rhyolite
B	**Chemical**		
1	Acidic	63-70% SiO_2	Granite, Rhyolite
2	Intermediate	52-63% SiO_2	Andesite, Dacite
3	Basic	45-52% SiO_2	Gabbro, Norite, Gabbronorite
4	Ultrabasic	45% SiO_2	Pyroxenite, Anorthosite
C	**Mineralogical**		
1	Felsic	Light coloured, colour index = 0-50% (in terms of darkness), contains more quartz, plagioclase, muscovite and feldspar minerals	Anorthosite
2	Mafic	Colour index = 50-80% contains ferromagnesian minerals	Norite, Gabbronorite
3	Ultramafic	Colour index > 80% contains more ferromagnesian minerals like Olivine, amphibole, biotite, ortho- and clino-pyroxene.	Harzburgite, Pyroxenite, Chromitite

N.B. – All the rock samples for this research are intrusive, basic to ultrabasic and majorly mafic to ultramafic.

2.1 The Bushveld Igneous Complex (BIC)

Kinnaird (2005) described the BIC as predominantly mafic (rich in mineral Mg and Fe), intrusive and extrusive rock. It was formed as a result of repeated injection of magma into a sub-volcanic, shallow level chamber. Based on lithostratigaphic Classification (Ryder and Jager, 2002), BIC is divided into Lebowa Granite Suite, Rashoop Granophyre Suite and Rustenburg Layered Suite (RLS). The RLS is described as the main body of the Bushveld Igneous Complex. It comprises 7000 m (West) to 9000 m (East) of basic igneous rock types which intrude into formation of Transvaal sequence. Its thickness is 9 km. Aside the fine-grained basal norite, there is upward change from ultra-basic rocks towards the base to basic rocks higher in the RLS succession. The RLS is further divided into upper, main, critical and lower zones. The critical zone is where the most important mining activities take place because of its richness in Platinum Group Elements.

The BIC, which consists of three different ore bodies, the Merensky Reef, the Upper Group 2 (UG2) chromitite and Platreef is known for its large proportion of the world's platinum and palladium resources. Platinum exists in BIC in association with six closely related elements, namely, palladium, rhodium, iridium, ruthenium, and osmium. Platinum and the associated elements in the BIC are referred to as the platinum-group metals (PGM) or platinum-group elements (PGE) (Cawthorn, 1999; Holwell and McDonald, 2007). The map of the BIC is shown in Figure 2.1, while the detailed geological information is presented in Figure 2.2

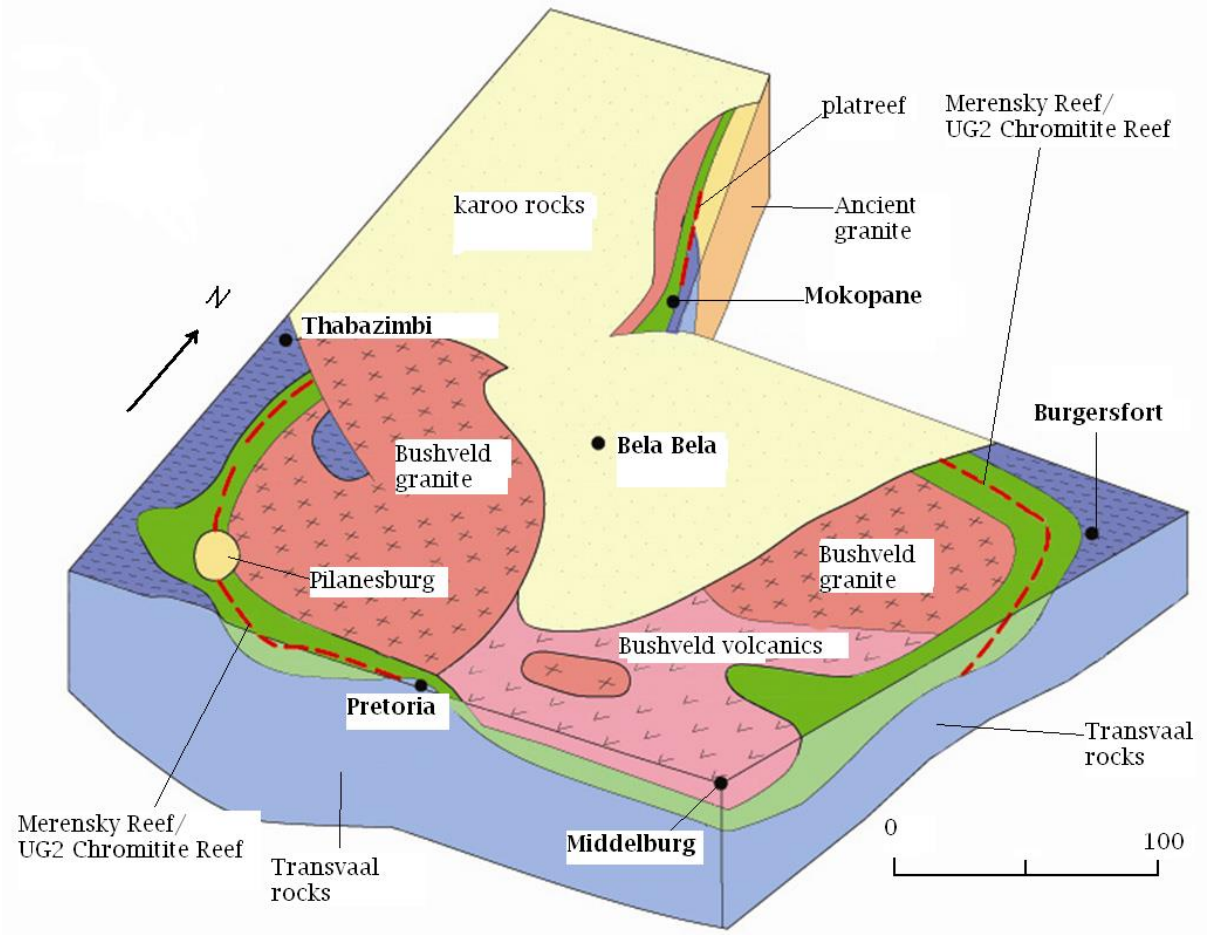


Figure 2.1: Map of the Bushveld Igneous Complex, (Cawthorn, 2010)

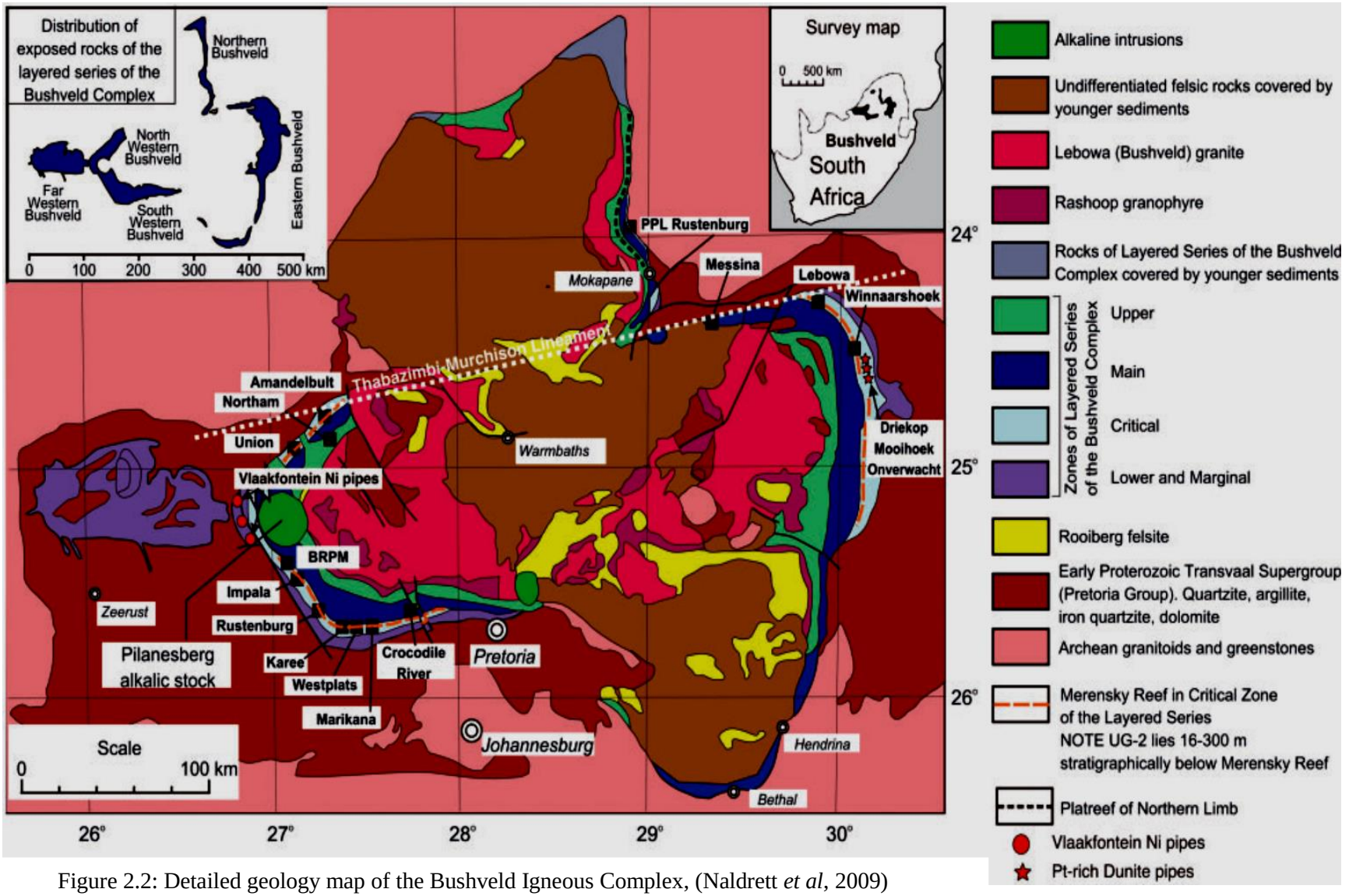


Figure 2.2: Detailed geology map of the Bushveld Igneous Complex, (Naldrett *et al*, 2009)

The layered mafic-ultramafic rocks of the BIC have been divided into western and eastern limbs with smaller northern limb as shown in Figures 2.1 and 2.2 The Platreef, which has the lowest reserve when compared with Merensky and UG2 Reef, consists of complex series of medium-to-coarse grained pyroxenites and norites. From north to south of the Platreef, the footwall is a combination of quartzites, shales, carbonate rocks, granite and gneiss (Pronost *et al*, 2008; Cawthorn 1999).

The lithology of the BIC is important to this research, due to the necessity of the knowledge on the location of the stopes and the types of rocks that form the footwall and hanging wall. The lithology of the western Bushveld, which hosts the Merensky and the UG2 chromitite Reef, is shown in Figure 2.3. The description of the eastern Bushveld (Winnaarshoek) which also hosts a portion of the Merensky and the UG2 chromitite Reef was given by Scoon and Mitchell (2002). There exists a 2-5 m thick layer of feldspathic pyroxenite that is overlain by a sequence of norite-leuconorite, spotted-mottled anorthosite, and mottled anorthosite.

Tassell (2010) reported Northam as the South African deepest platinum mine, mining the Merensky reef through No. 2 shaft at a depth of 2100 m. He also pointed out that most platinum is still mined from underground mines working at depths extending from close to surface to around 1000 m. The list of the rock samples obtained from the mines for this research, their locations and depths are provided in Chapter 3 (Table 3.1) and are indicated in Figure 2.3 with red rectangles. In the Eastern and Western lobes, the mineralization is hosted in the middle of the BIC, in the Merensky Reef and UG2 Chromitite layers. In contrast, the mineralization is hosted at the lower margin of the Complex, the Platreef.

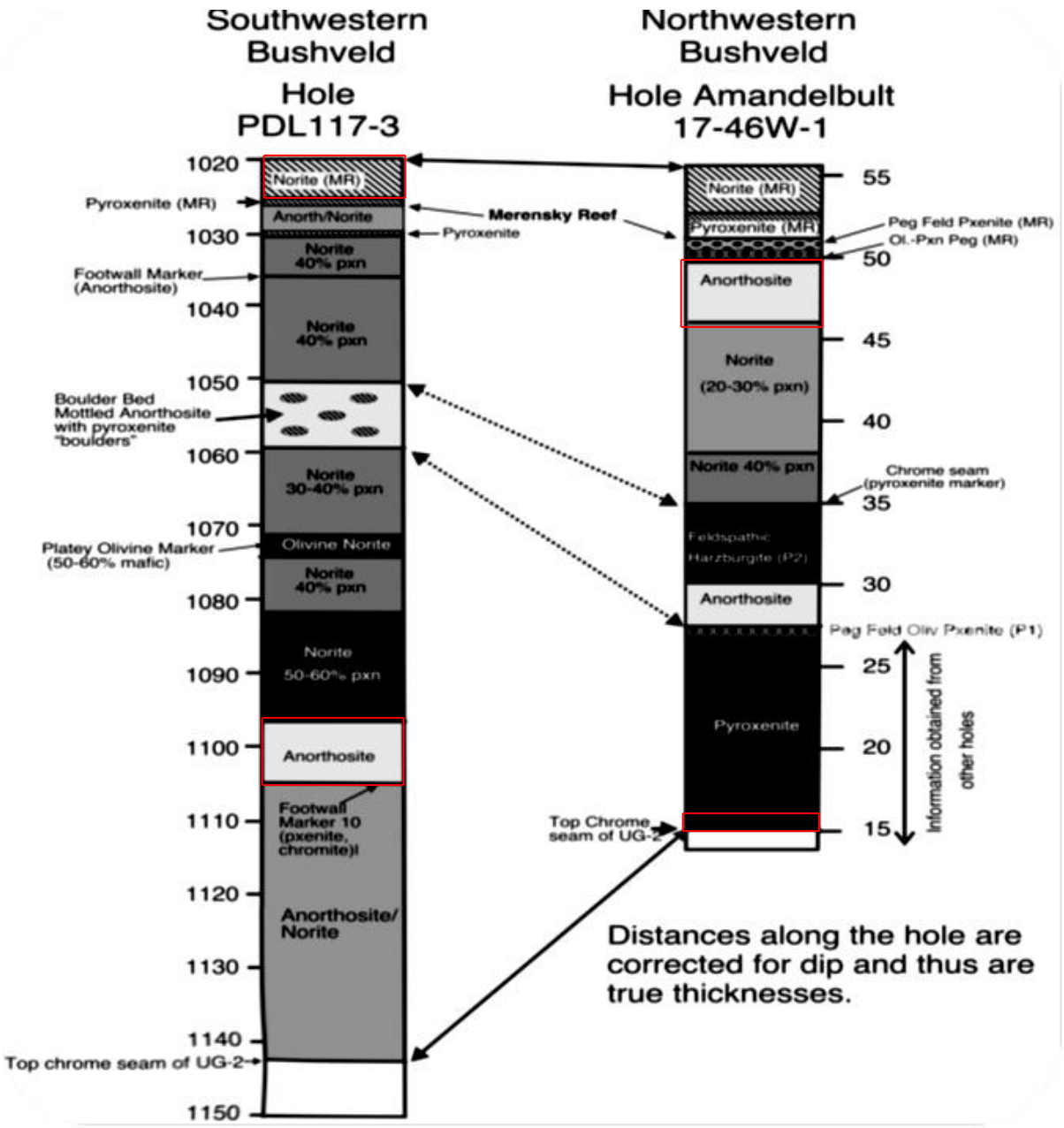


Figure 2.3: A comparison of the stratigraphic succession between the Merensky reef and the top chromite layer of the UG-2 in the Rustenburg (Naldrett *et al*, 2009)

2.1.1 Classification of rock types- rock names and normative composition

The classification of rocks from the BIC, in terms of their mineral or normative composition, is essential since mineral composition has a major influence on their mechanical properties (Wilson *et al* 2005). Generally, rock types are identified

based on mineral proportion and standard criteria set by the International Union of Geological Sciences Sub-commission (IUGS). Figure 2.4 shows the classification of rocks from the Merensky and Bastard Units based on the quantitative analyses of the mineral composition. The red arrows indicate some of the rocks obtained from mines for this research.

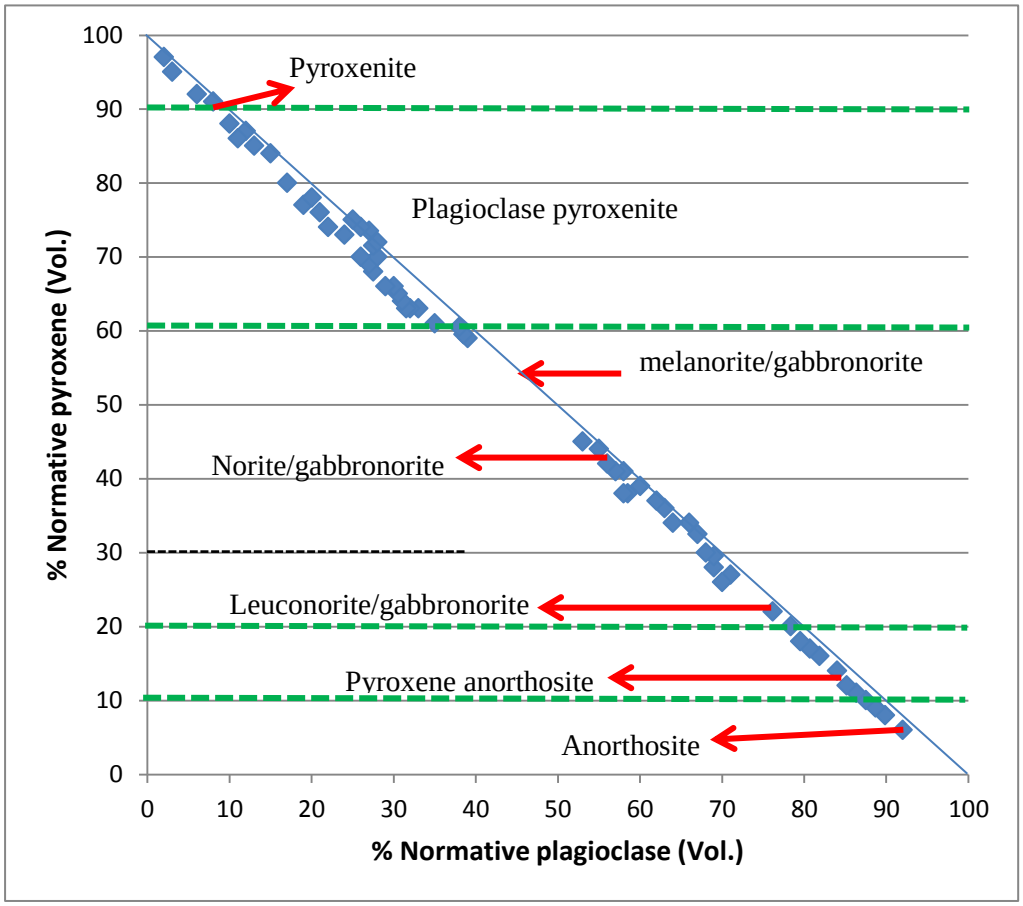


Figure 2.4: Normative mineral compositions for rock samples from the Merensky and Bastard units of the Bushveld Igneous Complex (Wilson *et al*, 2005)

Wilson *et al* (2005) classified anorthosites as Poikilitic/mottled anorthosite and spotted/varitextured anorthosite. "Mottled" anorthosites are characterised by large pyroxene crystals enclosing smaller crystals of plagioclase. Mottled anorthosites contain up to 5 cm diameter optically continuous areas of intercumulus pyroxene

(orthopyroxene and/or augite) within an anorthosite matrix, while "spotted" anorthosites contain up to 1cm diameter orthopyroxene grains with plagioclase chadacrysts in an anorthosite matrix.

Figure 2.5 shows the photograph of hand held specimens from the main zone of the BIC.

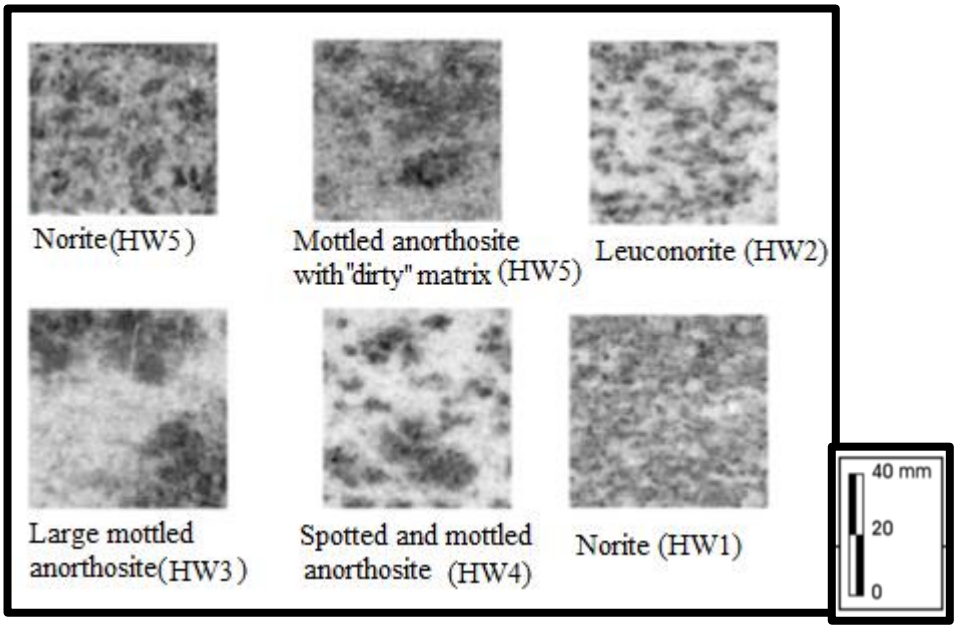


Figure 2.5: Photographs of units HW1 to HW5 of the Bastard reef in hand held specimen (Mitchell and Manthree, 2002)

2.1.2 Mechanical properties of Bushveld rocks

Haile and Jager (1995) stated that there is variability in the rock type properties of the BIC rocks. The reason of this variability remains unclear. They gave analysis of mottled anorthosite sourced from different stratigraphic horizon at approximately 25 and 50 m in the hangingwall of the Merensky horizon. Analysis of the individual strengths from these horizons indicated the Uniaxial Compressive Strength (UCS) to be 175 and 233 MPa respectively. Watson (2010) also observed variability on Poisson's ratio for anorthosite. He reported Poisson's ratio of 0.70 and 0.32 at 50% of the UCS for non-linear and linear samples respectively. Wilson *et al* (2005) proposed some reasons for the variation of

strength of norites around the Merensky Reef. These include textural relations and mineral associations, bulk rock composition, the nature and amount of cementing medium, fabric and stress history of the rock from early compaction to late-stage cooling. Wilson *et al* (2005), however, conclude that there is need for more research to establish the roles of these factors.

Table 2.2 and 2.3 show the strength and Young's modulus of rocks from Union section and Amandebult section Anglo-Platinum Mines respectively. Figure 2.6 also shows the stress-strain plot of footwall anorthosite, Merensky Reeef and hangingwall pyroxenite from Amandebult section tested under triaxial condition, at confining pressures of 10, 20 and 40 MPa.

Table 2.2: Strength and Young's modulus of rocks from Union section (York *et al* 1998)

Rock Type	Average UCS (MPa)	Average Young's Modulus (GPa)
	Hangingwall	
Mottled Anorthosite	196	80
Spotted Anorthosite	180	74
Leuconorite	189	81
Norite	209	96
Melanorite	145	74
Merensky Reef	131	104
	Footwall	
Pyroxenite	167	N/A
Harzburgite	170	N/A
UG2	38	N/A
Upper Pyroxenite	101	N/A
Lower Pyroxenite	187	N/A

Table 2.3: Strength and Young's modulus of rocks from Amandebult section (York *et al* 1998)

Rock Type	Average UCS (MPa)	Average Young's Modulus (GPa)
Hangingwall		
Poikilitic Anorthosite	187	90
Poikilitic Pyroxenite	130	115
Leuconorite	179	85
Norite	195	92
Melanorite	163	104
Bastard Reef	122	112
Footwall		
Merensky Reef	123	74
Harzburgite	106	72
Poikilitic Anorthosite	290	90
Melanorite	153	103
Norite	201	86
Leuconorite	235	82

As observed in Table 2.2, Table 2.3 and Figure 2.6, the reef strength is lower than that of the footwall and the hangingwall. Figure 2.6 shows the increase in strength of the rock as a function of increase in confinement.

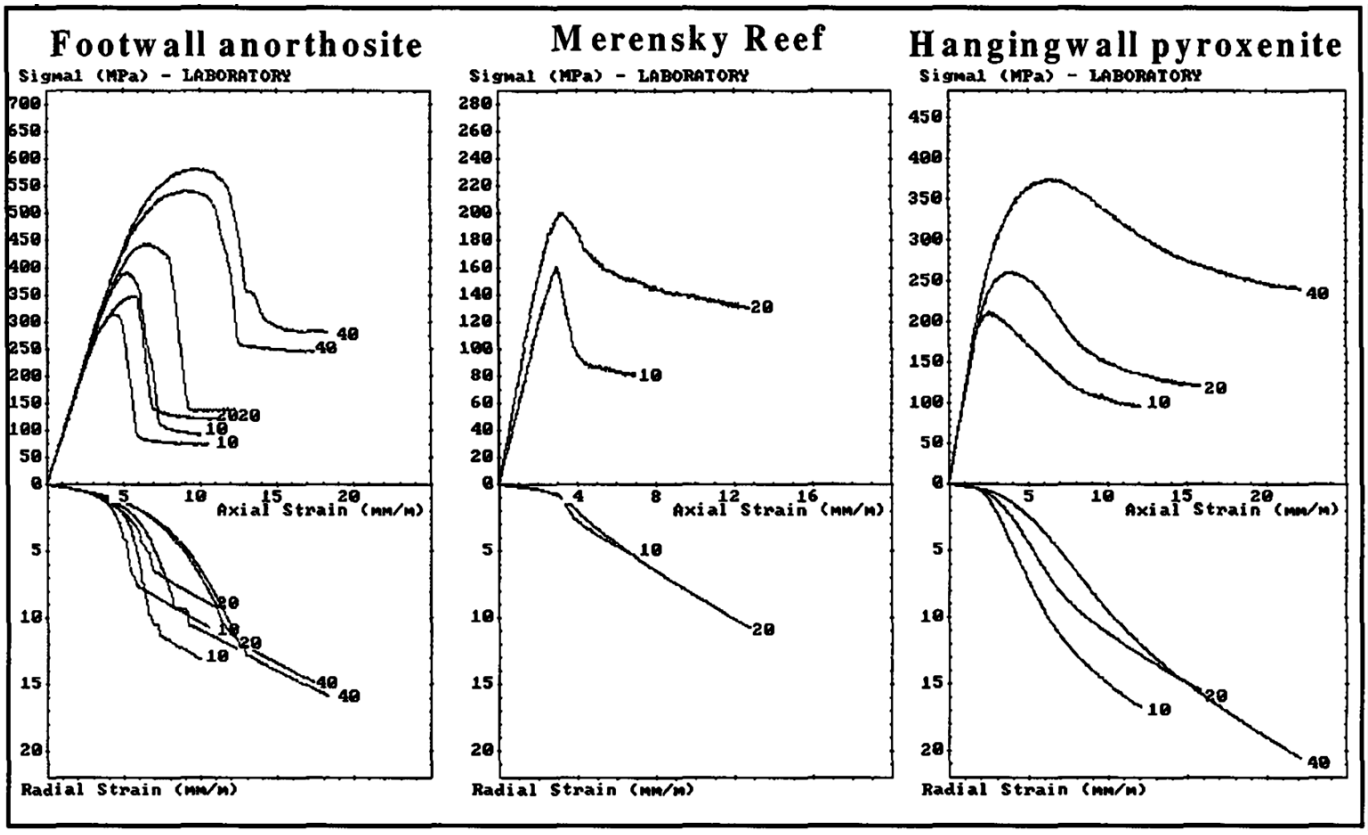


Figure 2.6: stress-strain plot of Merensky reef and immediate footwall and hangingwall tested under triaxial condition (York *et al*, 1998)

Table 2.2 reveals that the hangingwall rocks are relatively stronger than footwall rocks at Union Mine. York *et al* (1998) attributed the weakness of footwall to increase in dilation, which eventually led to observed footwall heave. The reverse is observed for Amandebult Mine, where the footwall rocks exhibit higher strength than those of the hangingwall as shown in Table 2.3. This is also evidence for the variability of strength properties of the Bushveld rocks.

2.2 Factors influencing the behaviour and mechanical properties of rock

The behaviour of rock, under laboratory testing, is influenced by factors such as the mineral composition, texture of the specimen, presence of pores and micro-fractures, moisture content, time, temperature, pressure, rate of loading and

machine characteristics (Stacey *et al*, 1987). Ramamurthy (2010) categorized the factors influencing rock response into five, namely,

1. geological (geology age, weathering and other alterations),
2. lithology (mineral composition, cementing material, texture and fabric and anisotropy),
3. physical (density, porosity),
4. mechanical (specimen preparation, specimen geometry, restrain at loading ends, testing machine, i.e. soft or stiff and loading rate) and
5. environmental (moisture content, nature of pore fluid, ambient temperature and confining pressure.

He further stated that, in the case of rock mass, in addition to the afore-mentioned factors, the structural factors such as bedding planes, shear planes, joints, fractures, faults and the gouge material present would determine the response of the rock mass.

Some of the factors that affect the behaviour of rocks are discussed below. The essence of discussing these factors is to consider how much of effects they have on rock behaviour and to establish that previous research works have covered these areas.

2.2.1 Influence of mineral composition

The physical properties and strength of rock materials are influenced by its mineralogical composition. The proportion and the relationship of the individual mineral that make up the rocks plays an important role in the engineering properties of strength, durability, weathering and hardness (Stacey *et al*, 1987). Increasing the quartz content of quartzite, gneisses, amphibole and dolomite resulted in higher UCS, while increasing muscovite, biotite and dolomite contents led to strength reduction (Figure 2.7).

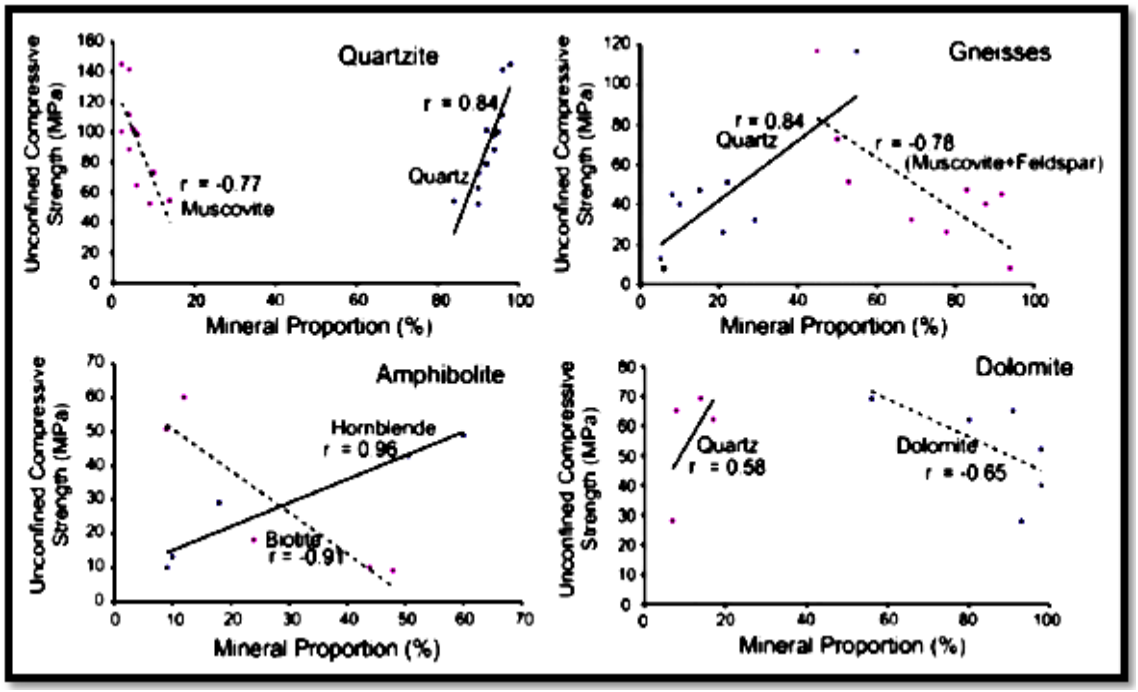


Figure 2.7: Relationship between UCS and mineralogical content of some rocks (Tandon and Gupta, 2013)

2.2.2 Influence of texture and structure

The manner in which crystals interlock is an important parameter controlling the physical and mechanical behaviour of igneous rocks. According to Bell (2000), fracture takes place more along crystal boundaries than within crystals. This implies that a rock strongly interlocking crystal boundaries will resist failure more than the one with weak boundaries.

Rock texture, as defined by Azzoni *et al* (1996) is the description of the form, dimensions and depositions of the mineral grains constituting the rocks. Howarth and Rowlands (1986) developed a technique known as "Texture Coefficient" (TC) for expressing rock texture. TC evaluates the grain shape, relative proportion of grains, orientation and degree of interlocking of grains through microscopic image analysis. Tandon and Gupta (2013) reported a direct relationship between UCS and TC for quartzite as shown in Figure 2.8.

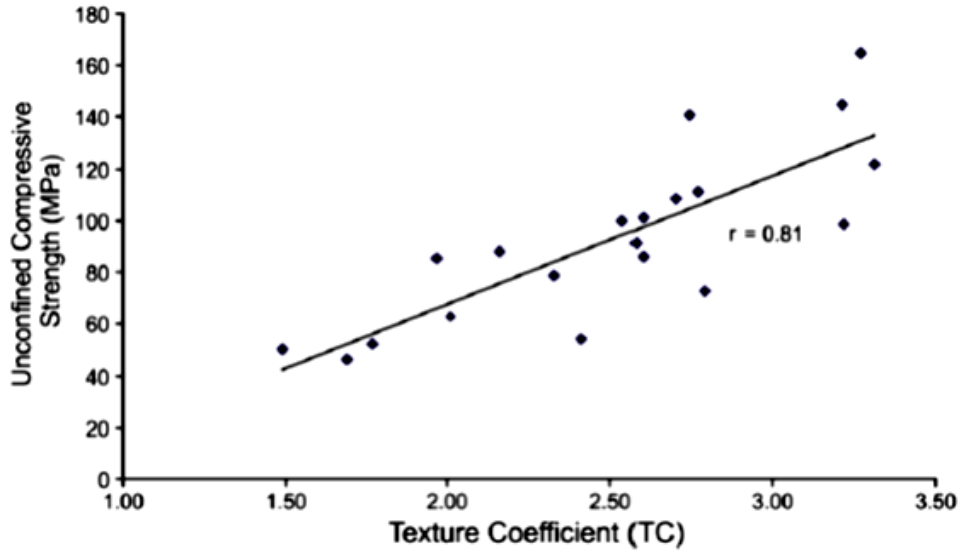


Figure 2.8: Relationship between uniaxial compressive strength and texture coefficient for quartzite (Tandon and Gupta, 2013)

2.2.3 Influence of porosity

The strength of rocks decreases with increasing porosity. Palchik (2006) investigated the influence of porosity on uniaxial compressive strength of Sandy Shale Samples. As can be seen in Figure 2.9, the Uniaxial Compressive Strength (UCS) decreased with increase in porosity of the rock, similar to the studies that have been carried out on granites, dolomites, limestone, sandstone by Vernik *et al* (1993), Palchik (1999), Lumb (1983) and Al-Harthi *et al* (1999). In Figure 2.9, the percentage strength reduction (~ 85 %) is calculated from the difference of UCS at 50% and 20% porosity. The influence of porosity on the Bushveld rocks will not be pronounced based on the fact they have very low porosity.

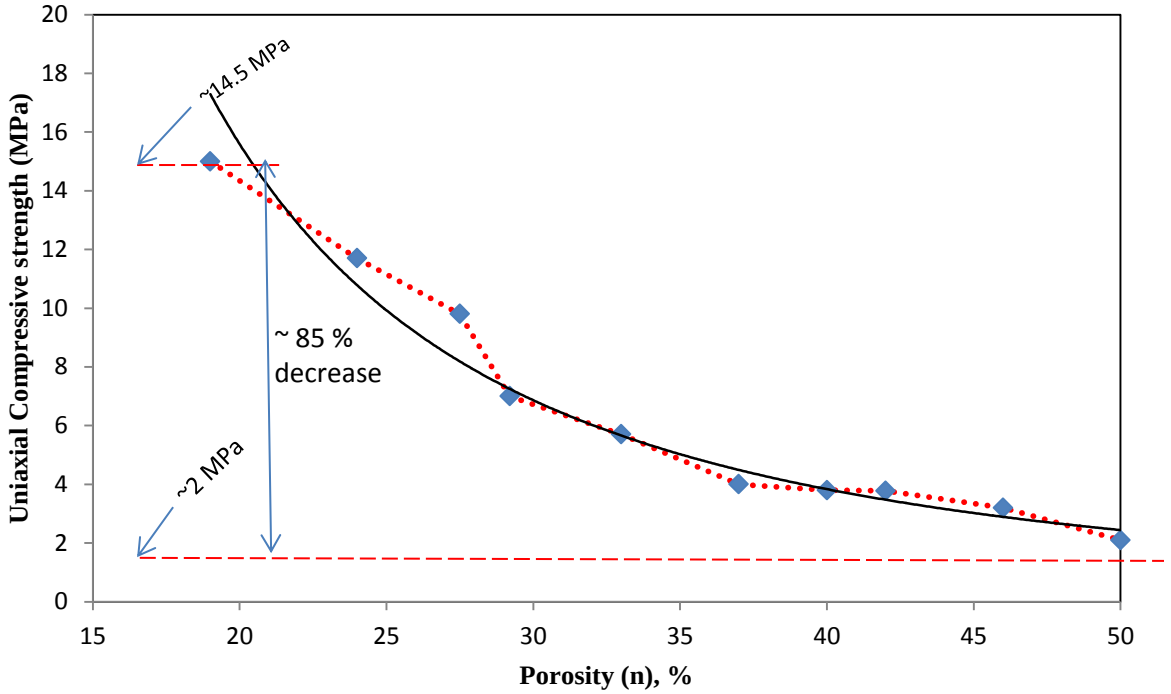


Figure 2.9: Influence of porosity on uniaxial compressive strength (Palchik, 2006)

Vutukuri (1974) examined the effect of liquids on the tensile strength of limestone. He demonstrated a decrease in tensile strength with increasing moisture content. Also in the investigations carried out by Ojo and Brook (1990), they concluded that moisture significantly reduces the strength of rocks. Vásárhelyi and Ván, (2003) showed that there is a linear correlation between the UCS of dry and fully saturated sandstone (Figure 2.10). The UCS of saturated sandstone is approximately 25% lower than the UCS of dry sandstone.

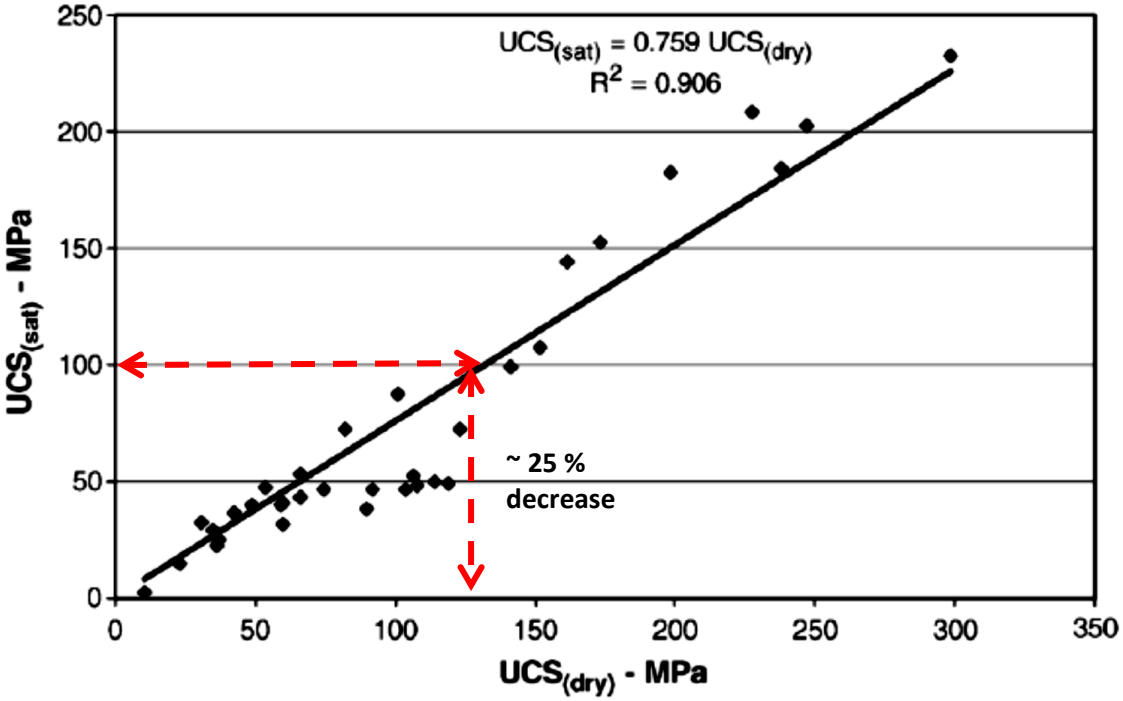


Figure 2.10: Comparison of UCS of dry and saturated 35 British sandstones (Vásárhelyi, 2003)

2.2.4 Effect of time under constant load

The strength and deformation characteristics of rocks are time dependent. A rock specimen, which is subjected to constant stress, deforms over a period of time (Creep). Shao *et al* (2006) explained that the development of creep deformation is an important factor for long-term safety in many structures; he further stated that in brittle rocks, creep deformation is essentially related to sub-critical propagation of micro-cracks due to stress corrosion process.

A schematic creep deformation curve of rock is given in Figure 2.11.

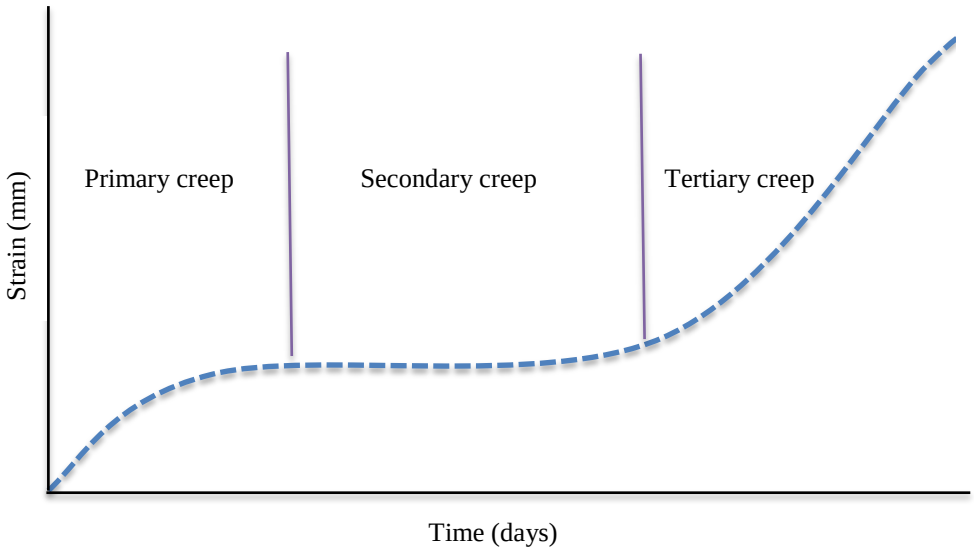


Figure 2.11: Schematic diagram of creep deformation (adapted from Okamoto *et al*, 2004)

The major methods used to study time-dependent behaviour of rock material are laboratory creep test and in situ rheological observations. Creep test can be carried out on servo-controlled testing machine, it, however, requires comparatively higher cost, in terms of energy consumption and time. As shown in Figure 2.11, the creep of rocks passes through three stages of primary (deceleration), secondary (steady) and tertiary (acceleration), which depends on applied load and nature of rock material (Li and Xia, 2000; Okamoto *et al*, 2004).

2.2.5 Effect of loading rate

Many researchers have investigated the influence of loading rate on the deformability and compressive strength of intact rocks. The outcome of their investigations revealed that rock uniaxial compressive strengths increase with increasing loading rate (Xia 2000, Fukui *et al* 2004). The rate-dependent effect becomes of concern where the strength and elastic properties obtained from laboratory testing are used for design and stability analyses. The laboratory determined strength magnitudes are higher as a result of relatively higher loading

rate recommended by ISRM (1979) as compared to that of loading rates experienced by rocks in underground openings. Fuenkajorn and Kenkhunthod (2010) carried out uniaxial and triaxial compressive strength tests on Thai sandstones at loading rates of 0.001, 0.01, 0.1, and 1.0 MPa/s. They reported that the strength and elastic properties of the sandstone increased with the loading rate. Peng and Podnieks (1972) also observed increased strength with increasing loading rate as shown in Figure 2.12. The figure shows 37% strength increase and 43% strain increase when loading rate was increased by five orders of magnitude, that is, from 10^{-7}/sec to 10^{-2}/sec. As pointed out by Li and Xia (2000), the mechanism governing the loading rate dependency for brittle rocks is linked to the time-dependent initiation and propagation of the fractures and micro-cracks in the rock matrix.

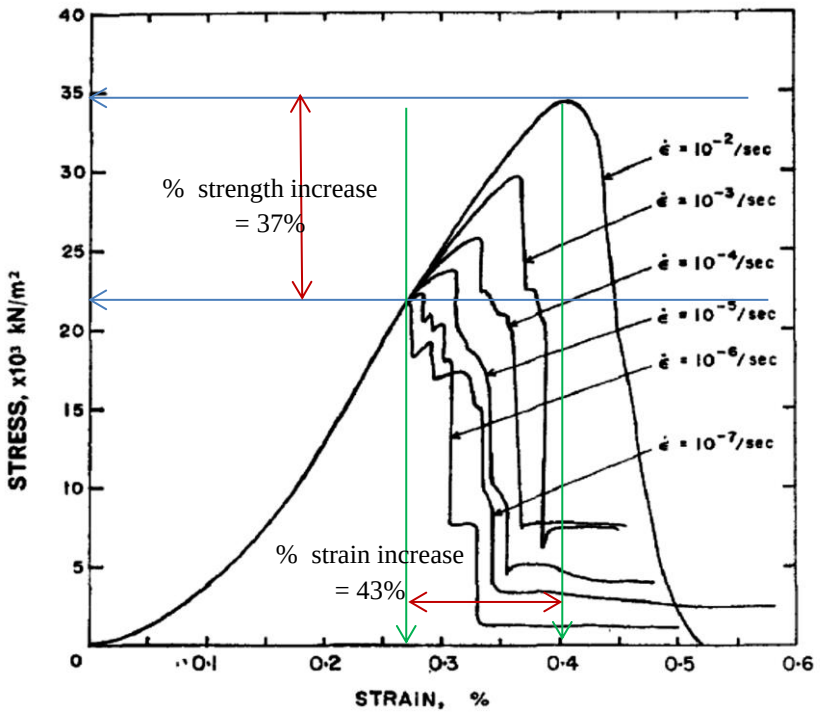


Figure 2.12: Effect of loading rate on the strength of tuff (Peng and Podnieks, 1972)

2.2.6 Effect of discontinuities on rock strength

The presence of discontinuities (joints, fractures, dykes, faults, bedding planes) in rock-mass leads to strength reduction. Ryder and Jager (2002) explained that occurrence of seismic events and rock bursting are highly influenced by geological structures. In order to study the effect of discontinuities on the compressive strength of rocks, Tsoutrelis and Exadaktylos (1993), tested five blocks of Pendali marble with artificially created discontinuities. The extent of the introduced discontinuities is quantified in terms of crack density. They observed decrease in the compressive strengths and modulus of elasticity with increase in discontinuities as shown in Figure 2.13, where σ_{cd} and σ_{ci} are the UCS for blocks with discontinuities introduced and that of the intact rock respectively, while E_d and E_i are modulus of elasticity for blocks with discontinuities introduced and that of the intact rock respectively.

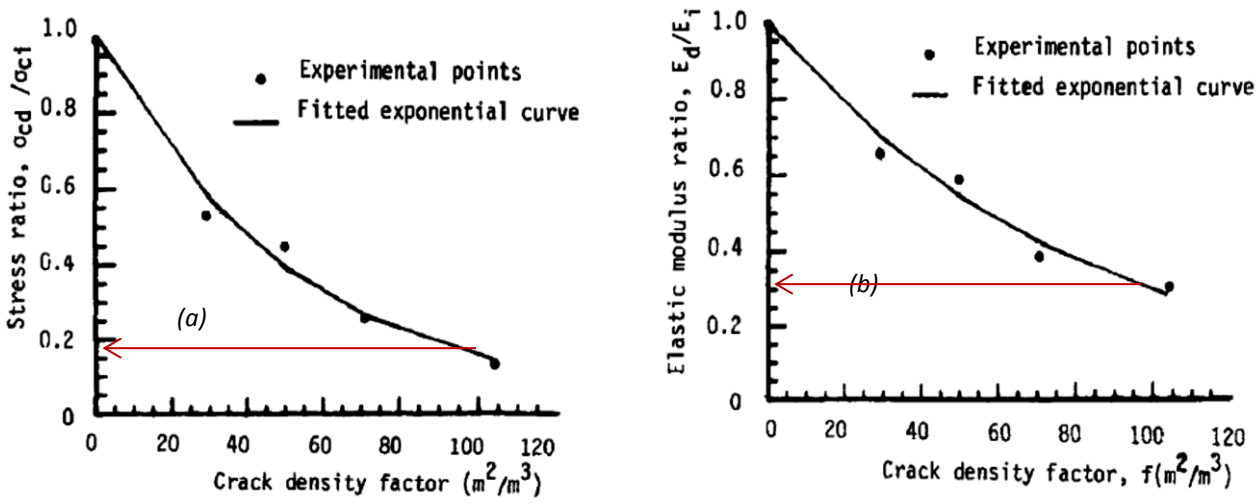


Figure 2.13: Effect of discontinuities on (a) UCS and (b) modulus of elasticity of Pendali marble blocks (Tsoutrelis and Exadaktylos, 1993)

From Figure 2.13, it can be seen that when there was no crack introduced, the ratio of both the UCS and elastic modulus is unity, however, the ratio drops when crack density increased to 100 m^2/m^3, from 100% to approximately 17% and 30% for UCS and elastic modulus respectively.

2.2.7 Effect of temperature on rock behaviour

The available published research on the effect of temperature on the behaviour of rock cover mostly fire accidents at the mines (Smith and Pells, 2008; Smith and Pells, 2009), underground storage repository (Bian *et al*, 2012), volcanic/tectonic activities, (Madonia *et al*., 2013), surface weathering as a result of temperature differential (Gomez-Heras *et al*, 2006). The reviews of the earlier laboratory works on the effect of temperature on the behaviour of rocks are presented below.

Brotón *et al*. (2013) studied the influence of temperature on the physical and mechanical properties of San Julian's calcarenite from 105°C to 600°C. The results show reduction of the elastic modulus, Poisson's ratio and compressive strength for the tested range of temperature. Similar result was obtained by Masri *et al*, (2014), who tested Tournemire shale at different temperatures as shown in Figure 2.14 .

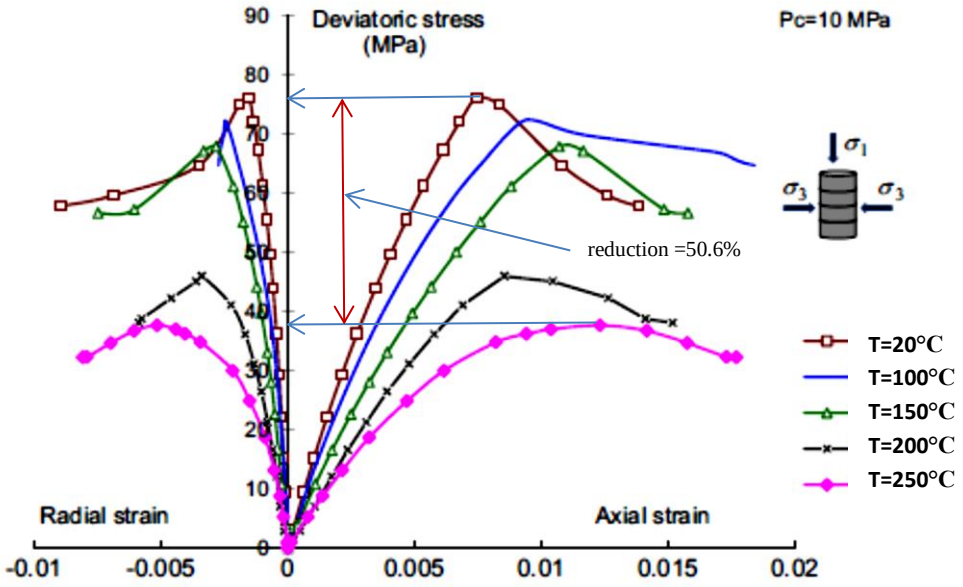


Figure 2.14: Stress-strain curves during triaxial compression tests of Tournemire shale at 10 MPa confining pressure and with different temperatures (Masri *et al*, 2014)

Luque *et al* (2011) observed that environmental temperature fluctuations (between 20°C and 90°C) caused develpoment of new micro-cracks or extension/widening of pre-existing micro-cracks in mable. Table 2.4 summarizes some of the reviewed literature on the effect of temperature on rock behaviour.

Table 2.4: Some of the reviewed literature on the effect of temperature on rock behaviour

S/N	ROCKS TESTED	PURPOSE OF TEST	FINDINGS	TEMP. RANGE	AUTHORS
1	Marble	Effect of heat on marble columns exposed to fire accident	Decrease in UCS, secant deformation, poisson's ratio, angle of friction and cohesion of the samples with increase in tempearture	20°C to 300°C	Koca *et al*, 2006
2	Inada granite & Shirahama sandstone	Influence of temperature on the mechanical properties of granite and sandstone.	Indirect tensile strength, strength intensity factor and stress corrosion factor decreased with increase in temperature	0°C to 80°C	Kodama *et al*, 2003
3	Diabase, granite and quartzitic schist	Effect of high temperatures on rock mass in the event of a fire in a rock tunnel	Increase in the UCS at 400°C and a very rapid decay in strength from 750°C to 1100°C.Variation in mineral composition of the samples at different temperature	400°C to 1100°C	Saiang and Miskovsky, 2011
4	Senones and Remiremont granite	Characterisation and analysis of thermally-induced micro-cracking	Crack density increases with the intensity of thermal treatment. Reduction in the Young's moduli in compression and tension.	20°C to 600°C	Homand-E and Houpert, 1989
5	Indian granite	Thermo-mechanical characterisation of granites for modelling of geological phenomena	Increase in strength with increase in confining pressure. Decrease in the tensile strength of the granites with increase in temperature	30°C to 1050°C	Dwivedi *et al*, 2008
6	Friable sandstone	Influence of temperature on the mechanical properties of reservoir rocks.	Bulk compressibility decreases with increase in temperature from 80 ^{o}C to 150 ^{o}C. Reduction in the failure limit from 24 ^{o}C to 80 ^{o}C	24°C to 150°C	Araujo *et al*, 1997
7	Crystalline & sedimentary rocks	Influence of temperature on thermal conductivity, thermal capacity and thermal diffusivity	Thermal conductivity and diffusivity decreases with rise in temperature while specific heat capacity and thermal capacity increases with rise in temperature.	0°C to 500°C	Vosteen and Schellschmidt, 2003

Table 2.4. (continued)

8	Granite, diabase, marble, dunite, limestone & quartzite	Investigating thermal expansion of rocks at high pressure.	At low confining pressure, small temperature changes results in appreciable thermal cracking, while most of the cracks are closed at high confining pressure.	2°**C** to 38°**C** plus confinement up to 600 MPa	Wong and Brace, 1979
9	Granite, gabbro, and diabase	Effect of thermal expansion of rock on lunar and terrestrial igneous rocks	Thermal expansion is a function of crack porosity, mineralogical composition, heating rate and preferred crystal orientation.	25°C to 550°C	Richter and Simmons, 1974
10	Granite	Review of high-temperature properties of granitic rocks for understanding geo-thermal activities, magma intrusions and plate tectonics.	Thermal diffusivity, thermal conductivity, Brazilian tensile strength, poisson's ratio, normalized modulus, dimensionless friction angle and cohesion decrease with rise in temperature, while specific heat and linear expansion increase with rise in temperature.	Above 250°C	Heuze, 1983
11	Granitic gneiss	Numerical study of near-field thermo-mechanical response of a nuclear waste vault	Variation of rock properties with temperature has minor effect on heat flow. Rapid rise in the coefficient of expansion with rise in temperature may lead to thermal spalling	Backfill max. temp. = 100°C, waste container max. temp. = 100°C,	Wai and Tsui, 1983
12	Quartz-micaschist	Presentation of some simulation data on thermal gradients and rock weathering at low temperature	Differential temperature in areas where rocks are covered by permafrost makes the interior of the rock warm while the exterior part cools. This results in a zone of compressive stress which may cause shearing.	-19°C to 10°C	Hall and Hall, 1991

The temperature range considered in most of the available literature is either very low (-19°C, Hall and Hall, (1991)) or very high (1100°C, Saiang and Miskovsky, (2011)) in most laboratory and numerical analyses that have been done in this regard, (Table 2.4).

Some of the previous researchers tested heated rock samples that were cooled (Saiang and Miskovsky, 2011; Dwivedi *et al*, 2008) while a few others tested rocks in the heated state (Wei *et al*, 2103, Masri *et al*, 2014; Araujo *et al*, 1997). The selected rocks for this research were loaded in the heated state at the appropriate temperature and confinement, which represents the rocks in their in-situ state.

Most of the previous studies reported reduction in strength of rock with increasing temperature except in few cases such as Rao *et al*. (2007), who tested sandstone between 20°C and 300°C. They reported increase in the strength and mechanical properties of rocks from 20°C to 250°C and reduction above 250°C. The reason they stated for the initial increase is that the samples tested had high moisture content and the applied heat reduced the moisture content, thereby making the rocks to be stronger. Smith and Pells, (2008) also showed strength reduction with increasing humidity and temperature (Figure 2.15).

Nara *et al*. (2010) investigated the effects of relative humidity and temperature on subcritical crack growth in igneous rock. The rocks were tested at relative humidity and temperature of 25% - 90% and 20°C - 80°C respectively. Their study revealed that crack velocity increased with increase in humidity and temperature.

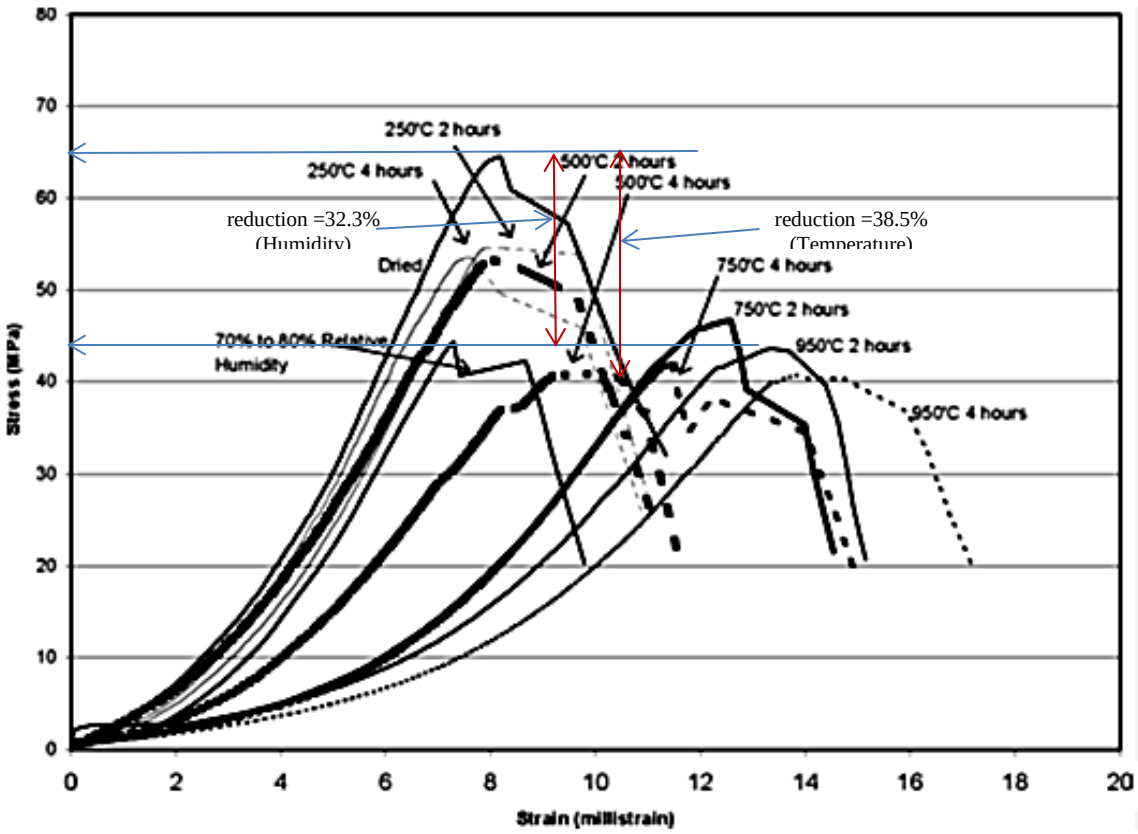


Figure 2.15: Effect of temperature and relative humidity on strength of Hawkesbury sandstone (Smith and Pells, 2008)

The rocks tested in this research were oven-dried to avoid the influence of moisture content in strength reduction.

2.2.7.1 Influence of temperature and confining pressure on Poisson's ratio

Temperature and confining pressure does not have significant influence on Poisson's ratio. Cristensen (1996) carried out laboratory tests on different igneous rocks to study the influence of temperature and confining pressure on their Poisson's ratio.

The outcome of his research is summarized in Figures 2.16 and 2.17. Figure 2.16 shows that there is only slight increase in the Poisson's ratio when confining pressure was increased from 200 MPa to 1000 MPa. The observation in Figure 2.17 is that, for most of the rocks, there is a slight reduction in the Poisson's ratio between ambient temperature and 200°C. After, 200°C, Poisson's ratio fluctuates insignificantly with increasing temperature.

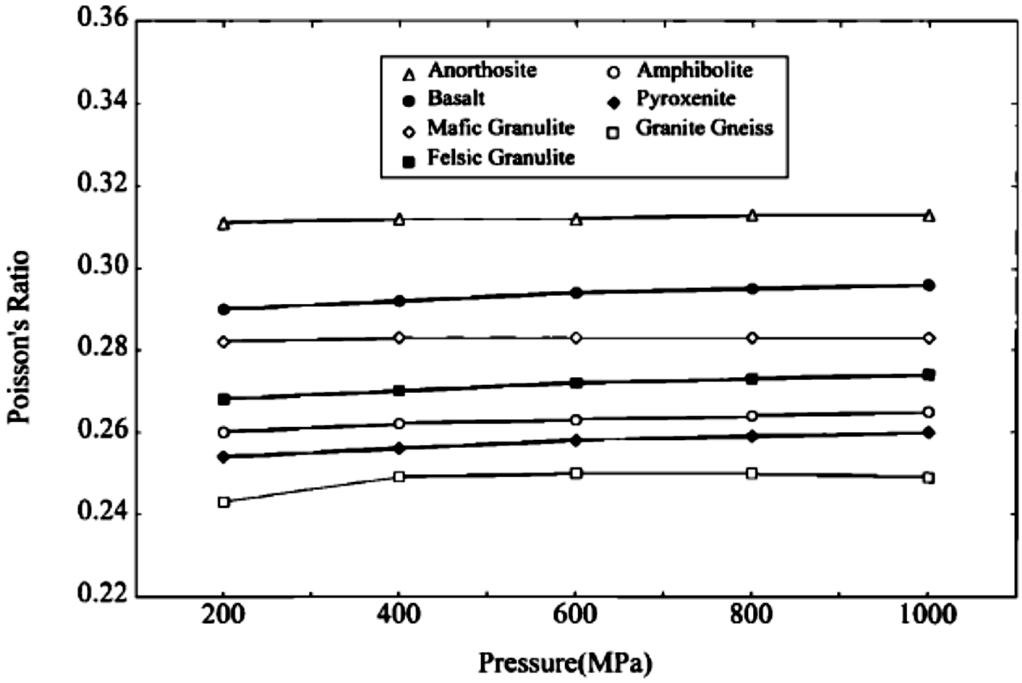


Figure 2.16: Influence of confining pressure on Piosson's ratio (Cristensen, 1996)

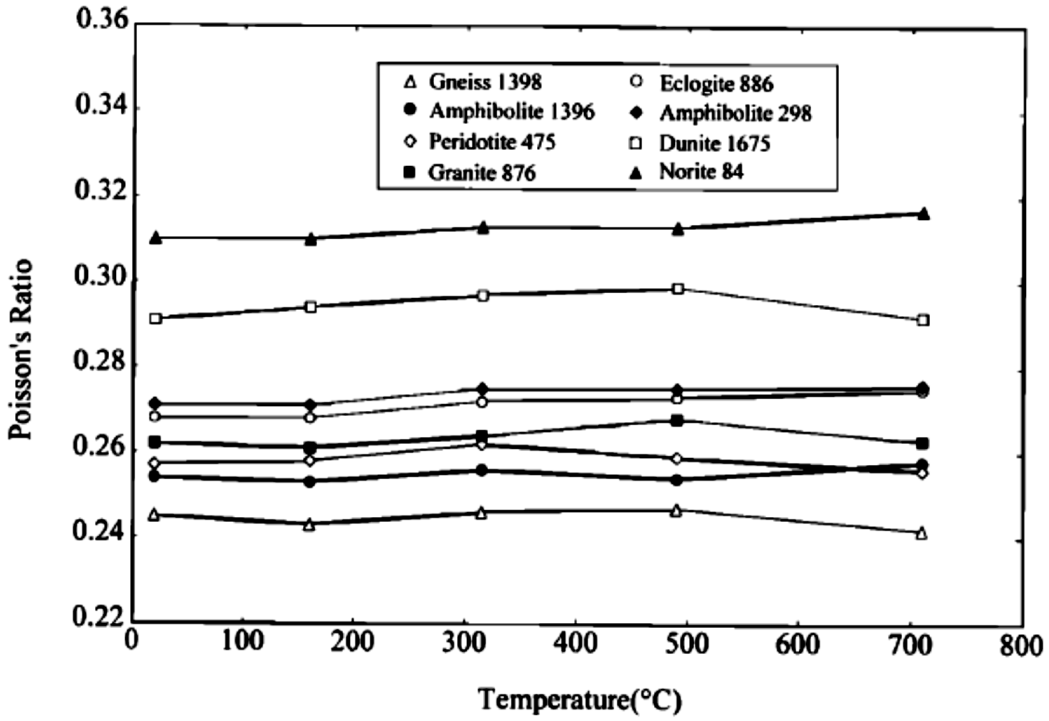


Figure 2.17: Influence of temperature on Piosson's ratio (Cristensen, 1996)

2.2.7.2 Numerical modelling of temperature influence of rock behaviour

There are some numerical modelling analyses on the influence of temperature on the behaviour of rocks carried out by previous researchers. Kim and Yang (2001) studied the behaviour of rock surrounding an underground storage cavern using thermal properties of rock. The distribution of heat and the thermal stress in the cavern were modelled using FLAC. They reported that only the dead weight of the overburden contribute towards the major stress before the storage of low temperature material (refrigerated foods). However, after the storage, the maximum principal stress at the sidewall of the cavern increased more than 60% as a result of thermal stress. This is similar to what this research is looking into. A situation where the virgin rock stress and temperature are high and later on the excavation walls are cooled by ventilation.

Hakami and Olofsson (1999) investigated the thermo-mechanical effects on the near field of a repository using FLAC3D. They started by analyzing the temperature development around the waste, due to the heat released from the waste. Thereafter, the stress change and strains caused by the excavation and the thermal load were analyzed. Their investigations show that yielding of some parts of the wall of the repository tunnel was caused by increasing temperature.

The results from the laboratory tests on rocks under different temperature and confining pressure serve as input parameters into the numerical modelling in the current research. The numerical modelling aspect of the research is also structured to imitate true underground mining environment. There are a number of numerical modelling analyses of stability of underground mining that have been published. However, temperature-coupling in the modelling has not been reported.

The major areas where research have focused on, in relation to depth in the platinum mines, are the influence of increase in rock stresses, development of new mining methods with improved mechanization, pillar design, ventilation, and influence of temperature on the mine workers, in case of inadequate ventilation. For example, Biffi *et al* (2005) outlined some of the ventilation challenges associated with deeper platinum mining and gave an overview of the strategies that could be employed in tackling them. The question of whether the increase in temperature, with respect to depth, will have significant impact on the stability of the working environment remained unanswered.

2.2.8 Effect of confinement

Increasing the confinement of rock under testing generally lead to reduction of pore spaces, particularly for highly porous rock, increase in strength, stiffness, angle of internal friction and cohesion. Liu and Jin (2014) studied the confining pressure and pore pressure coupling effect on rock strength. They reported that rock strength

increases with increasing confining pressure and decreases with increasing hydraulic pressure (Figure 2.18)

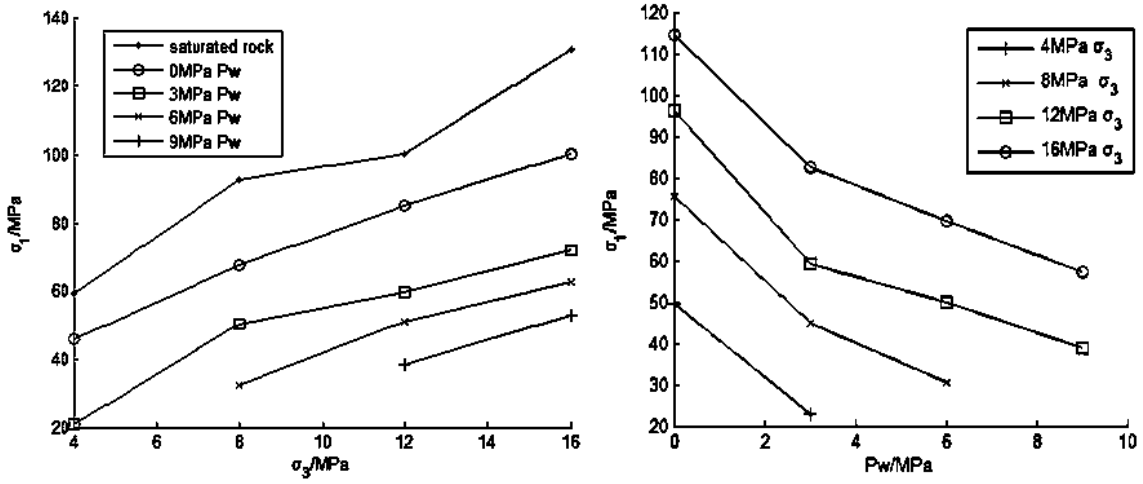


Figure 2.18: Influence of confining (σ_3) and hydraulic pressure (Pw) on strength of fine sandstone (Liu and Jin, 2014)

2.2.8 Thermal fatigue versus thermal shock

Rock deformation as a result of temperature differential is explained by the principle of thermal stress fatigue or thermal shock (Hall, 1999). Thermal stress fatigue can be defined as subjection of material to a series of thermally- induced stress events, each less than that required to cause immediate failure, however cause the material to fail with time. In the case of thermal shock, the thermally induced stress event is of sufficient magnitude to make the material fail as a result of not being able to adjust fast enough to accommodate the deformation. Based on the temperature range that is applicable in the platinum mines, that is a maximum of approximately 140°C at a depth of 5 km, thermal stress fatigue would be the main cause of concern and not

thermal shock. This research would attempt to model the effect of thermal stress fatigue on rock behaviour.

2.2.9 Relationship between virgin rock temperature and depth

Donoghue (2004) stated that the virgin rock temperatures (VRT) and air temperatures increase with depth, due to the geothermal gradient and auto-compression of air column. A comparison of the geothermal gradient of the Witwatersrand Basin and BIC, as presented by Biffi *et al* (2007) is given in Figure 2.19. Biffi *et al* (2007) reported that the geothermal gradient of the South African platinum mines is about twice that of the gold mines. Biffi *et al* (2007) also pointed out that the rock mass being mined in the platinum mines, mainly norites, cool faster than quartzite, which is the major host rock in the West Witwatersrand Basin.

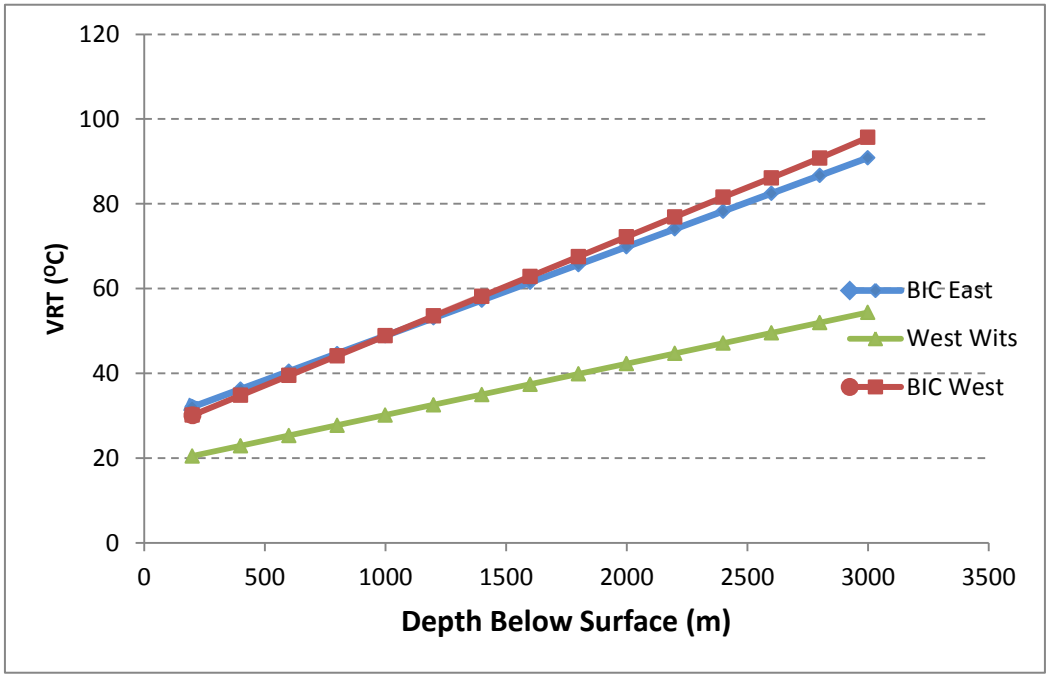


Figure 2.19: Geothermal gradient of the Witwatersrand Basin and BIC (Biffi *et al*, 2007)

Figure 2.19 also shows that the western BIC has higher virgin rock temperature than the eastern BIC.

2.3 Thermal properties of rocks

Mares and Tvrdy (2011) stated that the flow of heat is from the Earth's interior to the surface. The sources of this heat are:

"(a) decay of radioactive elements (radiogenic heat)
(b) geothermal exothermic reactions by the compression of the overlying beds (gravitational heat)
(c) tectonic movement and absorption of seismic wave energy" (Mares and Tvrdy, 2011).

The above stated sources are the sources of heat within the earth prior to interference by mining activities. Hartman *et al*. (2012) listed the contributors of heat in the underground mines as autocompression, wall rock, underground water, mine machinery and lights, human metabolism, oxidation, blasting, rock movement and pipelines. Payne and Mitra (2008) gave the percentage contributions of the sources as shown in Figure 2.20.

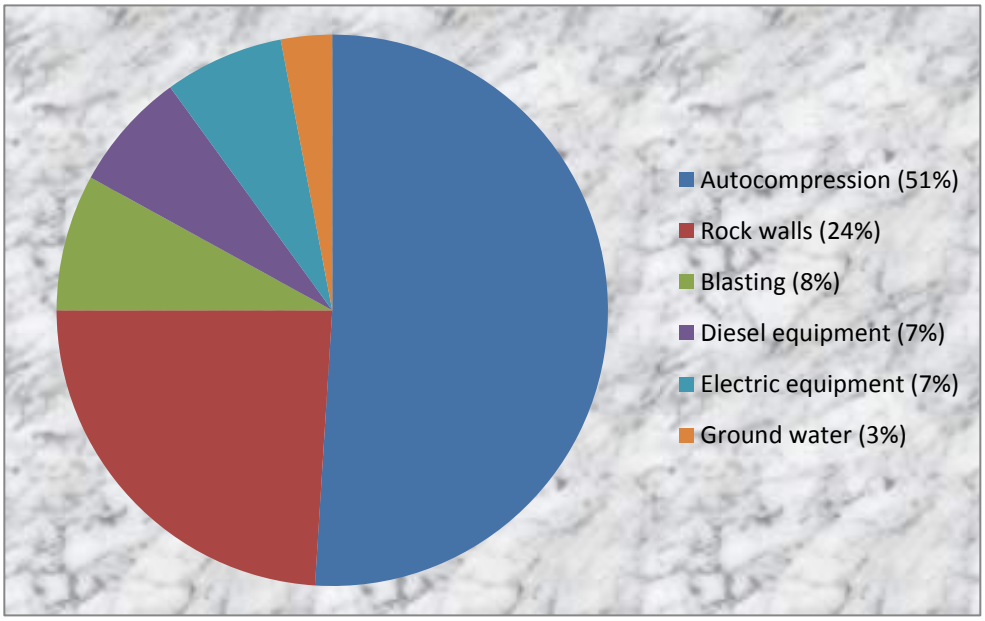


Figure 2.20: Percentage contributions of heat sources in underground mines (Payne and Mitra, 2008)

Different heat sources contribute to the heat load in the underground mines. The accumulated heat from theses sources is reduced to underground working temperature (approximately 27°C) through ventilation for worker's comfort. The ventilation of the mine openings will lead to cooling of the excavation skin, while the inner part of the rock remains hot. This results in temperature differential between the surface and the rock interior. The process of cooling of the warm rock occurs at different magnitudes at different depths due to varying virgin rock temperatures.

Clauser and Huenges (1995) explained that the interior heat of the earth is transmitted to its surface by conduction, radiation and advection. Conduction refers to the transfer of heat energy directly from atom to atom along a temperature gradient. It can be in gas, liquid or solid state. The transfer of heat energy by the vertical movement of a mass of gas or liquid is called convection. Radiation, on the other hand, refers to the transfer of heat energy across empty void of outer space. In underground working

environment, heat radiates from the walls of the rock into the excavated void, cooling of the openings occur through convection and advection, while the movement of heat energy from the rock interior to the cooled surface is through conduction. This research will mainly investigate the influence of the temperature differential on the stability of the skin of underground excavations.

Clauser and Huenges (1995) stated that the thermal conductivity of igneous rocks are isotropic while the thermal conductivity of sedimentary and metamorphic rocks display anisotropy. Clauser (2011a) observed that the thermal regime of the earth is given by its heat sources and sinks, transport processes and heat storage, and the equivalent transport and storage properties. The heat storage properties are heat capaicty and latent heat, while the transport properties are thermal conductivity and diffusivity.

Thermal diffusivity, k, is the ratio of thermal conductivity and heat capacity as given in equation 2.1. It governs transient heat diffusion (Clauser, 2011b).

$$k = \frac{\lambda}{c\rho} \qquad (2.1)$$

Where k = thermal diffusivity (m^2/s),

λ = thermal conductivity (W/m.K),

ρ = density of rock (kg/m^3),

c = specific heat capacity (J/kg.K).

and

$$c = \frac{\Delta Q}{m\Delta T} \qquad (2.2)$$

Where ΔQ = heat required, (J)

m = mass of rock (kg)

ΔT = change in temperature (K)

The specific heat capacity is defined as the amount of sensible heat which can be stored in or extracted from a unit (1 kg) mass of rock per unit (1 K) temperature increase or decrease (equation 2.2) (Clauser, 2011a).

Thermal conductivity refers to the amount of heat that flows across a unit cross-section (m^2) of rock along a unit distance (m) per unit temperature decrease (K) per unit time. It governs heat diffusion in the steady state (Clauser, 2011b).

Horai and Baldridge (1972) asserted that measurement of thermal conductivity of rocks is important in the determination of values of heat flow in the Earth's crust. Hirono and Hamada (2010) affirmed that thermal properties of rocks, such as, specific heat capacity and thermal diffusivity are fundamental parameters in the evaluation of the influence of heat on rock deformation using numerical analyses.

Mares and Tvrdy (2011) stated that among the common minerals, feldspars are the worst conductors of heat with thermal conductivity of 2.5 W/m.K, while quartz is one of the best conductors with thermal conductivity of 8.37 W/m.K. The range of thermal conductivities of most rocks within the Earth's crust is 2.09 to 4.19 W/m.K and most of them do not show any distinct anisotropy.

Figure 2.21 to 2.23 show the relationship between thermal properties of rocks and temperature. From the figures, it is observed that only specific energy increases as temperature increases, thermal conductivity and thermal diffusivity values decrease with increase in temperature.

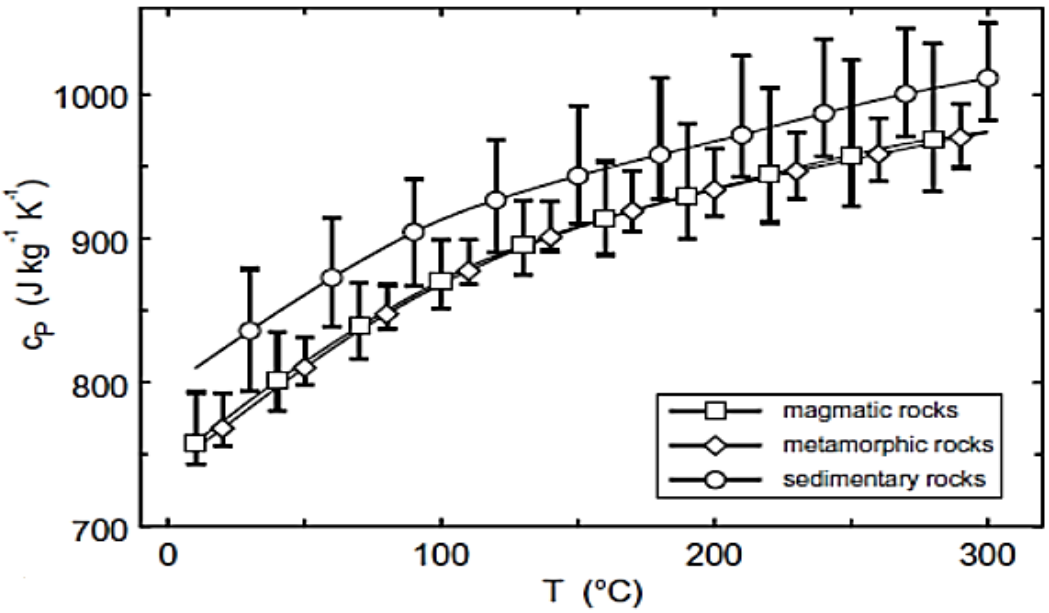


Figure 2.21: Graph of specific heat capacity against temperature (Vosteen and Schellschmidt, 2003)

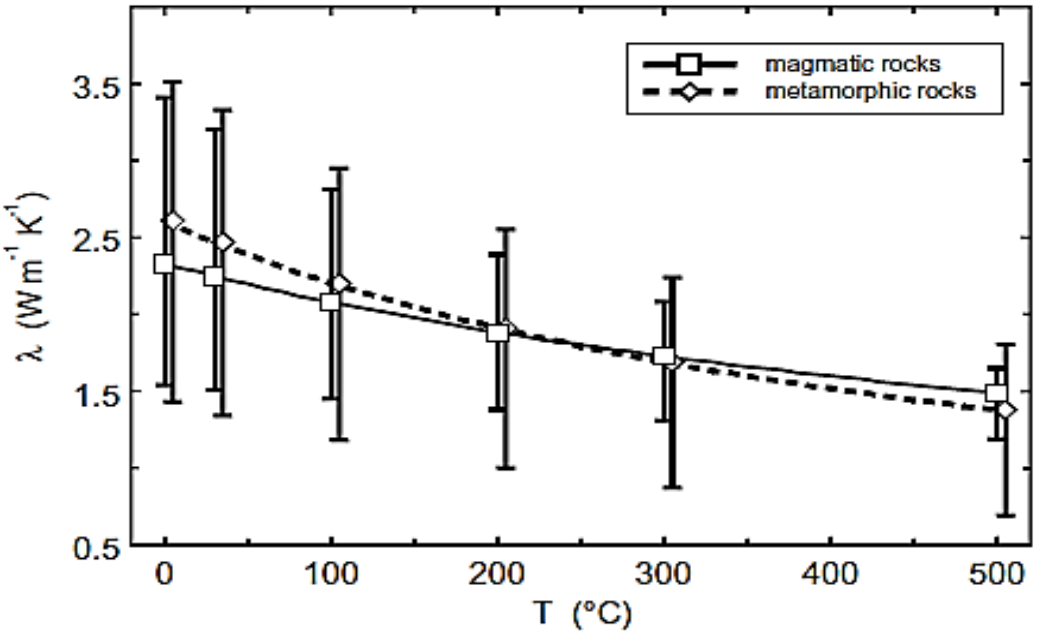


Figure 2.22: Graph of thermal conductivity against temperature

(Vosteen and Schellschmidt, 2003)

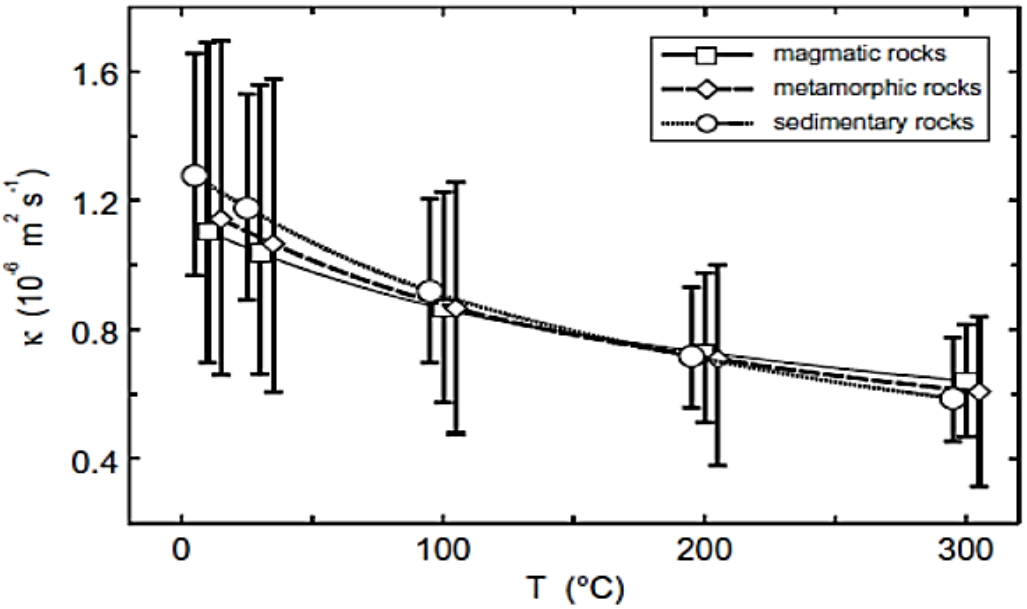


Figure 2.23: Graph of thermal diffusivity against temperature (Vosteen and Schellschmidt, 2003)

Coefficient of thermal expansion is another important parameter that is used to evaluate the response of rock to variation in temperature. It can be linear or volumetric. The linear coefficient of thermal expansion, α, is the ratio of change in length to the original length per unit of temperature change, as expressed in equation 2.3.

$$\alpha = \frac{\Delta l}{\Delta T} . \frac{1}{l} \qquad (2.3)$$

Where,

Δl = change in length of the rock specimen

ΔT = change in temperature

l = original length of the rock specimen

Equation 2.4 gives the volumetric coefficient of thermal expansion, β, which is the ratio of change in volume to the original volume per unit of temperature change, as expressed in equation 2.4.

$$\beta = \frac{\Delta v}{\Delta T} . \frac{1}{v} \qquad (2.4)$$

Where,

Δv = change in volume of the rock specimen

ΔT = change in temperature

v = original volume of the rock specimen.

Huotari and Kukkonen (2004) stated the relationship between the linear and volumetric coefficient of thermal expansion as:

$$\beta = 3\alpha \qquad (2.5)$$

According to Siegesmund *et al*. (2000), thermal expansion of rocks are influenced by properties such as mineral composition, texture, porosity, properties of fluid in pores, micro-cracks, pressure and temperature.

Wong and Brace (1979) studied the effect of confining pressure on the coefficient of thermal expansion of quartzite and limestone. They affirmed that coefficient of thermal expansion decreases with increasing confinement as shown in Figure 2.24. This is due to higher confining pressures that impede crack formation and extension.

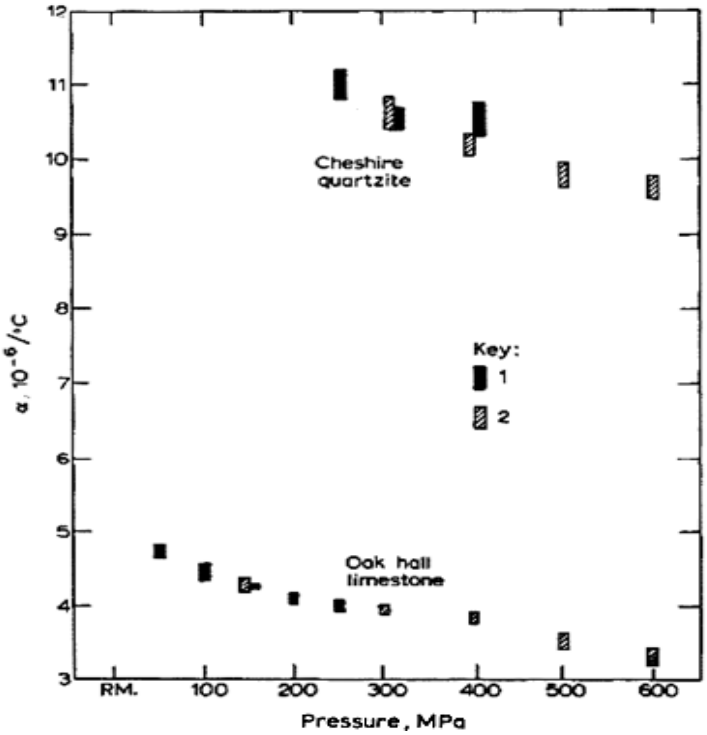


Figure 2.24: Influence of confining pressure on thermal expansion- when pressure was (1) decreased and (2) increased (Wong and Brace, 1979)

From Figure 2.24, it is observed that though higher confining pressure caused reduction in the coefficient of thermal expansion, however, effect is insignificant, except at higher pressure, above 600 MPa. For example, a pressure increase of 100 MPa only yields 5% reduction in the coefficient of thermal expansion.

Cooper and Simmons (1977) explained that changes in temperature result in two types of cracks: (a) thermal cycling cracks generated due to inhomogeneous strain by the mismatch of thermal expansion boundaries, (b) thermal gradient cracks produced due to inhomogeneous strain resulting from differential temperature. Table 2.5 shows the effect of temperature on the coefficient of linear thermal expansion, α, of some rocks. It is obvious from the table that the values of α increase when tested at higher temperature range, that is 35-60°C, except for porfyric granodiorite. Table 2.6 shows the volumetric and linear thermal expansion coefficient of some rocks. Looking at the values of α in Tables 2.5 and 2.6, it is observed that the α may vary within the rock

types in the igneous, sedimentary or metamorphic rocks. Huotari and Kukkonen (2004) explained that such variation may be attributed to changes in texture, constituent minerals, mineral proportions, pore space, grain sizes, orientation of minerals and fractures.

Table 2.5: Thermal expansion of some rocks with increasing temperature (Kjørholt, 1992)

Average coefficient of linear thermal expansion, α (10^{-6} per°C)				
Rocks	**Rock type**	**10-35**°C	**35-60**°C	**10-60**°C
Tonalite gneiss	Metamorphic	6.6	9.7	8.1
Mica gneiss	Metamorphic	8.2	10.9	9.5
Tonalite	Igneous	6.6	8.8	7.7
Porfyric granite	Igneous	7.3	10.4	8.8
Porfyric granodiorite	Igneous	9.3	8.1	8.7

Table 2.6: Volumetric and linear thermal expansion coefficient of some rocks (Robertson, 1988)

Rocks	**Rock type**	**Volumetric thermal expansion coefficient β (10^{-5} per °C)**	**Linear thermal expansion coefficient α (10^{-6} per °C)**
Granite, Rhyolite	Igneous	2.4	8.0
Diorite, andesite	Igneous	2.1	7.0
Gabbro, basalt	Igneous	1.6	5.3
Sandstone	Sedimentary	3.0	10
Limestone	Sedimentary	2.4	8.0
Marble	Metamorphic	2.1	7.0
Slate	Metamorphic	2.7	9.0
Quartzite	Metamorphic	3.3	11

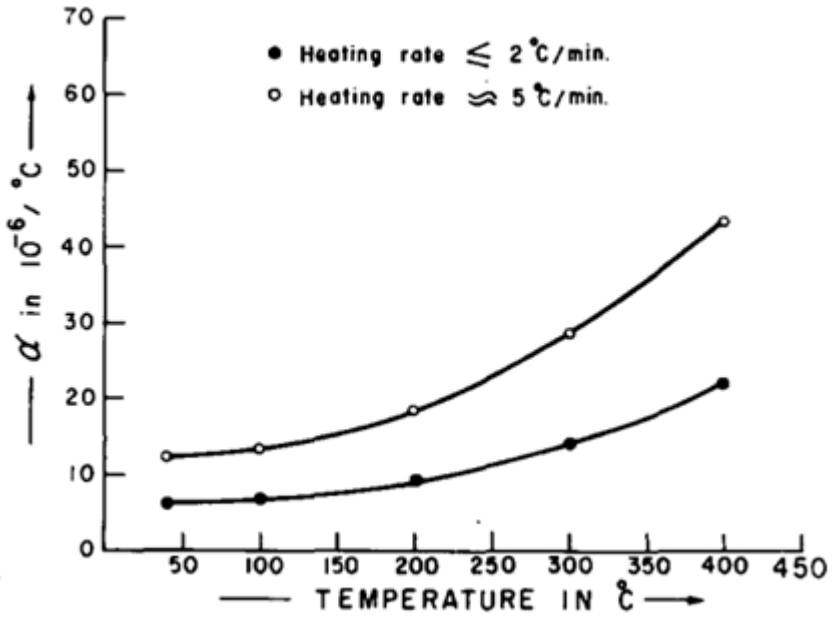


Figure 2.25: Effect of temperature and heating rate on coefficient of thermal expansion of granite (Ramana and Sarma, 1980)

Figure 2.25 shows that α increases with increasing temperature. It also shows that heating rate has significant influence on the expansion of rocks. According to Richter and Simmons (1974), thermal expansion of rock is affected by heating rate and presence of micro-cracks in the sample. They suggested that heating rates not greater than 2°C/min are required for precise measurement of thermal expansion to eliminate cracking due to stress produced by thermal gradient.

In this research, heating rate of 2°C/min was used for detremination of the linear and volumetric coefficient of thermal expansion.

2.4 Review of laboratory test methods for rocks applicable in this research

The review of experimental procedures for tensile and compression tests are provided below:

1. Indirect measurement of tensile strength
2. Compressive tests
3. Measurement of thermal expansion

2.4.1 Measurement of indirect tensile strength

Cai (2010) stated that tensile fracturing under loading is unstable. He noted that for brittle rocks, such as norite, under tensile loading, the stress levels of crack initiation and propagation (defined as the stress level at which coalescence occurs) are very close to the peak strength. Based on the difficulties associated with performing a direct uniaxial tensile test on rock, a number of indirect tensile testing methods, such as bending (beam) and Brazilian tests have been developed. Cai (2010) affirmed that the most common of these methods is the Brazilian test, which involves loading of a cylindrical sample diametrically between two platens until failure is achieved.

According to ISRM (1978), the justification for the indirect tensile testing is due to the fact that most rocks in biaxial stress fields fail in tension when one principal stress is tensile and the other one is compressive with a magnitude not more than three time that of the tensile strength. The apparatus for the Brazilian test are two steel loading jaws and suitable machine capable of measuring and applying compressive loads to the specimen. The steel loading jaws (Figure 2.26) are designed such that they contact a disc-shaped rock sample at diametrically -opposing surfaces over a line of contact.

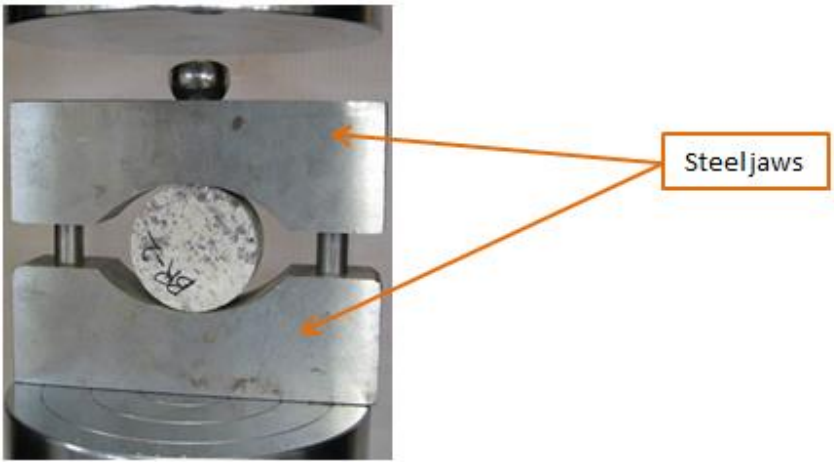


Figure 2.26: Apparatus for Brazilian test

The tensile strength, σ_t, is calculated from:

$\sigma_t = 0.636\ P / Dt$ (MPa) (2.6)

Where P is the load at failure (N),

D is the diameter of the test specimen (mm) and

T is the thickness of the test specimen (mm)

2.4.2 Laboratory compressive tests

Compression tests are intended for classification and characterization of intact rocks. The deformability, strength and failure mode of intact rock are critically important for understanding the basic mechanics of excavation and support requirement. Rock properties, such as, Young's modulus, Poisson's ratio, and strength are derived from unconfined and triaxial compression tests. In addition, shear strength (cohesion and angle of internal friction) are obtained from triaxial compression tests (Li *et al.*, 2012).

The uniaxial compression test is performed by taking a right cylinder of intact rock, loading it along its axis and recording the force and displacement produced as the force is increased. The test can be done with a soft or stiff testing machine. If a soft testing machine (such as Amsler compression testing machine, Figure 2.27) is used, the post-peak region of the stress-strain curve could not be obtained. However, if done with a stiff testing machine (such as MTS servo-controlled testing machine, Figure 2.28) a complete stress-strain curve will be obtained, showing the post-peak and residual stress and strains of the specimen. Tarasov and Potvin (2013) stated that the advantage of having a complete stress-strain curve is that informative characteristics of intrinsic material properties, before and after the peak stress is reached, can be obtained.

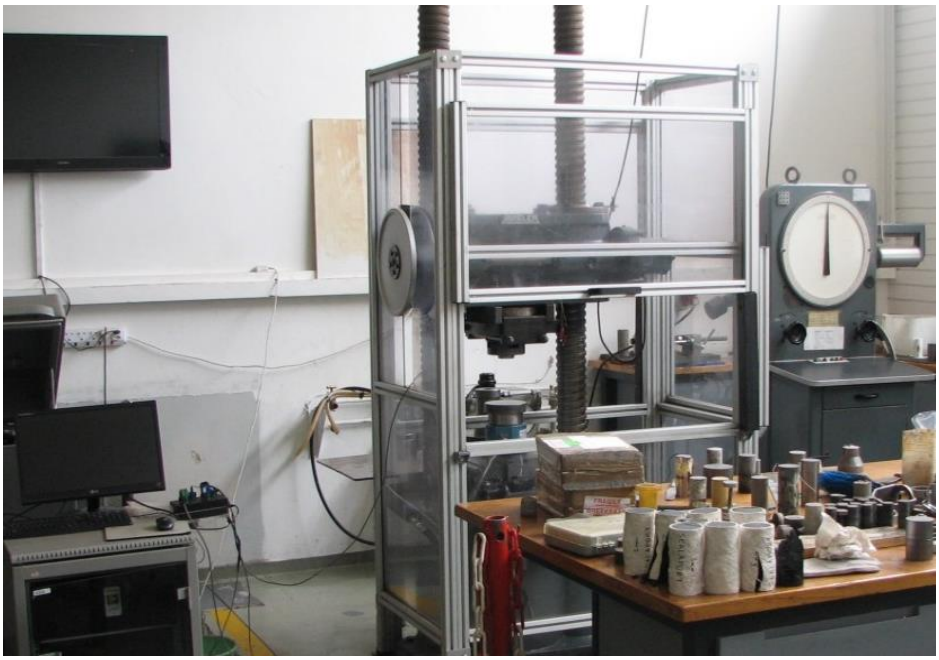


Figure 2.27: Amsler compression machine

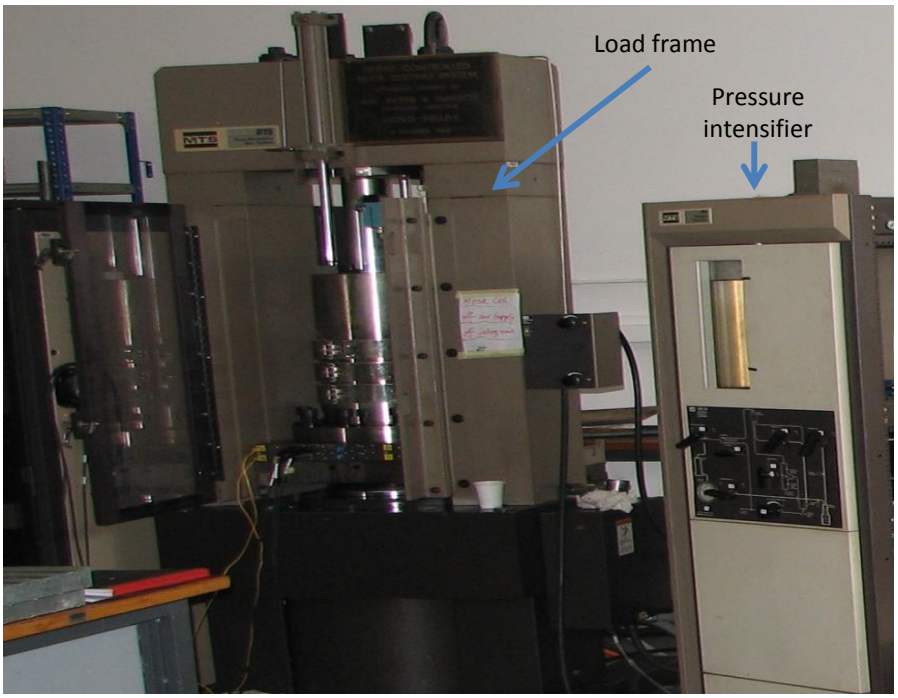


Figure 2.28: Servo-controlled testing machine and pressure intensifier

2.4.2.1 Components of the servo-controlled testing machine for triaxial testing.

The servo-controlled testing machine consists of the following components:

1. Load frame: The load frame (Figure 2.28) is designed for uniaxial and triaxial testing with particular attention to studies on post failure behaviour. The assembly consists of a fixed crosshead mounted on two rectangular columns which are bolted to the base, providing a high loading capacity in a stiff frame. When a triaxial cell is inserted into the test space, the load frame assembly applies axial stress to the specimen inside the cell. The load cell (Force transducer) is MTS 315.02 with maximum loading capacity of 2600 kN, which is accurate to within ±0.5% of the calibrated range (MTS, 2001).

2. Hydaulic power unit (HPU): The HPU (Figure 2.29 (a)) provides the high-pressure hydraulic fluid during test execution. The unit automatically starts in a low pressure of 1 MPa however can be increased up to 21 MPa. The unit also has a water-cooled heat exchanger which maintains the temperature of the hydraulic fluid.
3. Actuator Manifold and Servovalve: According to MTS, (2001) Actuator Manifold functions as the mounting block between the servo-valve and hydraulic actuator. It is designed to provide flexibility by offering a selection of pressure controls. Servo-valves (Figure 2.29 (b)) function as the final regulating element in a servo hydraulic test system by controlling the direction and rate of flow of the hydraulic fluid to the actuator.



(a) (b)

Figure 2.29: Servo-controlled machine support systems (a) Hydraulic Pump Unit (b) Servo-valves

4. Triaxial Cell Assembly: The triaxial cell assembly (Figure 2.30) is used to simulate in-situ rock conditions, in terms of stresses and temperature on rock specimen in order to investigate the effects of changes to these factors. The

features of the MTS 793 triaxial cell includes; hydraulic lifts for easy and quick raising and lowering of the cell, in-vessel spherical seats for proper specimen alignment, confining cell with a capacity of 140 MPa, heating element and temperature control package for simulation of in-situ temperature from -10°C to +200°C. The range of temperature used for this research was between ambient (approximately 20°C) and 140°C. The extensometers are limited to operate at a maximum operating temperature of 150°C (MTS, 2001). The pressure vessel, when lowered onto the base plate forms a sealed pressure chamber for the specimen and extensometer assembly. Ten cap screws hold the pressure vessel to the base plate. The extensometer cables connect to the feed-throughs in the base plate (Figure 2.30).

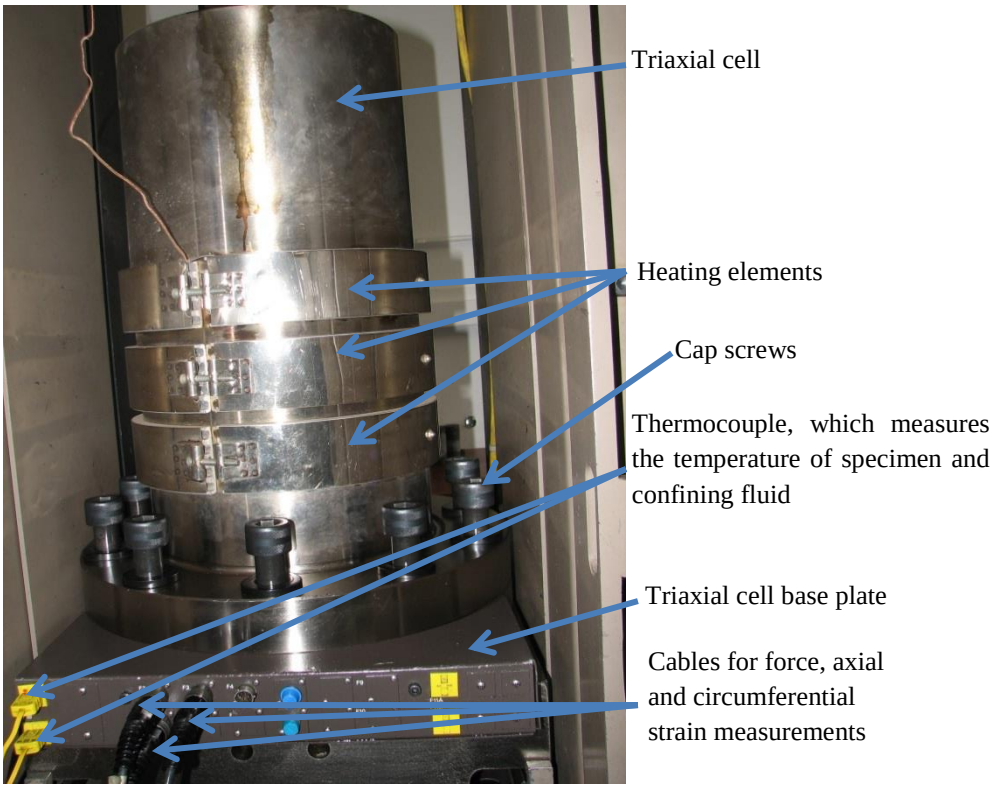


Figure 2.30: Parts of MTS servo-controlled triaxial cell

5. Confining pressure intensifier: It has a transparent reservoir for easy visual of fluid condition and level, in addition to an integral air pump. It is used for filling and pressurizing the triaxial cell (Figure 2.28). It also provides servo-control of the confining fluid in the triaxial cell (MTS, 2001).
6. Control System: MTS, (2001) stated that the control system used with the MTS 815 machine is MTS Flex 60 Controller. It provides real-time closed-loop control, with transducers conditioning and function generation to drive various types of servo-actuators. The system software bundles contain applications that perform activities centered around maintaining servo control of a test. These applications are; project manager, station builder, station manager and Multi-Purpose Testware (MPT).
7. Extensometers: Two types of extensometers were used. The axial extensometer measures strain over clearly defined gauge length. The axial extensometer used is MTS 632.90F (Figure 2.31), that has an axial gauge length of 50 mm. Its extension range is between 0.1 mm/mm and -0.05 mm/mm. Jacket effect was minimized through the use of heat-shrink teflon jackets. The second extensometer is of circumferential type used for measuring the overall circumferential strain (Figure 2.31). It has a capacity of extending by 15%. Both the axial and the circumferential extensometers are attached to the specimen before the pressure vessel is lowered as shown in Figure 2.31.

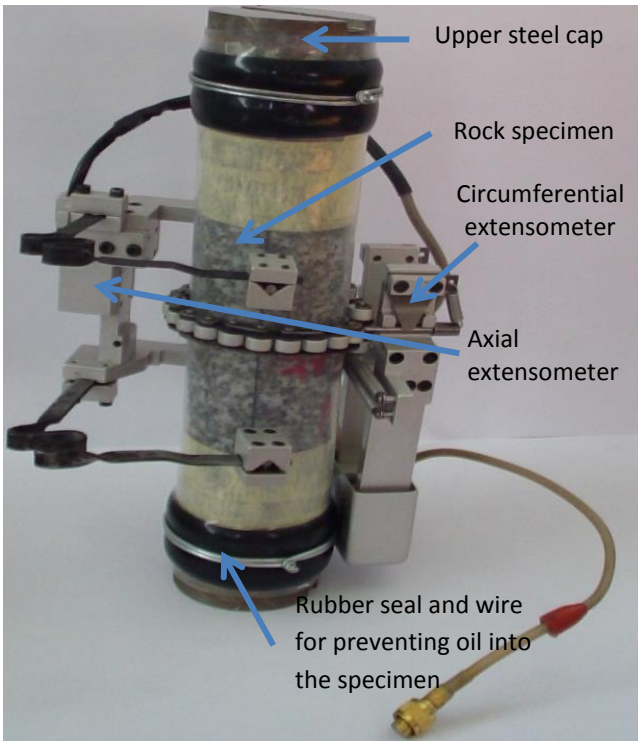


Figure 2.31: Axial and circumferential extensometers attached to norite specimen – ready for testing

Uniaxial compressive strength can be calculated by dividing the peak load applied to the specimen during the test by the original cross-sectional area. Axial tangential Young's modulus at 50% of uniaxial compressive strength, E_t, was calculated as the slope of tangent line of axial stress-axial strain curve.

Poisson's ratio (υ) at 50% of uniaxial compressive strength is calculated as:

$$\mathrm{v} = \left| -\frac{\text{slope of axial stress vs strain curve}}{\text{slope of lateral stress vs strain curve}} \right| \tag{2.7}$$

The bulk and the shear moduli were calculated from the formula below:

$$K = Bulk\ Modulus = \frac{E}{3(1-2v)} \tag{2.8}$$

$$G = Shear\ Modulus = \frac{E}{2(1+v)} \tag{2.9}$$

2.5 Class I and Class II post-peak behaviour of rocks

Based on the uniaxial quasi-static compression tests conducted by Wawersik and Fairhurst (1970), the complete stress-strain characteristics of the rocks studied are divided into Class I and Class II (Figure 2.32). Fracture propagation is stable in Class I and work must be done on the sample for each incremental decrease in load-carrying ability. For Class II, failure is unstable or self-sustaining; elastic energy must be extracted from the material in order to control fracture. Complete stress-strain curves of Class I rocks can be obtained using a servo-controlled stiff testing machine by selecting strain as the feedback signal. Class II rocks, however, will continue to fail just after reaching the peak stress-strain curves even if strain is kept constant as shown in Figure 2.32 (Okubo and Nishimatsu, 1985).

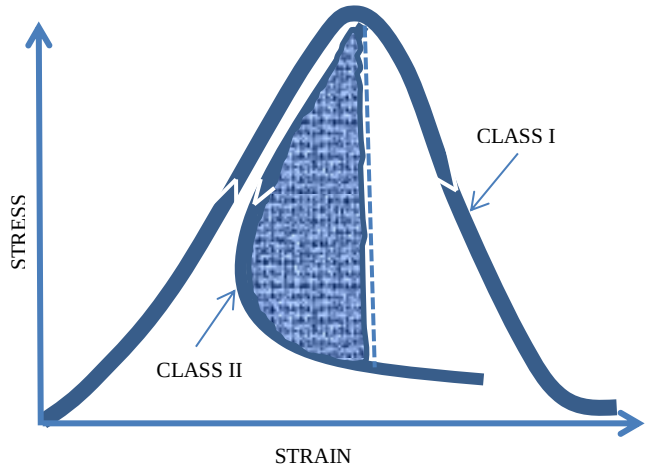


Figure 2.32 : Complete stress-strain curves of rocks showing Class I and Class II behaviour (ISRM, 1999)

Reseachers (Hudson *et al*, 1971; Okubo and Nishimatsu, 1985) have used different feedback signal or independent variables such as lateral displacement, acoustic emission rate, linear combination of stress and strain to study the post-peak behaviour of the Class II type rocks. In order to ensure reproducibilty of post-failure behaviour from sample to sample, Wawersik and Brace (1971) stated the important conditions that must be made constant as confining pressure, strain-rate, temperature and moisture content. In this research, strain rate, and moisture content are kept constant, while the confining pressure and temperature are varied.

Tarasov (2014) stated that Class I type rock is characterised by negative post-peak modulus, while Class II rock has positive post-peak modulus (Figure 2.29).

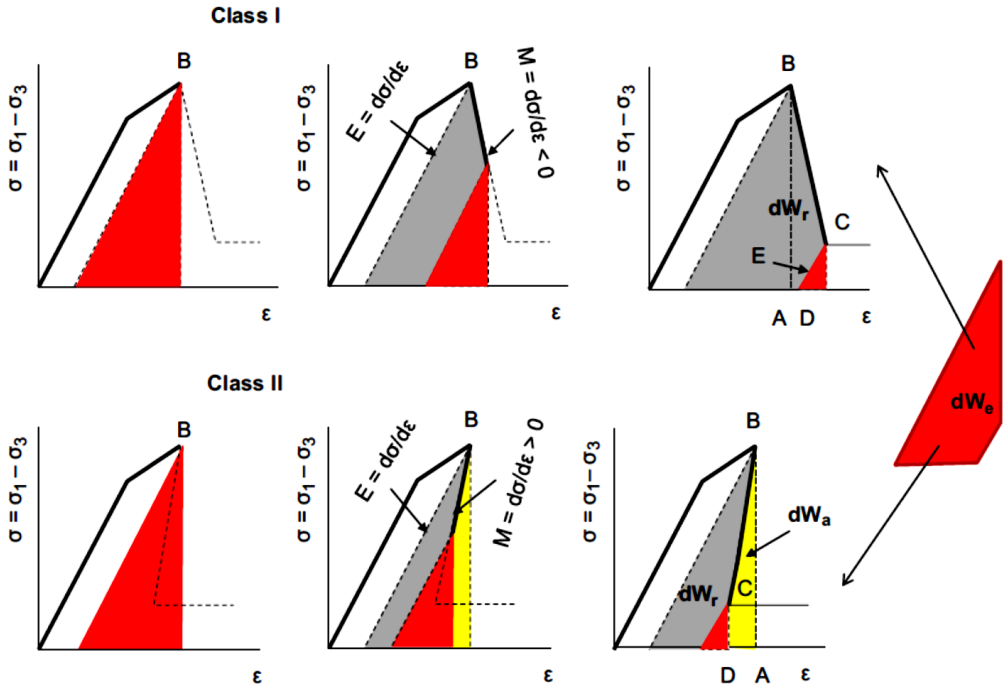


Figure 2.33: Illustration of the post-peak energy balance for rocks of Class I and II behaviour (Tarasov and Potvin, 2013)

The post-peak modulus, M, is given as:

$$M = d\sigma/d\varepsilon \qquad (2.10)$$

Where, σ is the differential stress (σ_1- σ_3) and

ε is the axial strain.

He *et al* (1990) noted that above a certain confining pressure, rock which shows Class I behaviour in triaxial condition changes to Class II. Tarasov and Potvin (2013) also affirmed that recent researches showed that increasing confining pressure lead to rock behaviour changing from Class I to Class II and then to Class I again. In the conventional behaviour (Figure 2.34 (a)), the behaviour of the rock is Class I type irrespective of the increasing confining pressure. However, in the case of the

unconventional behaviour, (Figure 2.34 (b)), at lower confining pressure, rocks in this category display Class I behaviour, with increasing confining pressure, the behaviour changes to Class II and with further increase in the level of confinement, it reverts to Class I.

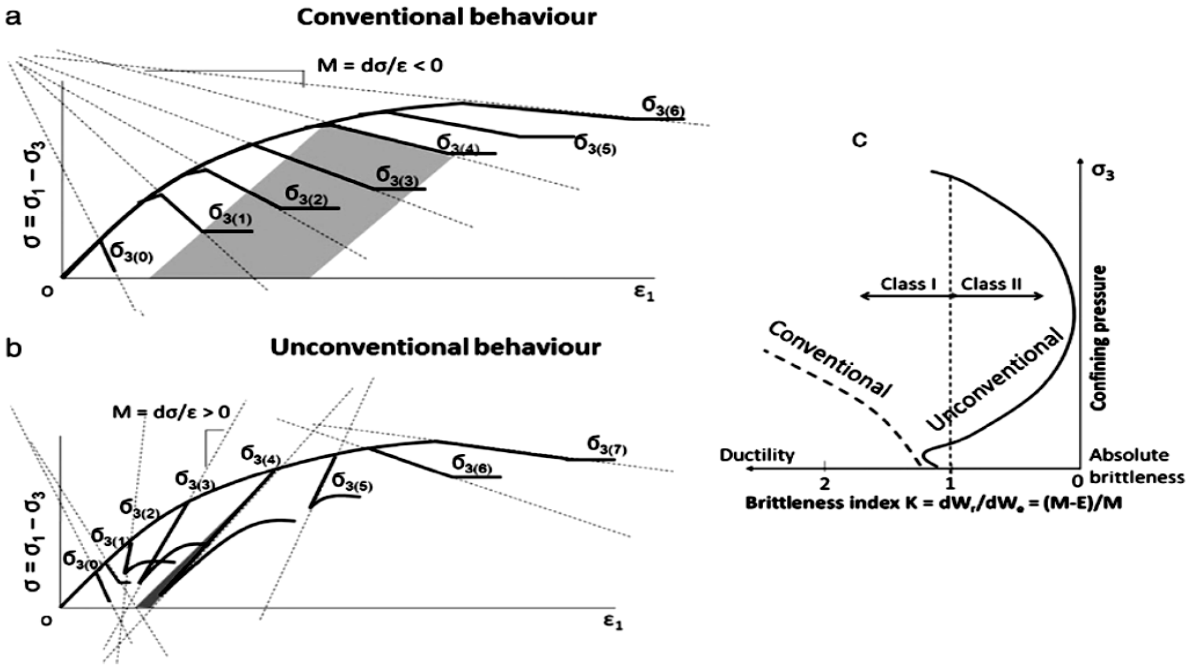


Figure 2.34: Generic stress-strain curves for different levels of confining pressure σ_3 showing (a) conventional (b) unconventional rock behaviour. (c) Typical variation of the post-peak brittleness index K with rising σ_3 for rocks displaying the conventional and unconventional behaviour (Tarasov, 2014)

It should be noted that there is no specific universal boundary value for the confining pressure that caused this transition for rocks with this type of behaviour. This imply that the transition will be dependent on the rock types. Tarasov (2014) reported tests conducted on dolorite specimen, with UCS of 300 MPa at confining pressure range of 0 to 150 MPa. The result of his tests showed that the specimens exhibit Class I

behaviour at confining pressure of 0 and 30 MPa, while at higher confining pressure up to 150 MPa, Class II behaviour was observed.

Tarasov (2014) also pointed out that at confining pressure less than 60 MPa, the total post-peak control was provided for both Class I and Class II behaviours for dolerite. However, at confining pressure ≥ 60 MPa, control was only possible at the beginning of the post-peak stage, after which spontaneous and violent failure took place. In Figure 2.34 (c), the post-peak brittleness index, $K = dW_r / dW_e = (M-E) / M$, is based on the ratio between the post-peak rupture energy 'dW_r' and elastic energy 'dW_e' withdrawn from the material during the failure process.

2.6 Measurement of coefficient of thermal expansion

According to Battaglia *et al*. (1993), thermal expansion of rocks can be measured through static or dynamic testing methods. In a static procedure, the specimen is heated up to the temperature of interest and kept constant for a certain time until thermal equilibrium is achieved. The variation of length that takes place during the passage from one temperature to the other is subsequently recorded. In a dynamic procedure, the temperature is varied continuously and the variation of length is simultaneously measured.

Some of the methods of thermal expansion measurement, as given by Wong and Brace (1979), are dilatometer, inter-ferometric, optical comparator, and X-ray diffractometric methods. Several investigators (Battaglia *et al*., 1993; Huotari and Kukkonen, 2004; Richter and Simmons, 1974) used dilatometers to study linear or volume change of rocks in experiments for determination of coefficient of thermal expansion. Huotari and Kukkonen (2004) explained that the measuring system of a dilatometer consisted of a furnace, thermocouple, sample holder and a linear variable displacement transducer (LVDT).

In this study, the coefficient of thermal expansion of rocks is measured with MTS servo-controlled, MTS criterion testing machines and MTS video extensometer. The detail of the experimental procedure is given in Chapter 3.

2.7 Determination of dilation angles (ψ) from laboratory triaxial test

Dilation angle, represented by ψ, is the parameter used for describing how dilatant a material is. The dilation angle is derived from the ratio of plastic volume change to plastic shear strain. This angle is typically determined from triaxial tests or shear box tests. In a triaxial test, the volumetric strain is defined as a measure of the change in volume per unit volume of the material. In other words, it is the sum of the normal strains (Vermeer and de Borst, 1984).

In plane strain analysis, volumetric strain, ε_v, is expressed as:

$$\varepsilon_v = \varepsilon_{xx} + \varepsilon_{yy} = \varepsilon_1 + \varepsilon_2 \quad (2.11)$$

Where, ε_1 and ε_2 are principal strains.

In a triaxial test, the volumetric strain is expressed in terms of the axial strain (ε_a) and radial strain (ε_r).

$$\varepsilon_v = \varepsilon_a + 2\varepsilon_r \quad (2.12)$$

The concept of dilatancy is important since it gives an indication of possible occurrence of earthquakes, mine collapse and mining-induced rock bursts (Kwaśniewski and Rodríguez-Oitabén, 2012). Generally, a more dilatant material will show a greater volume increase.

Vermeer and de Borst (1984) gave a bilinear graph of a triaxial test and a plot of volumetric strain versus axial strain in order to derive the formula for calculating the dilation angle as shown in Figure 2.35.

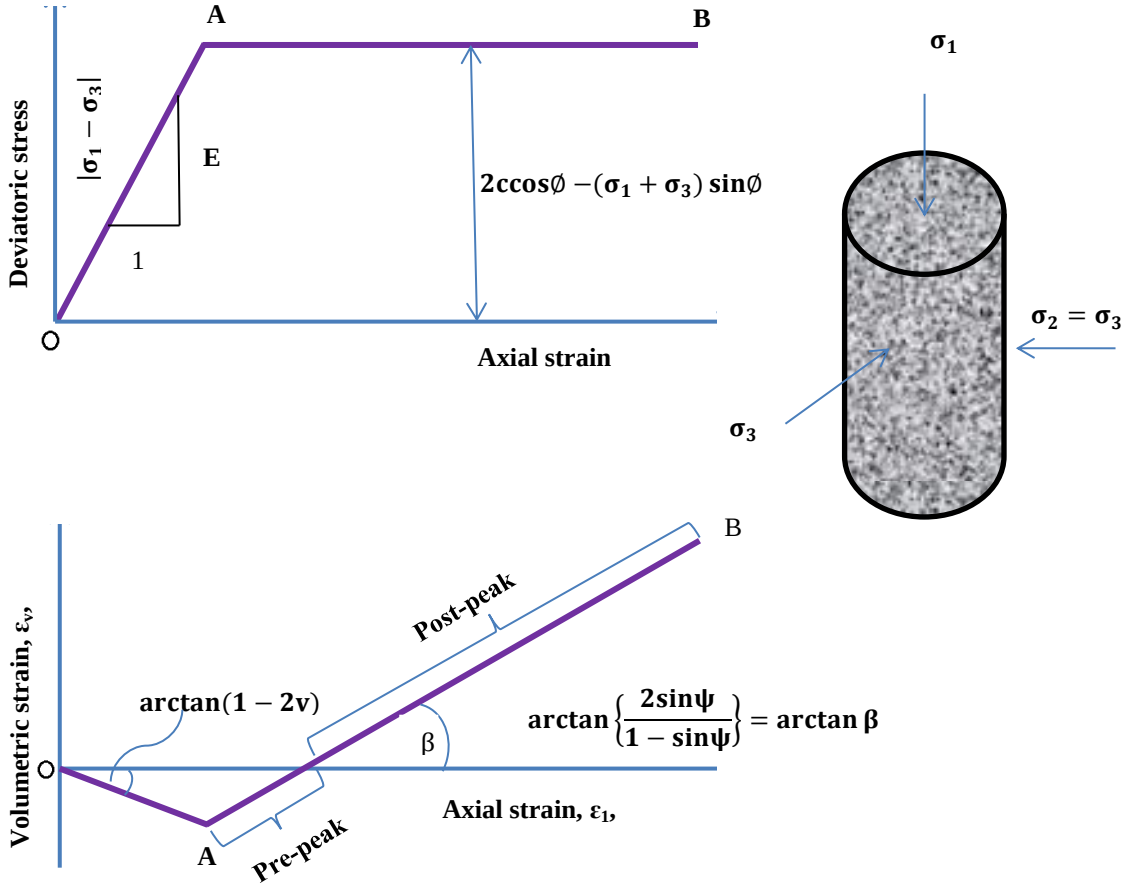


Figure 2.35: Bilinear idealization for determination of dilation angle
(after Vermeer and de Borst, 1984)

It should be noted that the initial slope of the deviatoric stress versus axial strain plot in Figure 2.35 corresponds to the elastic region (OA) while the slope used for the calculation of the dilation angle is that of the plastic region (AB).

Using the idealized relation for dilation angle, the value of ψ is calculated from the slope (β) of the volumetric strain versus axial strain as:

$$\psi = \arcsin\left(\frac{\tan\beta}{-2+\tan\beta}\right) \qquad (2.13)$$

Another equation given by Vermeer and de Borst, (1984) which relates ψ to the volumetric plastic strain rate ($\dot{\varepsilon}_v^p$) and axial plastic strain rate ($\dot{\varepsilon}_1^p$) is

$$\psi = \arcsin\left(\frac{\dot{\varepsilon}_v^p}{-2.\dot{\varepsilon}_1^p + \dot{\varepsilon}_v^p}\right) \quad (2.14)$$

The equation was established with soil mechanics sign convention, where compression is negative and extension is positive. That is the reason for the negative sign in the denominator. In rock mechanics sign convention, the reverse is the case, therefore, equation 2.14 becomes,

$$\psi = \arcsin\left(\frac{-\dot{\varepsilon}_v^p}{2.\dot{\varepsilon}_1^p - \dot{\varepsilon}_v^p}\right) \quad (2.15)$$

Dividing the numerator and denominator by $\dot{\varepsilon}_1^p$ in equation 2.15 gives,

$$\psi = \arcsin\left(\frac{-\dot{\varepsilon}_v^p/\dot{\varepsilon}_1^p}{2 - \dot{\varepsilon}_v^p/\dot{\varepsilon}_1^p}\right) \quad (2.16)$$

The slope of $\dot{\varepsilon}_v^p/\dot{\varepsilon}_1^p$ in Figure 2.29 is tan β, which brings equation 2.16 to

$$\psi = \arcsin\left(\frac{-\tan\beta}{2 - \tan\beta}\right) \quad (2.17)$$

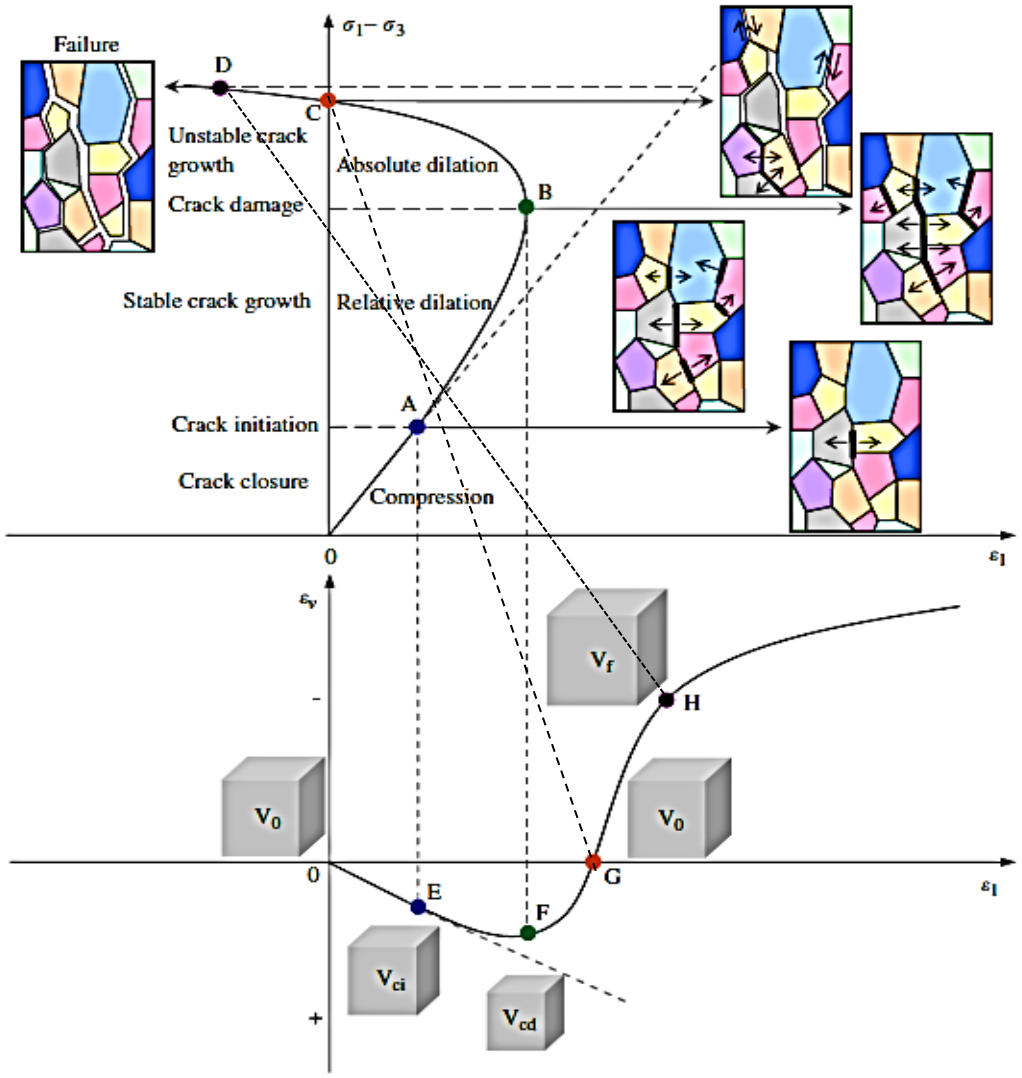
Kwaśniewski and Rodríguez-Oitabén (2012) stated that the dilation angle, characterizing the dilatant behaviour of rocks in the pre-failure domain can be determined using tan β in equation 2.17. Since the gradient of the volumetric strain to axial strain is the key parameter in the equation, the same equation is used in calculating the dilation angles in the pre-peak, post-peak and residual stages of rock deformation in this research. The only exception is that in calculating the post-peak dilation angle for Class II type rock, negative sign is introduced because of the negative gradient.

Alejano and Alonso (2005) asserted that correct estimation of dilatancy is of paramount interest in resolving certain post-peak rock mechanics issues, such as the

practical problem of modelling underground excavations. According to Finzi *et al*. (2013), when experimenting with moderate or high confining stress, dilation is observed only after the shear band forms and starts propagating. They also pointed out that for non-porous rocks at relatively high confining pressure, pre-failure volumetric changes are small and highly depend on the stress state. They explained that at moderate to high confining pressure, shear-induced dilation and elastic and inelastic compaction processes, such as, distributed grain crushing and pore collapse, could coexist and interact to form compacting shear band and conjugate shear bands. They concluded that where dilation occurs, it enhances damage accumulation and material weakening which causes further strain localization and deformation, that is, dilation and shear.

Many researchers (Martin *et al*, 1997; Kaiser *et al*, 2000; Cai *et al*, 2001) have stated that spalling and slabbing are the prevalent failure mode around underground excavations in hard brittle rocks where in-situ stresses are high. According to Cai, (2008), rock fracturing usually starts at the excavation boundary where the tangential stress is highest and then propagates to the deeper ground. This implies that rock mass dilation will be highest close to the boundary and relaxes away from the excavation due to higher confining stress.

Kwaśniewski and Rodríguez-Oitabén (2012) emphasized the importance of determining the dilation angle of rock at the pre-failure domain, that volumetric expansion of the compressed rock starts at relatively early stages of the deformation process in the pre-failure region. Zhao and Cai (2010a) represented dilation in relation to crack initiation, growth and coalescence pictorially in Figure 2.36.



V_o: Original volume, V_{ci}: Crack initiation volume, V_{cd}: Crack damage volume, V_f: Failure volume

Figure 2.36: Dilation in relation to crack initiation, growth and coalescence (Zhao and Cai, 2010a)

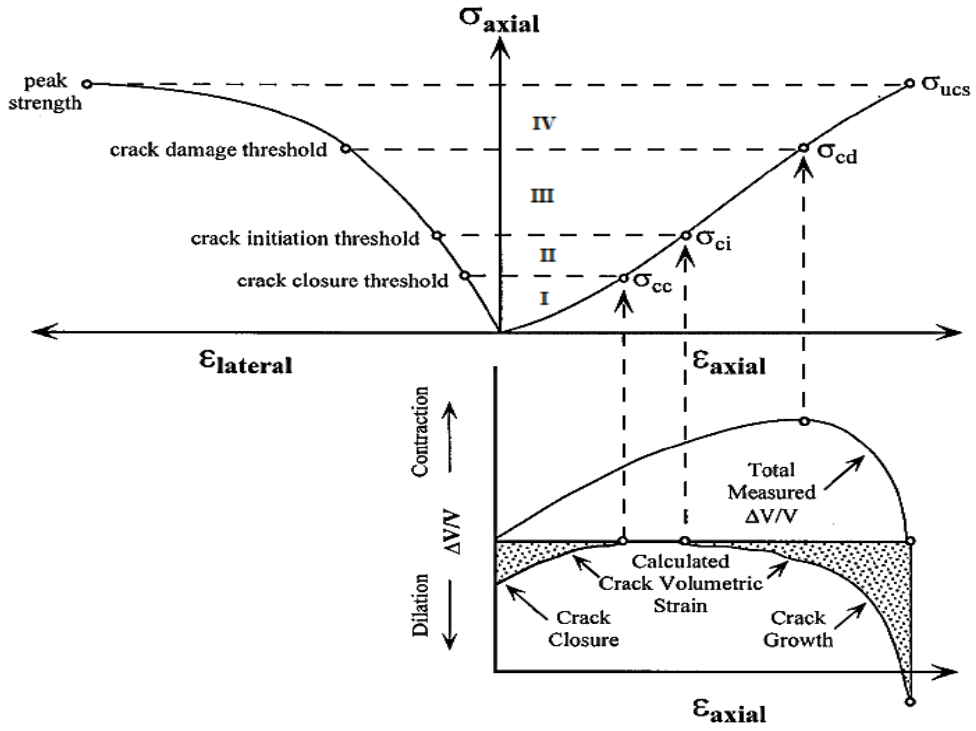


Figure 2.37: Stress-strain diagram showing crack development (Eberhardt *et al*.,1998)

Figure 2.36 and 2.37 establish the four widely accepted stages of stress-strain behaviour of brittle rock in relation to dilation. The stages as seen in Figure 2.37 are; (I) upward concavity of the stress-strain curve, which is attributed to crack closure (OA), (II) nearly linear elastic stage, (III) development of microfacturing and diltancy associated with propagation of stable microcrack and (IV) growth of macroscopic fracture, which results from the development of unstable micro-cracking pattern. The figures also show that the volume increase starts at the stage close to the peak region of the curve, that is, point C in Figure 2.36 and stage III in Figure 2.37. These figures only show the stress-strain and volumetric strain curves up to failure, the post-peak stage of deformation is not included. In the current research, the dilation angles are calculated at the pre-peak, peak and the residual stages of deformation.

Other important points that have been established by previous researchers (Zhao and Cai, 2010a; Vermeer and de Borst, 1984; Yuan and Harrison, 2004) are:

(i) dilation decreases with increasing confinement (Zhao *et al*., 2010);

(ii) the onset of dilation is delayed with increasing confining stress (Yuan and Harrison, 2004);

(iii) the rate of dilation, defined as the tangent slope of a point in the volumetric strain - axial strain curve, decreases when rock undergoes transition from strength weakening to residual strength; (Cai and Zhao, 2010)

(iv) dilation gradually reduces to a constant value at the end of the deformation stage, due to no additional volumetric strain (Cai and Zhao, 2010).

Hoek and Brown (1997) suggested the use of constant dilation angles based on rock mass quality. They recommended that the dilation angle is about ¼ of the friction angle for very good rock, 1/8 for average rock, and negligible for poor rock. Ord (1991) determined the values of cohesion, angle of friction and dilation angle of Carrara marble and Gosford sandstone. He reported dilation angle of 12° to 15° at 100 MPa confining pressure for Carrara marble, which is slightly higher than Gosford sandstone.

However, at higher confining pressures (400 MPa to 800 MPa), the reverse occurred, Gosdord sandstone is more dilatant, while Carrara marble is contractant. He also pointed out that in most cases, dilation angle is less than the friction angle, however, some of his results showed cases where the dilation angle is higher than the friction angle. For example, for Carrara marble, he stated that at first yield, that is, before cohesion loss, at 50 MPa confining pressure (friction angle = 20°, cohesion = 40 MPa, ψ = 16°), while at 100 MPa confining pressure, first yield (friction angle = 8°, cohesion = 58.5 MPa, ψ = 15°).

Figure 2.38 shows that the peak dilation angles of Witwatersrand quartzite, which is a brittle hard rock, are approximately 72°, 64°, 60°, 54°, 47° and 42° at confining stresses of 0.34, 3.45, 6.90, 13.79, 31.03 and 34.48 MPa respectively. The dilation angle also decreases with increasing strain. For instance, dilation angle at 0.1% strain for 0.34 confining pressure is 72°; it decreases to 39° at 4% strain.

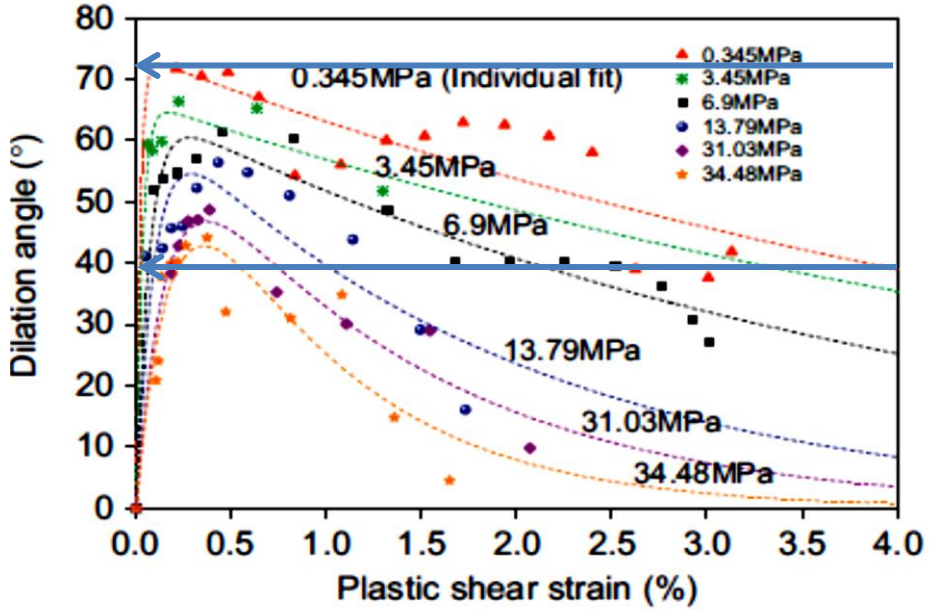


Figure 2.38: Dilation angle-plastic shear strain relationship for Witwatersrand quartzite under different confining stresses (Zhao and Cai, 2010a)

Table 2.7 presents the dilation angle of some common rocks.

Table 2.7: Summary of peak dilation angles for some rock types

Rock	ψ (°)	Confinement (MPa)	Reference
Carrara marble	15	100	Ord (1991)
Witwatersrand quartzite	72	0.34	Zhao and Cai, (2010a)
Limestone	24	2.5	Ribacchi (2000)
Brenna sandstone	33	0	Kwaśniewski and Rodríguez-Oitabén (2012)

In deep underground mines located in areas with high geothermal gradients, in thermal repositories, and in earthquake prone zones, increase in temperature may have effect on the dilation of the rocks. Little attention has been given to the effect of temperature on the dilatancy of rocks. This research will, therefore, investigate the effect of temperature on the dilation of rocks.

2.8 Measurement of P- and S-wave velocities

Utrasonic measurement, which is a non-destructive method, has been used for various studies such as, determination of rock dynamic elastic constants (Soroush and Qutob, 2011), degree of rock weathering (Kahraman *et al*, 2007), blasting efficiencies in rock mass (Young *et al*. 1985) and rock mass characterization (Bery and Saad, 2012; Klose *et al*, 2007). Sound velocities of rocks are influenced by factors such as rock type, elastic properties, texture, density, porosity, anisotropy, confining pressure, grain size and shape, water contentt, temperature, weathering, alteration zones, microcracks, bedding planes, and joint properties (roughness, filling materials, water, dip and strike (Altindag, 2012; Kahraman *et al*, 2007).

The longitudinal/compressional (P-wave) and transverse/shear (S-wave) velocities are calculated from the transition time of a travelling elastic pulse measured along the

axis of a cylindrical core specimen with parallel end faces. Aydin (2014) classified the techniques of generating sound waves and detecting their propagation through solids into two. The first technique involves the use of a single transducer, which he called pulse-echo technique, while the second technique, called pitch-catch technique, uses a pair of transducers (transmitter and receiver). In this research, the pitch-catch technique was used in examining the influence of temperature on P- and S-wave velocities of BIC rocks.

A typical layout of important ultrasonic testing components is shown in Figure 2.39 The components include a signal generator, an oscilloscope for visual analyses of the waveform, amplifier for signal enhancement, a data acquisition unit and two transducers (Aydin, 2014; ISRM, 2014).

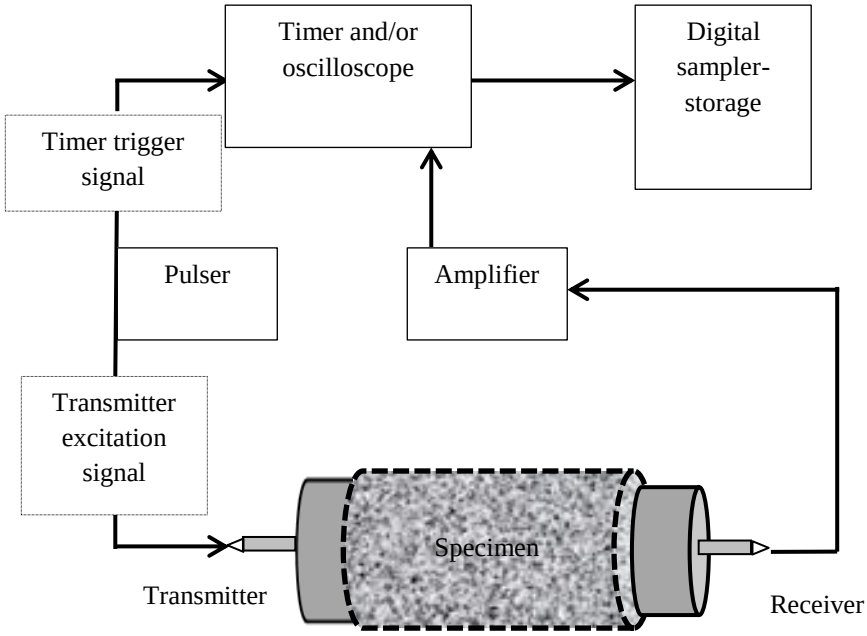


Figure 2.39: Layout of essential components of an ultrasonic apparatus (adapted from Aydin, 2014)

In order to achieve good test results, ISRM (2014) suggested the following:

- The test specimen's surface should be smooth, flat, parallel and should be measured at several points with a precision of ±0.01 mm.
- A thin layer of coupling material, such as Vaseline, oil, should be used to ensure efficient and uniform energy transfer from/to transducers.
- Transducers should be positioned and aligned to produce an acoustic axis (center beam), that is, normal to both faces.
- When the transducers are manually coupled, the travel times should be measured at least three times applying different pressures.

The P- wave velocity (V_p) and S-wave velocity (V_s) are determined from (ISRM, 2014)

$$V_p = L/t_p \quad (2.18)$$

and

$$V_s = L/t_s \quad (2.19)$$

Where L is the travel path length, t_p, and t_s are travel times for P- and S-waves, respectively.

Setyowiyoto and Samsuri (2009) demonstrated that increasing temperature caused reduction in the values of both P and S velocities. They reported that the P and S velocities of carbonate rock decreased from 3910 m/s to 3480 m/s and from 1965 m/s to 1780 m/s respectively when temperature increased from 28.47° to 57.10°C. Figure 2.40 shows the elastic wave velocities (V_p and V_s) as a function of temperature for three pore fluid conditions (without pore fluid, with Argon gas-filled, and with water-

filled). In all of the three conditions, the elastic wave velocities decreased linearly with increasing temperature.

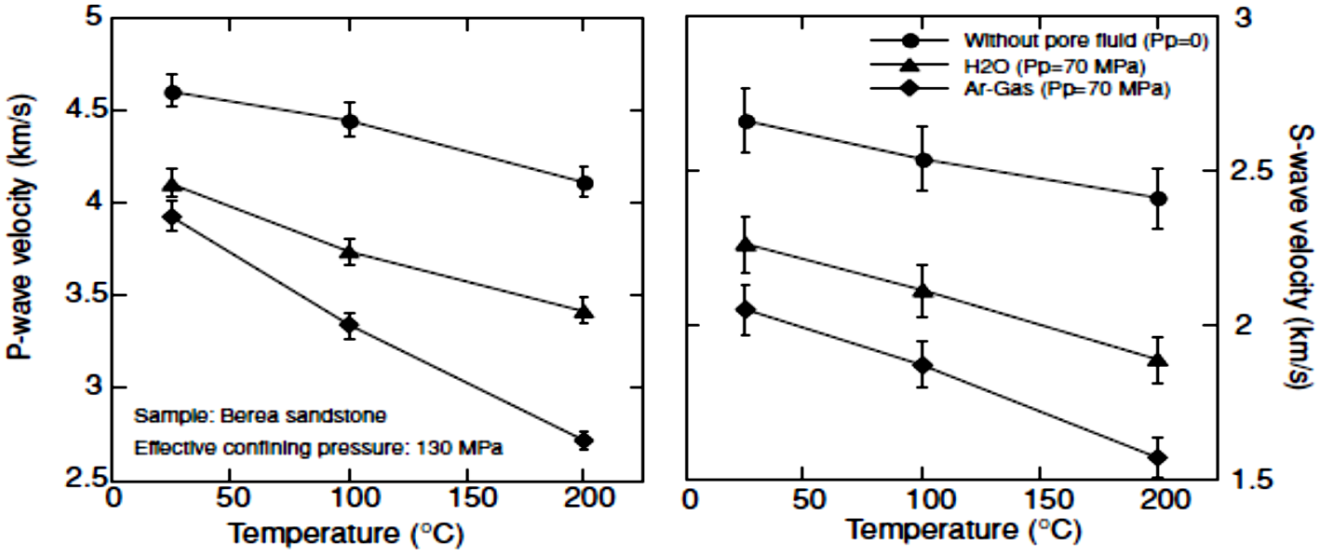


Figure 2.40: Influence of temperature on P- and S-wave velocities (Kitamura *et al*, 2006)

Confining pressure generally increases the wave velocities (Figure 2.41). He and Schmitt (2006) plotted the experimentally measured and Gassmann's equation calculated P- and S-wave velocities on a dry and water saturated sample. They explained that microcracks are not only playing an important role in controlling the pressure dependence of velocity, they also have a large effect on fluid substitution. Setyowiyoto and Samsuri (2009) also explained that increase in pressure causes compaction, porosity reduction and increase in ultrasonic wave velocities.

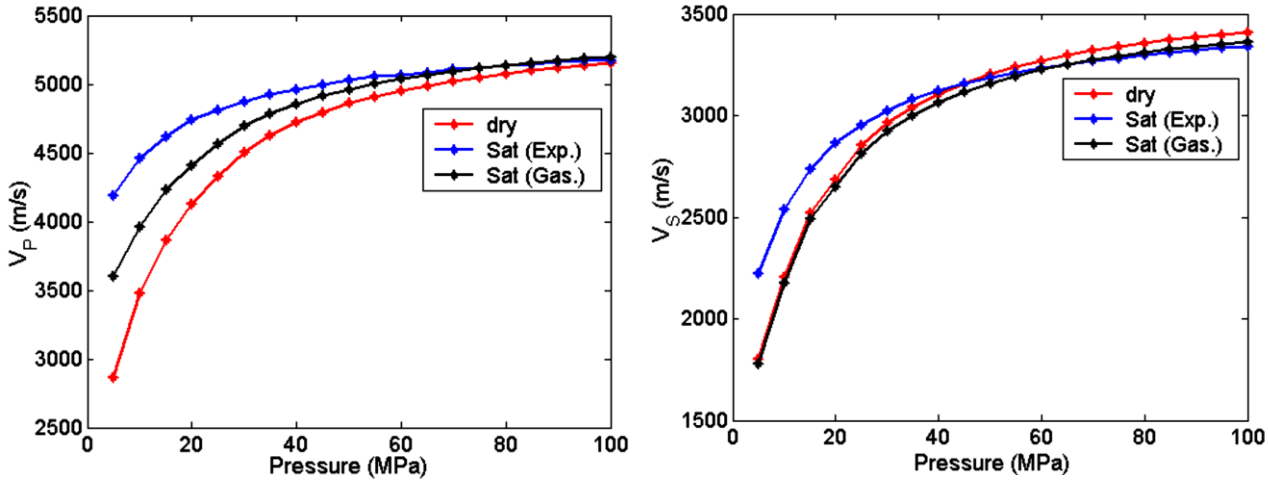


Figure 2.41: Influence of confining pressure on P- and S-wave velocities (He and Schmitt, 2006)

Figure 2.42 shows that velocity is strongly dependent on rock porosity. Setyowiyoto and Samsuri (2009) reported an inverse trend in the relationship between velocity and porosity. For example, when the porosity of some carbonate rocks increased from 5% to 20% acoustic velocity decreased from 4500 m/s to 2000 m/s.

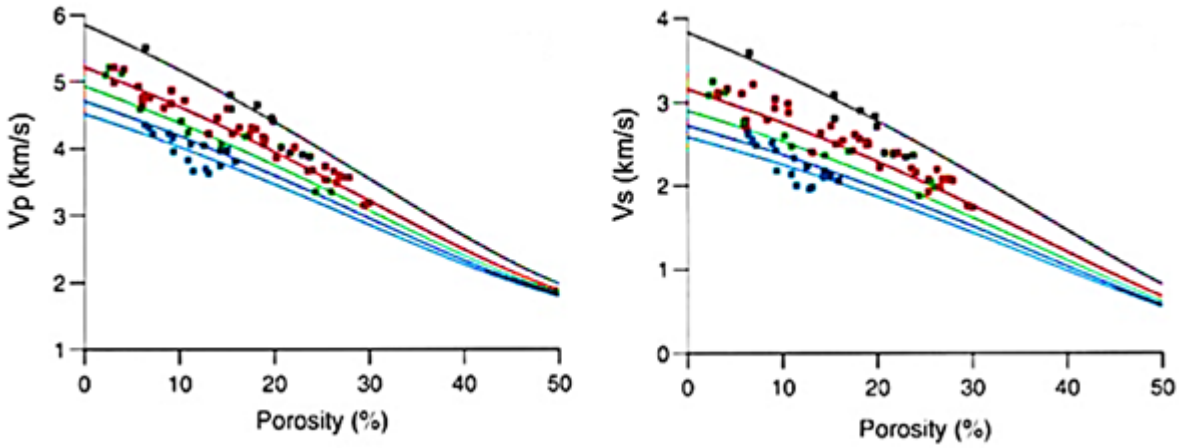


Figure 2.42: Influence of porosity on P- and S-wave velocities (Paoletti, 2012))

Fortin *et al* (2011) measured the axial and radial seismic velocities in a triaxial experiment on Etna basalt at confining pressure of 20 MPa. The plots of deviatoric

stress versus axial strain and P- and S-wave velocities versus axial strain are provided in Figure 2.43. As Figure 2.43 shows, V_p-axial are higher than V_p-radial. V_p-radial as well as V_s-horizontal decrease with increasing axial loading. These observations were attributed to crack initiation and propagation.

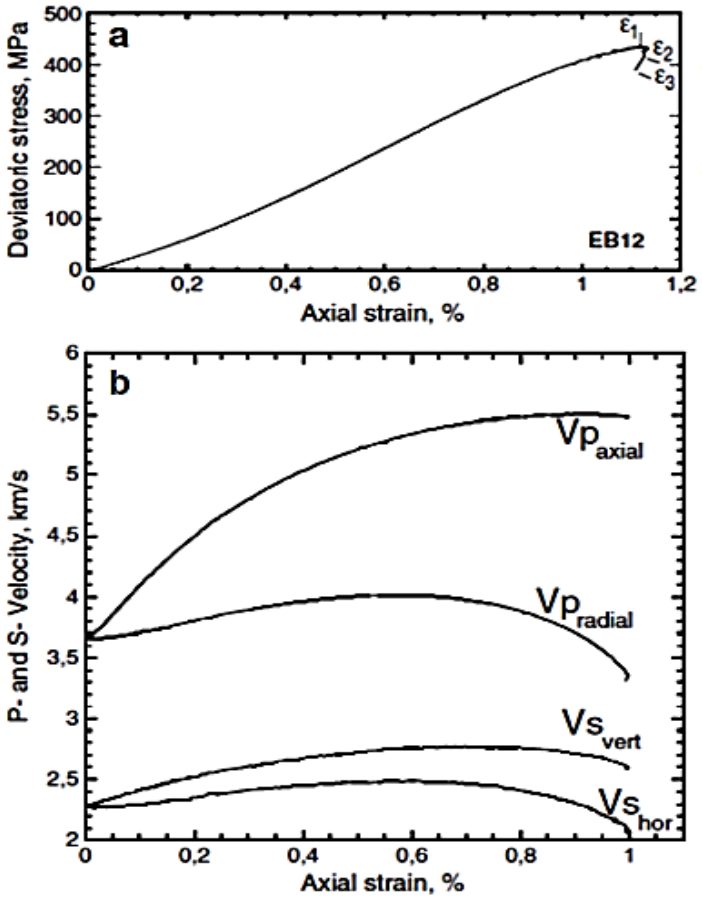


Figure 2.43: (a) Deviatoric stress versus axial strain (b) P- and S-wave velocities versus axial strain for Etna basalt. (Fortin *et al*, 2011)

2.9 Prediction of depth of brittle failure

The determination of the depth or lateral extent of failure is important for support design purposes. The type of failure that is typical in brittle rock is spalling or slabbing, which can lead to the formation of breakouts (Zhao and Cai, 2010b). Brady and Brown (2004) explained that the rock mass and stress field around an orebody can be described as near-field or far-field. They defined near-field as the rock mass and stress field within a distance of $3d_m$ from the excavation boundaries, where d_m is the minimum dimension of excavation created in the orebody. Far-field effects are those outside the range of near-field. Eberhardt *et al* (1998) noted that an underground opening in a stressed rock mass results in the deformation of the near-field rock due to a redistribution of stresses, resulting in stress concentrations. This stress redistribution increases strain energy in zones of high stress concentration. If the resulting imbalance in the energy of the system is severe enough, it can result in the progressive degradation of rock mass strength through fracturing.

Ortlepp *et al* (1972) studied the influence of the far-field maximum stress (σ_1) on failure of tunnels in South African mines. He concluded that for a stress environment where the ratio of the minimum to maximum far-field stress is equal to 0.5, minor spalling will occur if $\sigma_1 / \sigma_c > 0.2$, where σ_c is the laboratory uniaxial compressive strength. Martin *et al* (1999) illustrated tunnel instability and brittle failure as a function of Rock Mass Rating (RMR) and the ratio of the maximum far-field stress to the uniaxial compressive strength as shown in Figure 2.44. The part of the figure with red mark indicates the one applicable to the study area, BIC, since the rock mass is massive as reported in Chapter 5 of this thesis.

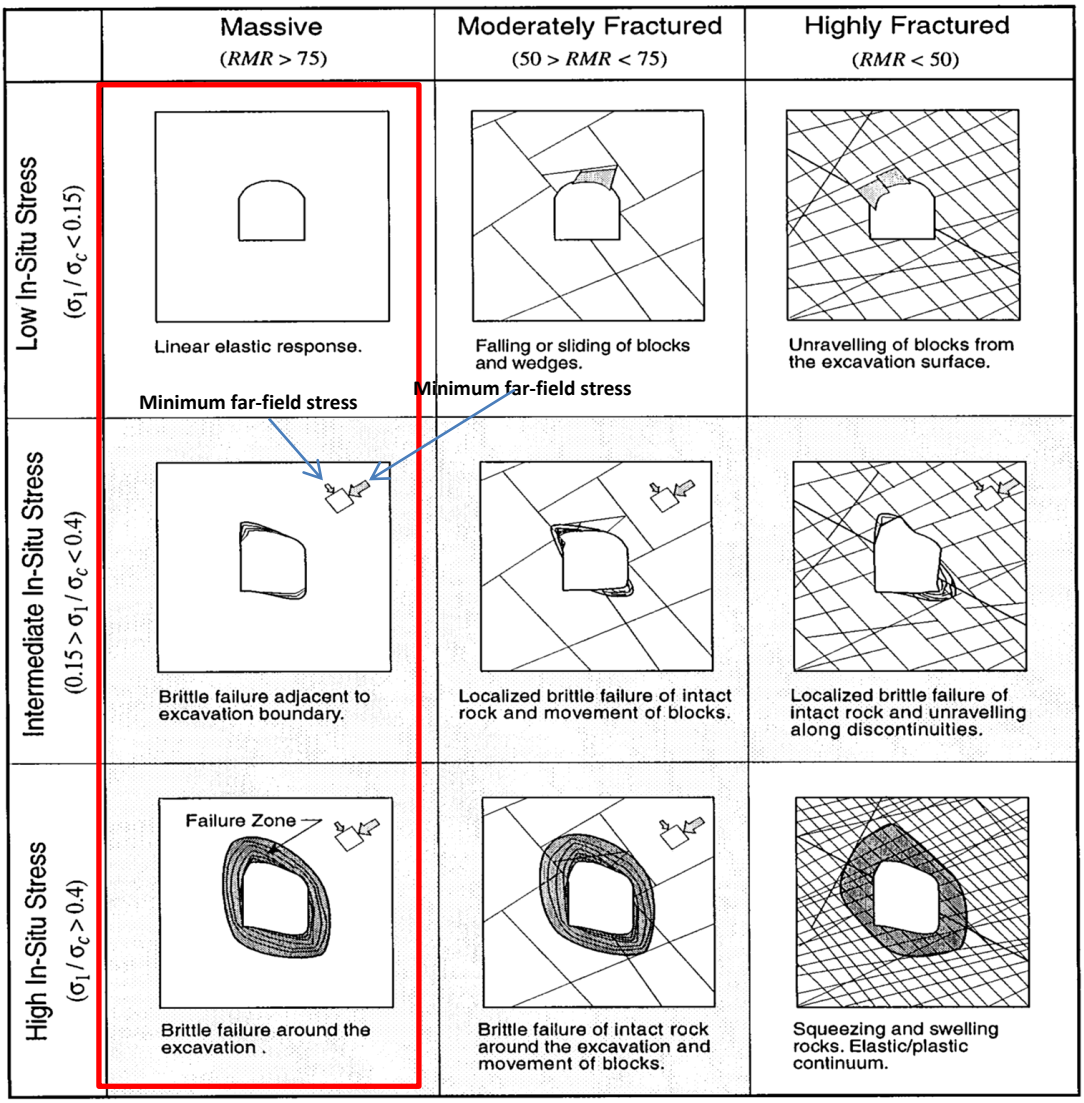


Figure 2.44: Tunnel failure modes (Martin *et al*, 1999)

Wiseman (1979) stated that stress-induced failure process initiates at the stress concentration near the boundary tunnels. He proposed a sidewall stress concentration factor (SCF) given by

$$SCF = \frac{3\sigma_1 - \sigma_3}{\sigma_c} \qquad (2.20)$$

Where σ_1 and σ_3 are the far-field in-situ stress and σ_c is the laboratory uniaxial compressive strength. Wiseman (1979) noted that the conditions for unsupported tunnels worsened rapidly when SCF reached a value of about 0.8.

In a bid to predict the depth of failure around tunnels in massive quartzite, Stacey (1981) proposed that depth of failure could be estimated from calculation of extension 'ϵ' strain given by

$$\epsilon = \frac{1}{E}\left[\sigma_3 - \nu(\sigma_1 + \sigma_2)\right] \quad (2.21)$$

Stacey (1981) stated that if the calculated extension strain is greater than the critical extension strain, spalling would occur.

Martin *et al* (1999) explained that the brittle failure process is controlled by the cohesion of the rock mass, based on observational evidence and prediction of spalling from the concept of extension strain criterion. They examined different case studies where the generalized Hoek-Brown failure criterion given in equation 2.22, has been used for the estimation of the depth of failure. Martin *et al* (1999) concluded that elastic analyses combined with the appropriate Hoek-Brown brittle parameters are adequate, for practical purposes, in estimating the depth and extent of stressed-induced failure zones in massive rock mass.

$$\sigma_1 = \sigma_3 + \sigma_c \left(m \frac{\sigma_3}{\sigma_c} + s\right)^a \quad (2.22)$$

The empirical constants m and s are based on the rock mass quality. For most hard rock masses, the constant 'a' is equal to 0.5, which makes equation 2.22

$$\sigma_1 = \sigma_3 + \sqrt{m\sigma_c\sigma_3 + s{\sigma_c}^2} \quad (2.23)$$

Martin *et al* (1999) proposed setting m to zero to reflect non-mobilization of frictional strength, thus reducing equation 2.22 to

$$\sigma_1 = \sigma_3 + \sqrt{s\sigma_c{}^2} \quad (2.24)$$

and setting $\sqrt{s}$ to 1/3 gives

$$\frac{\sigma_1 - \sigma_3}{\sigma_c} = 0.33 \quad (2.25)$$

Equation 2.25 is the constant deviatoric stress equation proposed by Martin *et al* (1999) for depth of failure prediction in brittle rock mass.

If $\frac{\sigma_1 - \sigma_3}{\sigma_c} < 0.33$ it means that there is no failure.

2.10 Discussion

Table 2.8 summarises some of the factors that affect the strength of rocks. The significance of each of the factors is categorized as major, intermediate, and minor with a range of 100 to 60%, 59 to 30% and less than 30% respectively. As Table 2.8 shows, porosity, discontinuity and mineral contents have major significance on strength reduction, while moisture content has minor influence. The effect of loading rate, temperature, relative humidity, and confining pressure belongs to the intermediate category. Although, relative humidity is a measure of the amount of water content in the air, it also influences the behavior of rocks.

It should be noted, however, that the level of significance of the factor stated in Table 2.8 is not absolute; it may vary with different rock types.

Table 2.8: Summary of some of the factors influencing rock strength

S/N	Factors	% strength reduction	Reason	Rock type	Significance
1	Porosity	85	Porosity increases from approx. 22% to 50%	Sandy shale	Major
2	Moisture content	25	Increased level of saturation lowers strength	Sandstone	Minor
3	Loading rate	37	Strain rate decreases from 10^{-2}/sec to 10^{-5}/sec	Tuff	Intermediate
4	Discontinuity	81	Crack density increases from 0 to 100 m^2 /m^3	Marble	Major
5	Temperature	51	Temperature rises from 20°C to 250°C	Shale	Intermediate
6	Temperature	36	Temperature increases from 500°C to 950°C	Sandstone	Intermediate
7	Relative Humidity	32	Relative humidity increase from 0 to 80%	Sandstone	Intermediate
8	Confining Pressure	54	Confining pressure decreases from 130 MPa to 60 MPa	Sandstone	Intermediate
9	Confining Pressure	50	Confining pressure decreases from 40 MPa to 10 MPa	Anorthosite	Intermediate
10	mineral content	67	Muscovite content increases from 0 to 20%	Quartzite	Major

2.11 Chapter Summary

From the literature survey, it has been established that variation in temperature has influence on the behaviour of rocks. These effects have been studied for cases of underground fire accidents, thermal repositories, geothermal intrusions, underground storage caverns and thermal weathering. The question as to what will be the influence of virgin rock temperature on the stability of underground openings, particularly those located in areas of high geothermal gradient, such as Bushveld Igneous Complex, remains unanswered. Providing answer to this question is the major motive

behind this research. This chapter also provides a theoretical background to some of the laboratory testing (Chapter 3), microscopic analyses (Chapter 4) and numerical modelling (Chapter 5).

CHAPTER THREE

3.0 LABORATORY TESTS

This chapter presents the methodology, the equipment/materials for all the laboratory tests conducted in the course of the research, in addition to the results obtained. The laboratory tests were, on one hand, aimed at gaining insight into the effect of temperature variation on the behavior of the rocks from the Platinum mines. On the other hand, the results of the tests serve as input parameters into the numerical modelling presented in Chapter 4. As Hoek and Martin (2014) noted, the understanding of the characteristics of rock and rock masses, as engineering material, starts with the knowledge of the behaviour of intact rock. The tests include determination of the following properties on the rock samples from the BIC:

1. Indirect tensile strength through Brazilian test.
2. Mechanical properties (UCS, Young's modulus, Poisson's ratio) under ambient temperature and uniaxial loading using Amsler testing machine.
3. Coefficient of thermal expansion in an unconfined condition using oven and video extensometer.
4. Coefficient of thermal expansion in a confined condition using MTS servo-controlled testing machine.
5. Uniaxial and triaxial testing at various temperatures and confinements to obtain the peak strength and post-peak behaviour using MTS machine.

3.1 Rock samples and their sources

The rock samples tested were obtained from four different mines located in the northern and the western limb of the BIC. The mines and the samples obtained are summarized in Table 3.1.

Table 3.1: Details of the samples received from different mines

S/N	Mines	Company	BIC location	Rocks received	Diameter (mm)
1	Mogalakwena Platinum mine	AngloAmerican Platinum	Northern limb	GN, VTA, MA, G, GF, PX	36
2	Bafokeng Rasimone Platinum	Royal Bafokeng Platinum (BRPM)	Western limb	N, LN, ANCR, VTA, MA, CR, PX	36
3	Khomanani Platinum mine	AngloAmerican Platinum	Western limb	GN, N, LN, VTA, MA, PX	47*
4	Siphumelele Platinum mine	AngloAmerican Platinum	Western limb	N, LN, MA, PX	32

* N:B- The diameter of the Khomanani samples were reduced to 42 mm in the laboratory before testing.

ANCR : anorthosite-chromitite; CR : chromitite; LN : leuco-norite; MA : mottled-anorthosite; N : norite; PX : pyroxenite; VTA : varitextured-anorthosite; GN : gabbro-norite; G : granite; GF :granofels.

The borehole depth below surface for the samples from BRPM, Mogalakwena mine and Khomanani mine are provided in Table 3.2.

Table 3.2: Borehole depth of rock samples

	Borehole ID	From (m)	To (m)
BRPM samples			
N	N/A	861.18	1092.59
LN	N/A	872.51	1214.78
ANCR	N/A	942.25	1293.79
VTA	N/A	835.00	1163.66
MA	N/A	868.03	1228.48
CR	N/A	957.52	1291.29
PX	N/A	863.06	1225.68
Mogalakwena mine samples			
GN	OY676	15.85	21.69
VTA	OY676	117.10	661.40
MA	OY676	49.82	224.77
G	OY748D0	497.23	507.20
GF	OY750	492.05	493.43
PX	VK99	681.70	688.70
Khomanani mine			
GN	N/A	709.21	719.50
N	N/A	688.32	695.65
LN	N/A	600.11	624.88
VTA	N/A	683.12	687.43
MA	N/A	624.52	672.41
PX	N/A	697.66	704.07

3.1.1 Specimen preparation

The specimens were prepared according to ISRM standard (ISRM, 1983). The test specimens for uniaxial and triaxial testing were prepared with a height to diameter ratio of 2.5. The ends of the specimen were cut and ground parallel to each other, and at right angle to the longitudinal axis. The disparity between the perpendicular ends of the specimen to its longitudinal axis was not more than 0.05 in 50 mm (ISRM, 1983).

3.2 Brazilian (Indirect tensile) test

The test specimens were right circular cylinders with height to diameter ratio of approximately 0.5. The diameter of the specimens is 36 mm except for those from Khomanani mines, which is 42 mm. Specimens from Siphumelele were not tested due to their relatively smaller diameter, that is 32 mm. The cylindrical surfaces were free from boring associated marks. Irregularities across the thickness of the specimen were less than 0.025 mm. End faces were flat to within 0.25 mm and square and parallel to within 0.25°, as suggested by ISRM (1978). Some of the samples tested are shown in Figures 3.1 and 3.2.

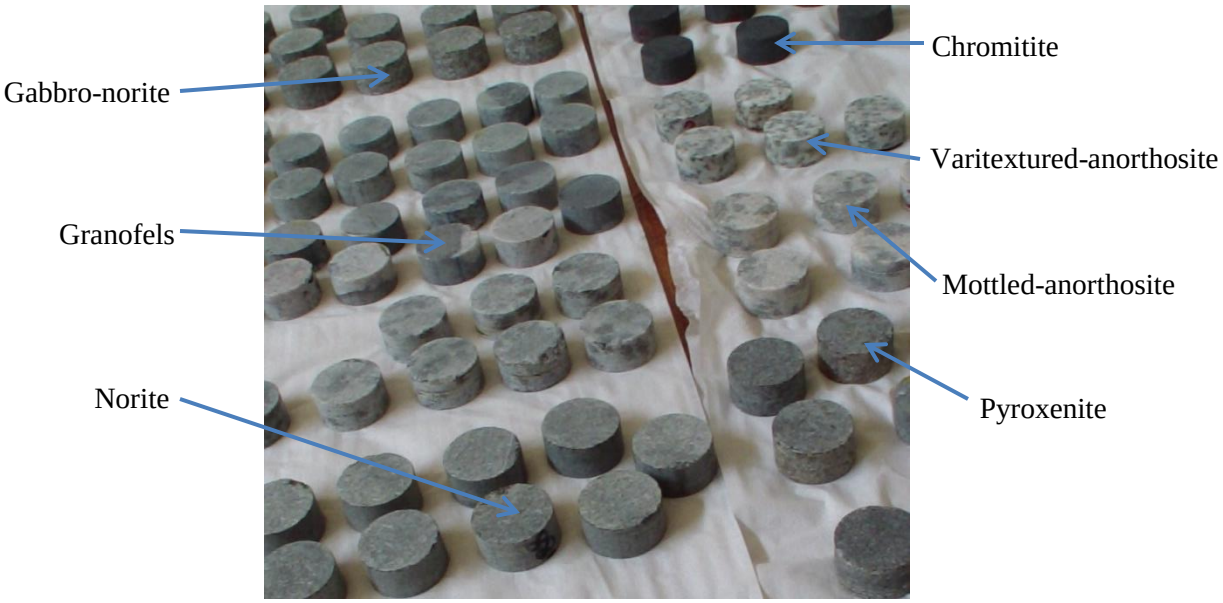


Figure 3.1: Brazilian test specimens before testing



Figure 3.2: Some Brazilian test specimens after testing

The diametric loading of the samples is performed with the MTS Criterion testing machine. The loading complied with ISRM requirement for indirect testing of tensile strength in that the specimens were continuously loaded at a constant rate of 200 N/s until failure. The detail description of the Brazilian test set-up is provided in section 2.4.1. Ten tests were done for each rock type. The specimens failed by splitting along diameter starting from the centre towards the loading point as shown in Figure 3.2. The average tensile strength (σ_{t_av}) and standard deviation of the rock types received from BRPM, Khomanani and Mogalakwena mines are provided in Table 3.3

Table 3.3: Average tensile strength and standard deviation of specimens.

Rock Types							
			BRPM				
	ANCR	CR	LN	MA	N	PX	VTA
σ_{t_av} (MPa)	**7.2**	**4.9**	**9.5**	**9.5**	**11.2**	**11.4**	**8.9**
s.d.	1.6	2.1	0.9	2.6	1.8	1.1	1.5
			Khomanani				
		GN	**LN**	**MA**	**N**	**PX**	**VTA**
σ_{t_av} (MPa)		10.0	7.7	11.1	13.6	10.5	8.6
s.d.		0.7	1.6	1.7	2.1	1.6	1.2
			Mogalakwena				
		G	**GN**	**MA**	**GF**	**PX**	**VTA**
σ_{t_av} (MPa)		11.7	13.6	13.8	13.5	20.0	12.0
s.d.		2.5	0.4	4.1	3.8	3.7	1.4

ANCR : anorthosite-chromitite; CR : chromitite; LN : leuco-norite; MA : mottled-anorthosite; N : norite; PX : pyroxenite; VTA : varitextured-anorthosite; GN : gabbro-norite; G : granite; GF :granofels.

3.3 Compressive strength testing using Amsler testing machine

The uniaxial and triaxial compressive strength of the rock samples were determined under ambient temperature (approximately 20°C) using Amsler compression testing machine, shown in Figure 3.4. The machine is hydraulic, soft type with a load capacity of 2000 kN. Testing is done manually at a constant rate by controlling force-controlled, which results in violent uncontrolled failure at the peak force. The loading rate is manually controlled. The hydraulic piston, which applies force on test specimens, is located at the base of the load frame. The Amsler machine has been installed in 1974 and it is still in a good working condition.

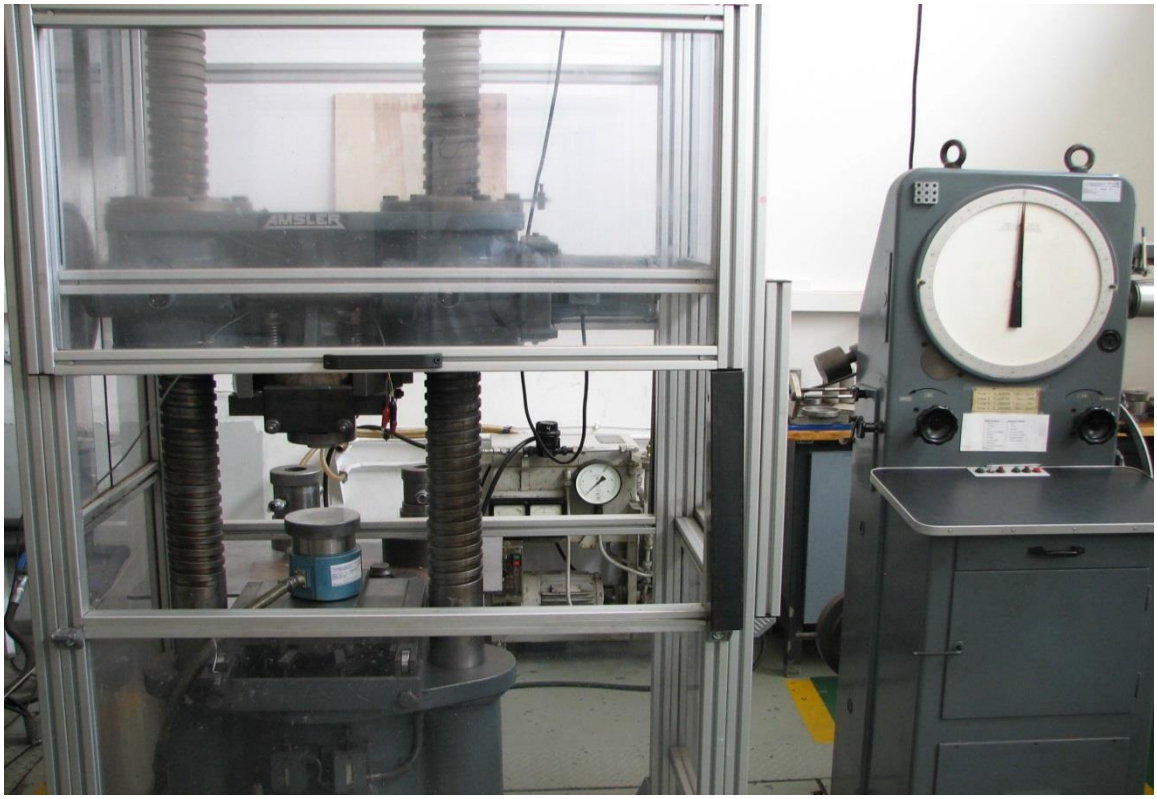


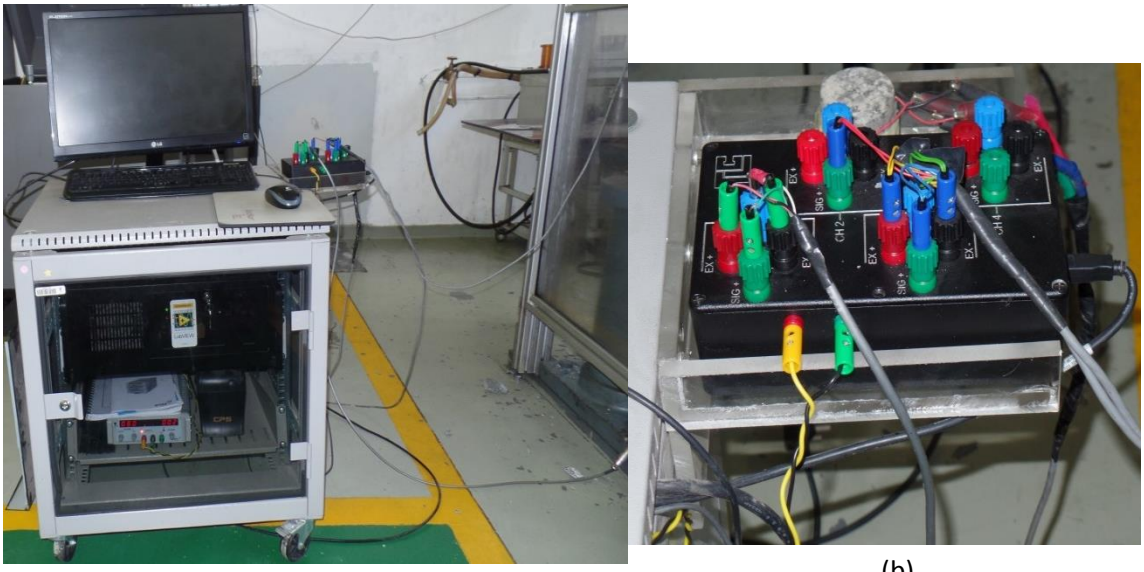
Figure 3.4: Amsler compression testing machine

3.3.1 Test specimens

UCS tests were conducted on Siphumelele and Mogalakwena specimens, while UCS with Modulus (UCM) tests were done on BRPM and Khomanani specimens. Four strain gauges were glued on the cylindrical specimens, two axially and two transversely, for the measurement of axial and lateral strains respectively while the specimen is loaded. The electrical resistance of a strain gauge varies in proportion to the amount of strain. Lead-wires connected to the strain gauges (Figure 3.5) transfer signals to strain guage amplifier and then to the computer, where the experimental data are stored with "Lab-VIEW precision data acquisition and control version 8 program" (Figure 3.6).



Figure 3.5: Specimens with strain gauges and lead-wires



(a) (b)

Figure 3.6: Data acquisition system (a) data acquisition and control unit (b) strain gauge amplifier

3.3.2 Test procedure for uniaxial compression test

The specimen is placed in between the lower platen and the spherical seating on the top. The lead-wires were connected to the bridge box and data logger. The specimen is then compressed at a constant loading rate of 0.5 kN/sec. such that failure occurs within 5-10 minutes of loading as recommended by ISRM (1979). The load is measured by the load cell at the base of the lower platen.

The result of testing allowed the calculation of UCS Young's modulus and Poisson's ratio. The aim of performing UCS and determination of elastic properties of different rock types in ambient condition is for comparison to the tests done under various temperatures. The test results also serve as input parameters into the numerical modelling aspect of the research.

Figures 3.7 and 3.8 show some of the stress versus strain graphs for the tested specimens under uniaxial compression.

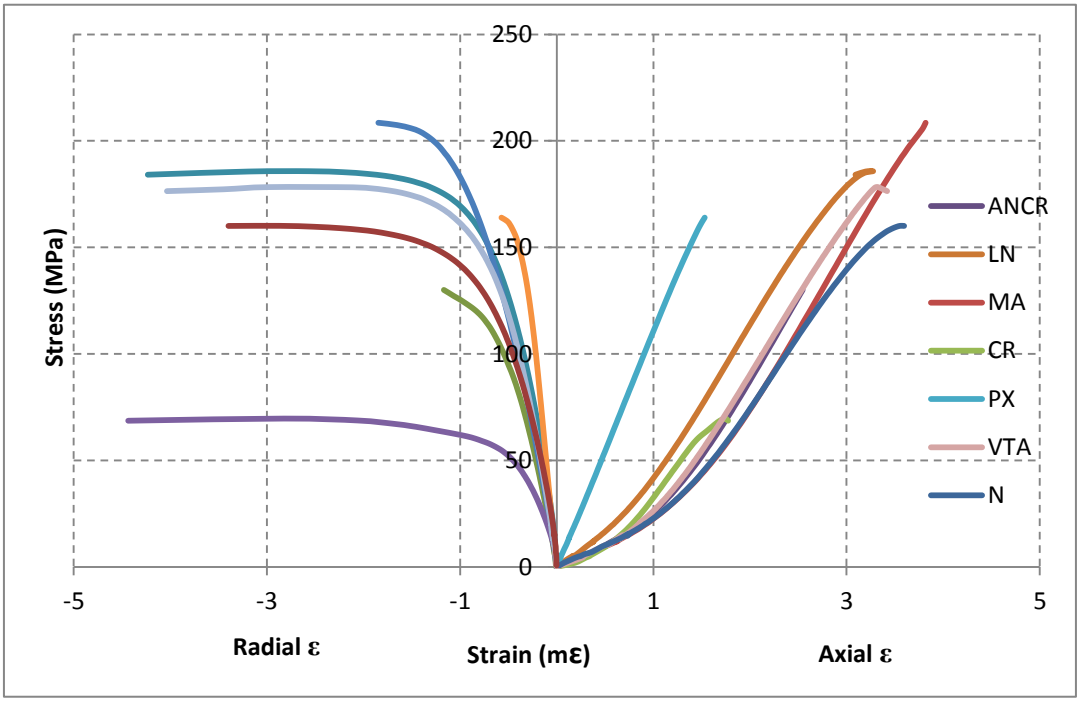


Figure 3.9: Stress-strain for BRPM specimens

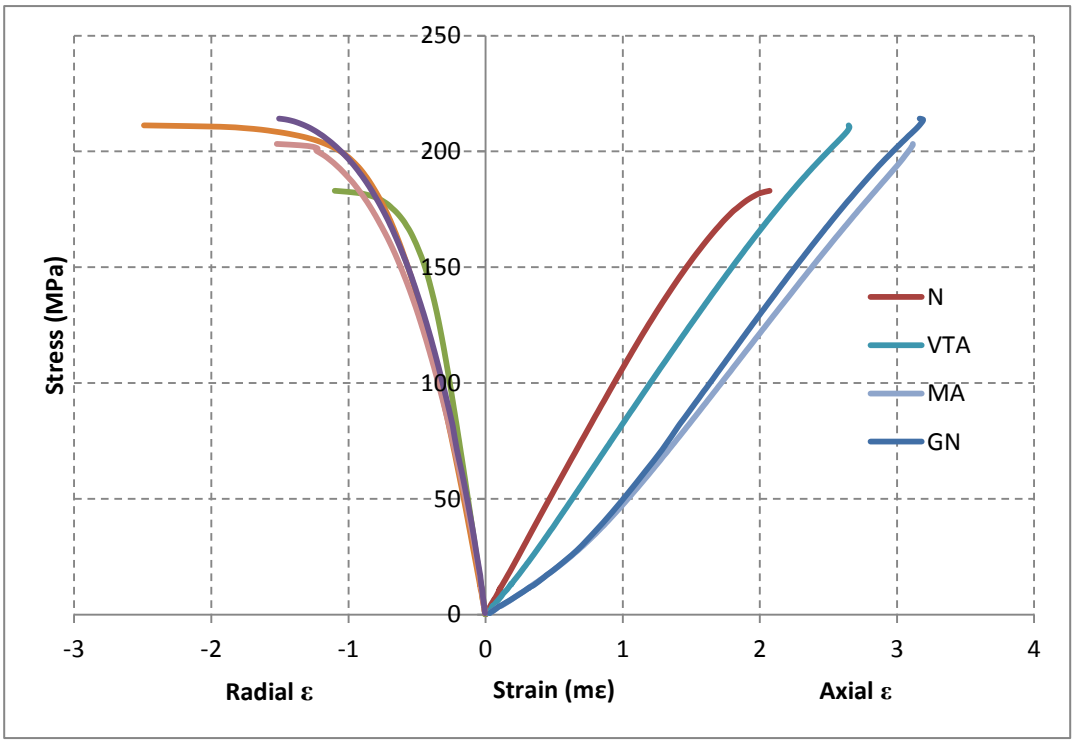


Figure 3.10: Stress-strain plot for Khomanani specimens

Table 3.4 shows the UCS of the rocks, while the bulk modulus, shear modulus, tensile strength and density of the rocks are given in Table 3.5.

Table 3.4: UCS of specimens from Khomanani, Siphumelele, Mogalakwena and BRPM in MPa.

Mines	**Specimen**	**Rock types**								
		MA	PX	VTA	N	LN	CR	ANCR	GF	G
Khomanani	1	264	126	314	179					
	2	287	102	238	189					
	3	285	121	276	221					
	4	280	115	325	185					
	5	276	118	247	213					
	Average	**278**	**116**	**280**	**197**					
Siphumelele	1	126	65		55	148				
	2	115	85		73	130				
	3	100	115		75	132				
	4	95	83		80	136				
	5	159	95		90	138				
	Average	**119**	**89**		**75**	**137**				
Mogalakwena	1	292	334	231					274	153
	2	271	361	205					251	205
	3	256	335	234					227	176
	4	336	360	221					266	145
	5	210	327	224					235	180
	Average	**273**	**343**	**223**					**251**	**172**
BRPM	1	201	163	180	151	175	63	150		
	2	208	164	178	155	172	71	130		
	3	208	165	185	160	186	70	135		
	4	204	157	185	143	172	66	125		
	5	193	161	184	159	170	65	133		
	Average	**203**	**162**	**182**	**154**	**175**	**67**	**135**		

Looking through Table 3.4, the following observation is worthy of note:

The UCS of Simphumelele specimens were far less than those from other mines for the same rock types. For example, the average UCS of MA, PX are 119, 89 for Simphumelele and 203, 162 for BRPM specimens. This may be attributed to textural or compositional influence, the detail of which is beyond the scope of this thesis. The table also revealed that for specimens of the same rock type and size, there is variability in their UCS. For instance, the average UCS of MA, PX, VTA are 273, 343, 223 and 203, 162, 182 for Mogalakwena and BRPM specimens respectively. Obviously, the Mogalakwena specimens are of higher strength than those of the BRPM.

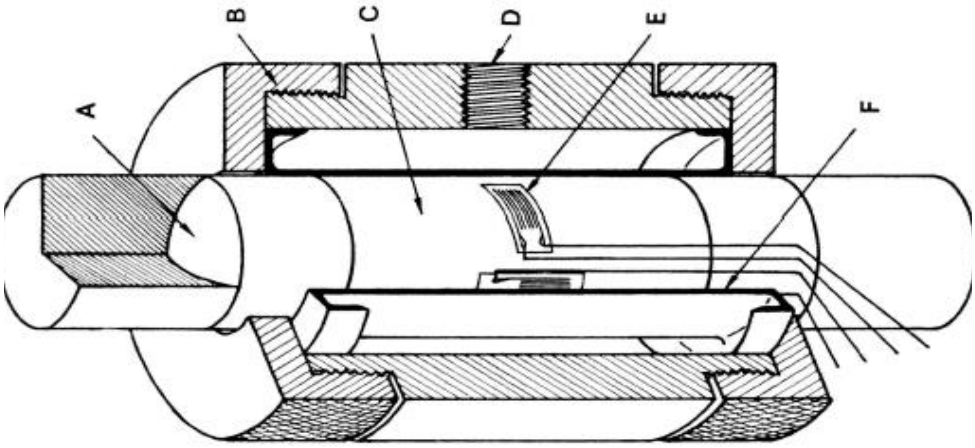
Table 3.5: Strength and physical properties of rocks from BRPM

	ANCR	**CR**	**LN**	**MA**	**N**	**PX**	**VTA**
Bulk Modulus (GPa)	108.6	128.7	73.4	94.1	65.6	71.9	94.5
Shear Modulus (GPa)	23.3	17.3	28.4	27.8	23.9	44.6	26.9
Young's Modulus (GPa)	65.2	49.7	75.4	75.9	63.8	110.9	73.7
Poisson's Ratio	0.40	0.44	0.33	0.37	0.34	0.24	0.37
Tensile Strength (MPa)	7.2	4.9	9.5	9.5	11.2	11.4	8.9
UCS (MPa)	135	67	175	203	154	162	182
Density (kg/m^3)	2853.1	4050.0	2776.4	2744.8	3045.4	3194.0	2766.5

3.3.3 Triaxial compression strength testing

Only the specimens from BRPM were tested in triaxial compression. Specimen preparation is similar to uniaxial testing, including the length to diameter ratio. Strain gauges were also attached to the specimen for the determination of axial and lateral strains while loading took place by Amsler testing machine.

The confining pressure was applied to the specimen with the aid of a hydraulic pump. The triaxial cell used is Hoek cell (Figure 3.14) that consists of the cell body, spherical seatings and a flexible membrane which prevents the confining fluid from entering the specimen. The specimens were tested at three confinements, which are, 5 MPa, 10 MPa and 15 MPa. The aim of the triaxial testing is to determine the Mohr-Coulomb parameters of the rocks, that is, cohesion, angle of internal friction and bulk shear modulus at ambient temperature. These parameters are used as input parameters in numerical (Chapter 5) to assess rock failure.



A – Spherical seat, B – Mild steel cell body, C – Rock specimen, D – Oil inlet, E – Strain gauges, F – Sealing membrane

Figure 3.14: Triaxial cell (After, Franklin and Hoek, 1970)

After the specimen is placed in the cell, the lead-wires from the strain gauges were connected to the bridge box for recording the strain data. The axial load and the confining pressure were increased simultaneously up to 5 MPa, 10 MPa and 15 MPa for each test individually. Thereafter, the axial loading continued until failure occurred. The specimen was loaded at a constant rate of approximately 0.5 kN/sec, such that failure occurred within 5-10 minutes of loading. The values of the axial load and strains were recorded throughout the test.

Tangent Young's modulus, Et, and Poisson's were measured at a stress level equal to 50% of the uniaxial compressive strength. The compressive strength is the peak stress sustained by the specimen. The Young's modulus and Poisson's ratio for the triaxial tests are provided in Appendix A3. The peak stresses were plotted against their corresponding confining pressures. The tangent of the slope, m, of a straight line drawn across the points (Figure 3.15) is used in the calculation of the internal friction angle, Ø, and the cohesion, c of the intact rock, as in the equations 3.2 and 3.3 shown below. The position of the straight line is fixed by the ordinate, σ_c that stands for the UCS.

Friction Angle, $$\emptyset = \sin^{-1}\left(\frac{m-1}{m+1}\right) \quad (3.2)$$

and

Cohesion, $$C = \left(\frac{1-Sin\emptyset}{2Cos\emptyset}\right)\sigma_c \quad (3.3)$$

The plot of peak stress versus confining pressure, showing the gradient "m" (strengthening parameter), is given in Figure 3.15, while Table 3.6 summarises the calculated internal angle of friction and cohesion for BRPM specimens.

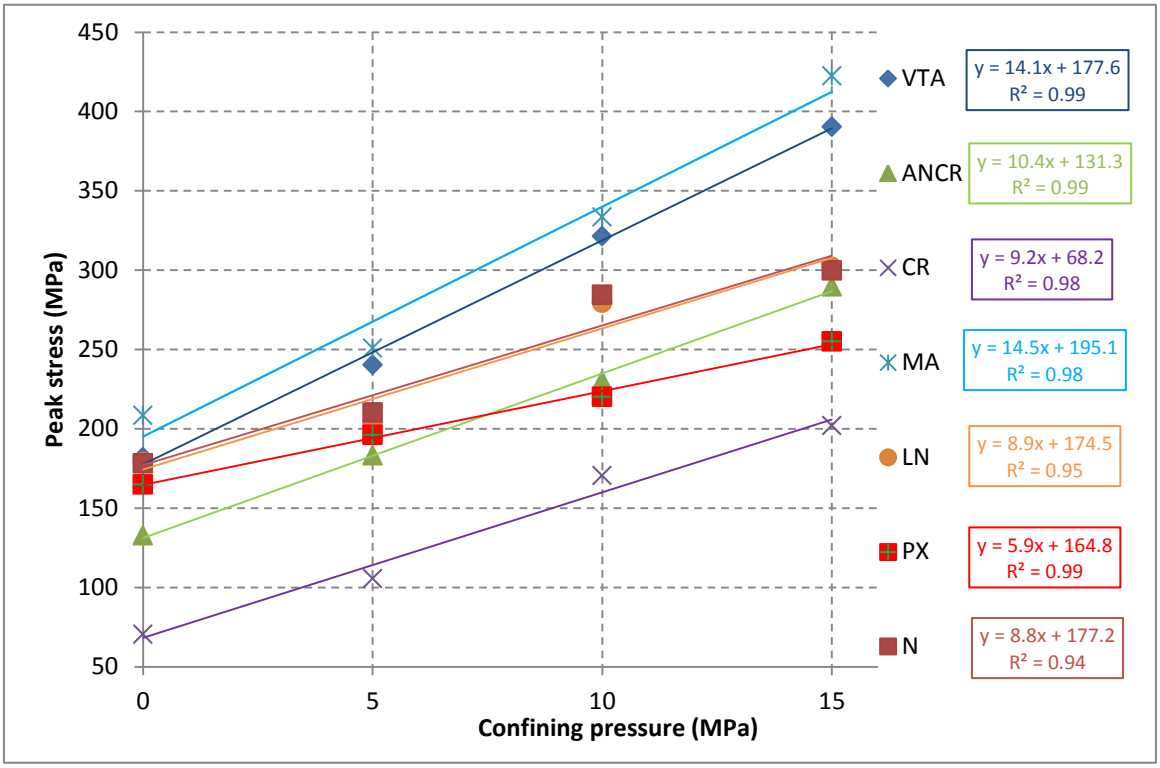


Figure 3.15: Plot of peak stresses versus confining pressures

Table 3.6: Values of m, angle of internal friction and cohesion for BRPM specimens

Parameters	ANCR	CR	LN	MA	N	PX	VTA
m	10.36	9.18	8.88	14.49	8.79	5.90	14.12
Ø (°)	55.27	53.13	52.09	59.43	52.75	45.24	59.77
C (MPa)	32.77	20.69	41.59	51.43	36.40	35.21	44.62

3.3.4 Compression testing using MTS servo-controlled testing machine

The uniaxial and triaxial compression testing of the specimens at varied temperatures were carried out using MTS 815 servo-controlled testing machine (Figure 2.28). The equipment is a stiff testing machine. The tests are aimed at simulating the real life loading condition and environment expected in the platinum mines, where the virgin

rock temperature increases with increasing depth. The tests would assist in the determination of the post-peak behaviour of BIC rocks. This information is crucial in understanding the process of specimen deformation, right from the stage of crack initiation, in the pre-peak failure phase to complete failure, after post failure stage. The information gained would provide insight into the residual strength and post failure behaviour of BIC rock types.

3.3.4.1 Test procedure

The triaxial tests were designed to achieve the following:

a. Study the response of specimens to variation in temperature under triaxial loading. This was achieved by testing all the available samples, from BRPM, at the same confining pressure (10 MPa) and different temperatures, that is, ambient temperature (approximately 20°C), 50°C, 70°C, 90°C, 110°C and 140°C.
b. The selected specimens (norite, mottled anorthosite, pyroxenite and chromitite) are mainly the immediate hanging wall, foot wall rock types or reef in most of the platinum mines. The rock strengths at confining pressures of 10 MPa, 20 MPa, and 30 MPa at the temperatures mentioned in "a" were used for the evaluation of Ø and c.
c. Study the effect of temperature variation on the UCS of the specimens. This was attained by testing the specimens at 20°C, 50°C, 90°C, and 140°C.
d. Determine the linear coefficient of thermal expansion of the specimens under confinement. As stated in the literature review, linear coefficient of thermal expansion in terms of the change in length of rock, while volumetric coefficient of thermal expansion, considers the volume change. This was achieved by subjecting the specimens to a hydrostatic pressure of 3 MPa, after which they were heated at the rate of 2°C/minute until the desired temperature (50°C, 70°C, 90°C, 110°C and 140°C) is reached. When the targeted

temperature is reached, the temperature is kept constant for one hour to allow for even distribution of heat through the specimen.

3.3.4.2 Test specimens

Only specimens from BRPM were tested for the uniaxial and triaxial strengths using servo-controlled testing machine. The reasons for this are:

i. In the previous compression tests done with Amsler compression testing machine, it was observed that there were variation in the strength of the same rock type sourced from different mines.
ii. In terms of the quantity of the samples received from the mines, the ones from BRPM were the most and could cover all ranges of tests done on the servo-controlled testing machine.

Specimen preparation is the same as described under compression testing using Amsler machine. The only exception is that the specimen is jacketed in heat-shrink teflon material to prevent confining fluid from getting in touch with the rock surface during heating and loading, and during failure process.

3.3.4.3 Results of the linear coefficient of thermal expansion test

Figure 3.20 shows the plots of axial thermal strain measured in a confined condition (10 MPa confining pressure), using MTS machine, as a function of temperature for norite, while the plots for other rock types are given in appendix A2.

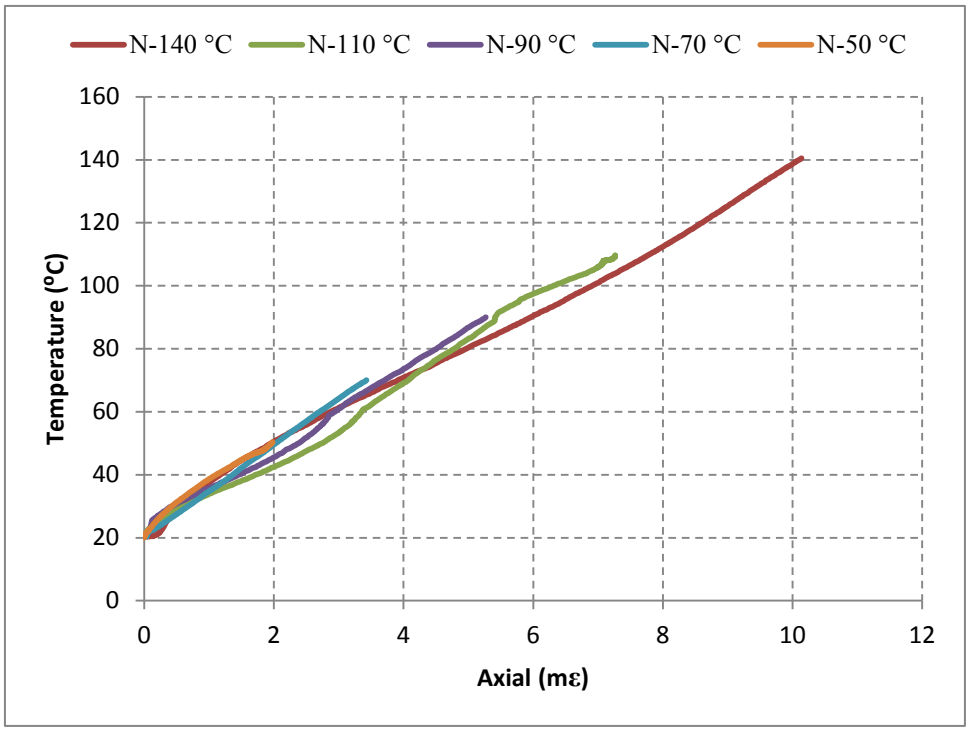


Figure 3.20: Plot of temperature versus axial stain for norite under 10 MPa confinement

Figure 3.20 shows a linear relationship between temperature and extension of the rock specimen. Five norite specimens were heated from ambient temperature (~20°C) to 50°C, 70°C, 90°C, 110°C and 140°C as seen in Figure 3.20. Both axial and radial expansions of the rocks were noticed with increasing temperature. Only the axial strain is presented in Figure 3.20 since it is the required parameter for the calculation of coefficient of linear thermal expansion (CLTE). The same linear trend was observed for the other rock types. The peak values of the axial thermal strain, when the desired temperature is reached, are used as an input for the calculation of CLTE.

The CLTE of samples at different temperatures is calculated using equation 2.23 in the literature review (Chapter 2).

Figure 3.21 shows the plot of CLTE versus temperature for all rock types tested.

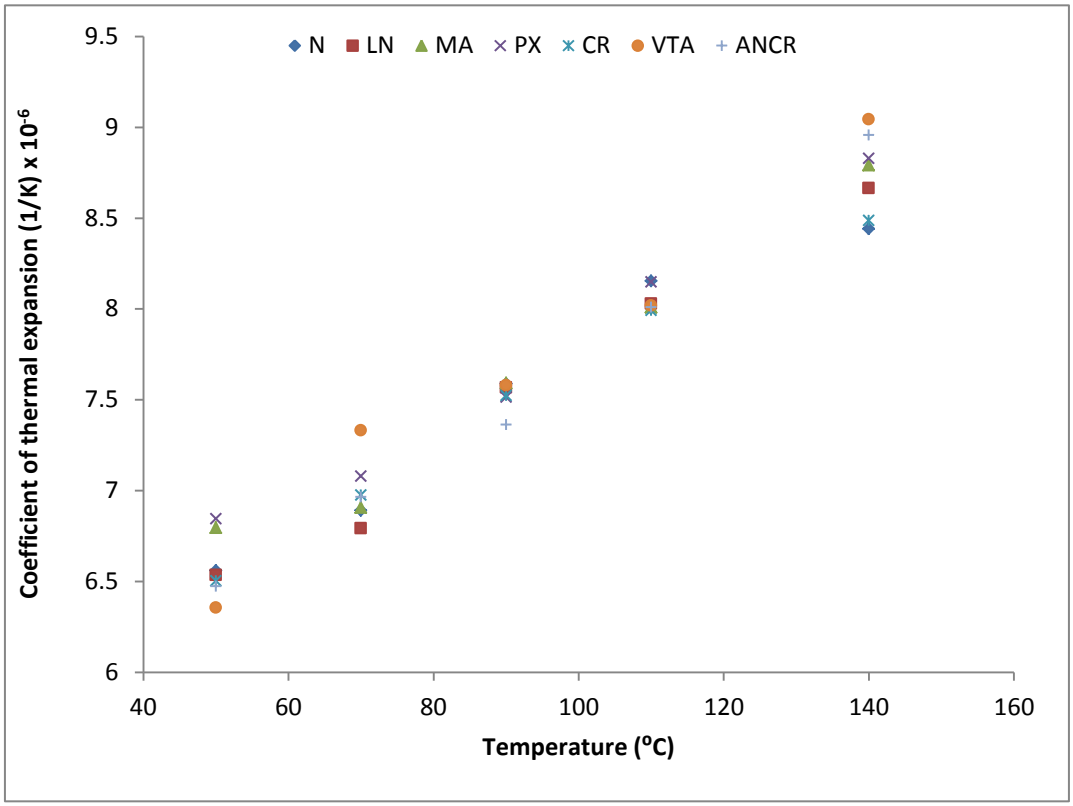


Figure 3.21: Plot of CLTE versus temperature for norite

Figure 3.21 clearly shows that there is a linear relationship between temperature and CLTE. The values of CLTE are input parameters into the numerical modelling. For all the specimens tested, as seen in Figure 3.21, the range of CLTE values are very narrow, particularly at 90° and 110°C. This is not surprising since rocks are igneous. It was seen from the reviewed literature that variation of CLTE could be possible within the same rock type, however, there could be exceptions as well. The notable difference in the values of CLTE for different rocks at 50°, 70° and 140°C could be attributed to the variation of the mineral constituents of rocks.

3.3.4.4 Loading of test specimens for triaxial testing

At the completion of coefficient of thermal expansion test on each rock type, the load and confining pressure on the specimen are removed. The MPT procedure (Figure 3.22) set up was executed for triaxial experiments. The steps are shown in Figure 2.23.

(a) The axial stress and the confining pressure are simultaneously increased until the desired confinement is reached at the rate of 0.5 MPa/minute. The results of a preliminary tests conducted on the selected rocks for this research showed that spontaneous and violent failure commenced at confining pressure of 40 MPa. In order to obtain complete post-peak curves for all the test, confining pressure range of 0 to 30 MPa was used for the main tests. Some of the rocks tested displayed the transition from Class I to Class II due to changes in temperature and confining pressure.

(b) The control mode is then switched to axial strain control and the specimen was loaded at an axial strain rate of 0.001mm/mm/s until approximately 70% of the expected peak force, as suggested by ISRM (1999). Since most of the tested specimens are brittle, the axial strain control mode can only be used in the elastic region of the stress-strain curve.

(c) At 70% of peak force, the control mode was switched to circumferential strain control at the rate of 10^{-6} mm/mm/s, until the applied load falls to 50% of peak force after failure.

(d) The control mode was then returned to axial strain control until the completion of the test in the post-failure stage.

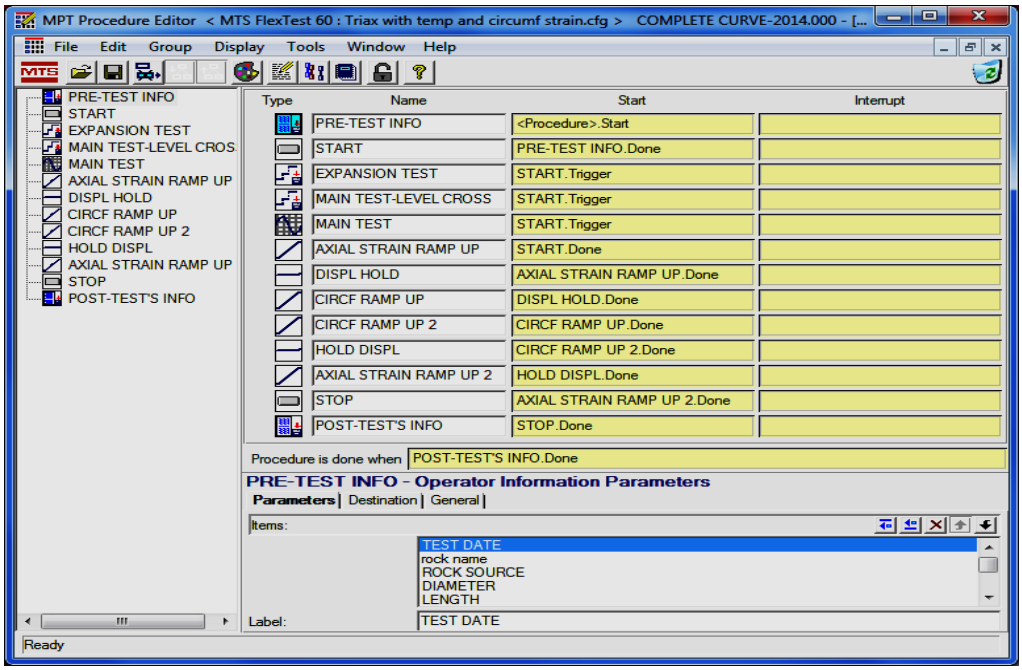


Figure 3.22: Screen shot of the Multi-Purpose-Testware (MPT) procedure for triaxial testing

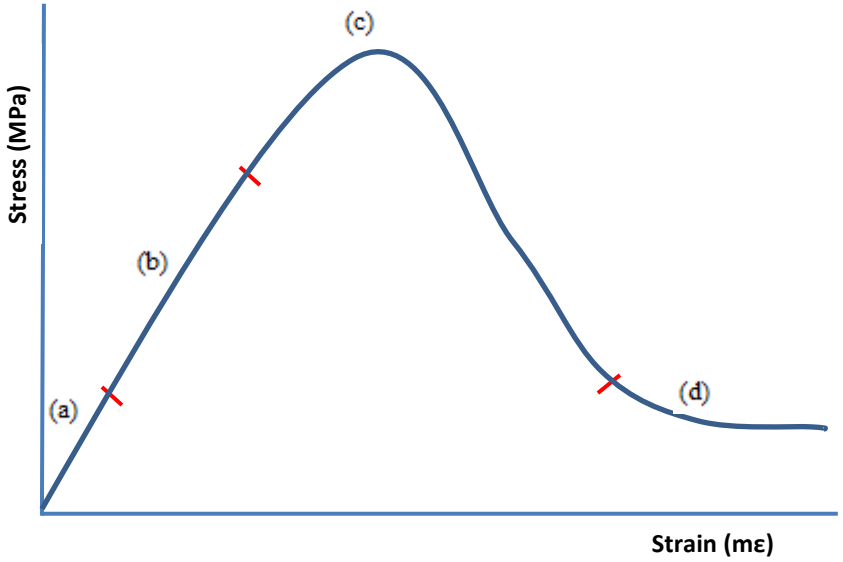


Figure 3.23: Illustration of MPT steps

The use of circumferential strain extensometer as the feedback has been known as the most sensitive means of detecting specimen failure (ISRM, 1999). However, it should be noted that when a pilot test was conducted with circumferential strain as the control mode at 70% of the expected peak stress, the test was unsuccessful. Then dual compensation control mode was used, that is, using a combination of displacement and circumferential strain as the feedback. This was due to the brittle nature of the test specimens.

The displacement, built-in-calculated stress, temperature, confining pressure, axial and circumferential strain were captured in a data file during test execution. From the test data, Young's modulus, Poisson's ratio, shear and bulk moduli, cohesion, internal friction angle and dilation angle, were calculated as was done with the Amsler compression tests. The complete stress-strain curves specimens for norite tested at different temperatures and confining pressure are given in Figures 3.24 to 3.28, while the results of the other rock types are provided in the appendix A3. Figure 3.24 is the graph of norite tested under ambient temperature and confining pressures of 10, 20 and 30 MPa. It can be seen that norite exhibits Class II behaviour with confining pressures of 10 and 20 MPa, while the behaviour at 30 MPa confinement is Class I.

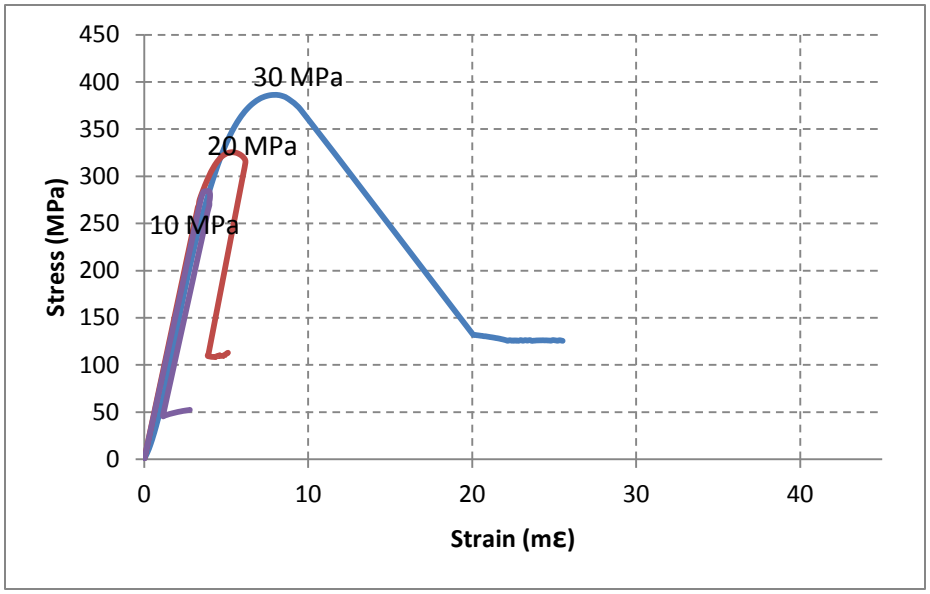


Figure 3.24: Norite tested at ambient temperature and various confinements

Figure 3.25 illustrates the behaviour of norite tested at temperature of 50°C and confining pressures of 10, 20 and 30 MPa. The graph shows similar behaviour to the one tested in ambient temperature, that is, Class II behaviour at 10 and 20 MPa and Class I at 30 MPa confining pressure respectively. This means that increasing temperature to 50°C has no noticeable effect on the behaviour of norite in terms of post peak behaviour.

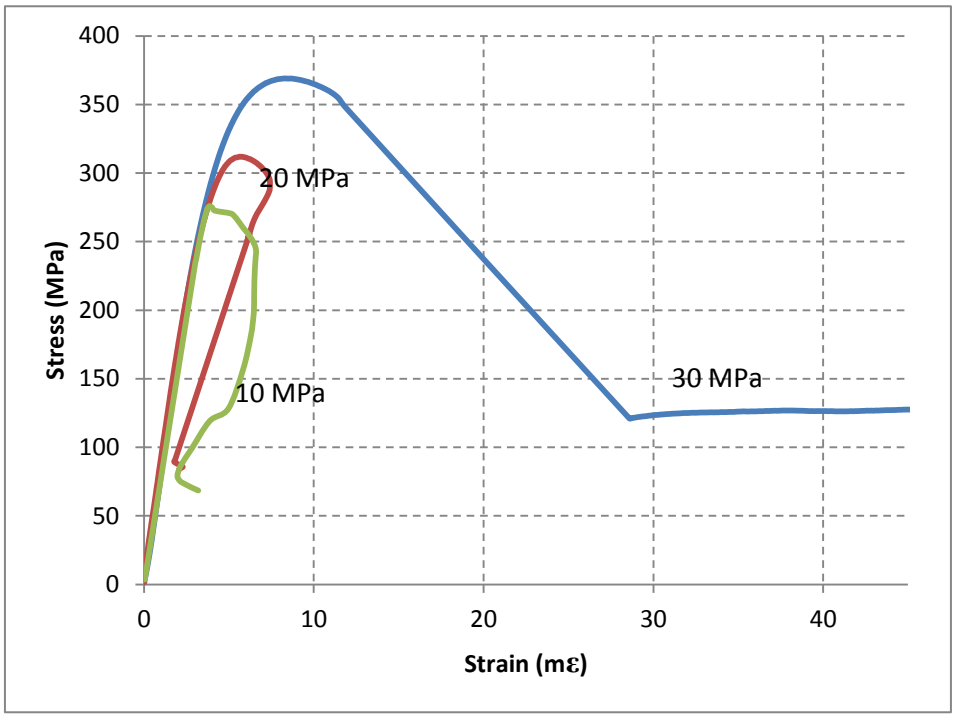


Figure 3.25: Norite tested at 50°C and various confinements

However, there is approximately 3.2% strength reduction on norite specimens at ambient temperature and that of 50°C for confining pressure of 10 MPa. There is also reduction in strength for 20 and 30 MPa norite specimen as shown in Figures 3.24 and 3.25.

Figures 3.26 and 3.27 show the graphs of norite tested at 90°C and 140°C and confining pressures of 10, 20, and 30 MPa.

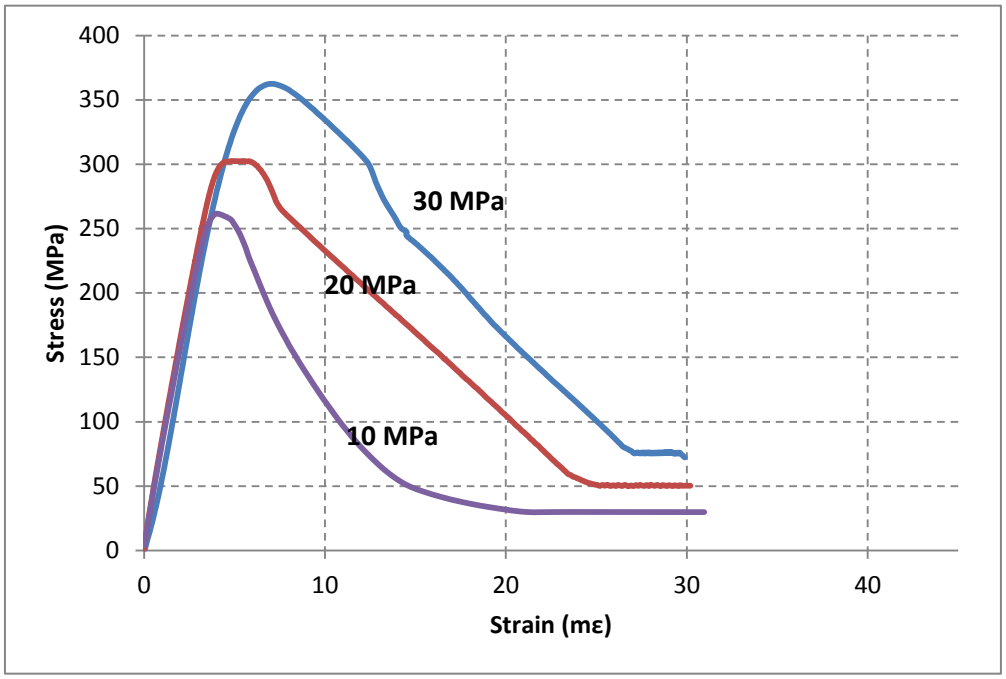


Figure 3.26: Norite tested at 90°C and various confinements

The norite specimens tested at 90°C and 140°C show Class I behaviour at all confining pressures (Figures 3.26 and 3.27). The figures also show slight strength reduction with increasing temperature at a particular confining pressures. The possible reason for the observed Class I behaviour and strength reduction is that increasing temperature causes formation of new cracks or extension and coalescence of existing cracks within the specimens.

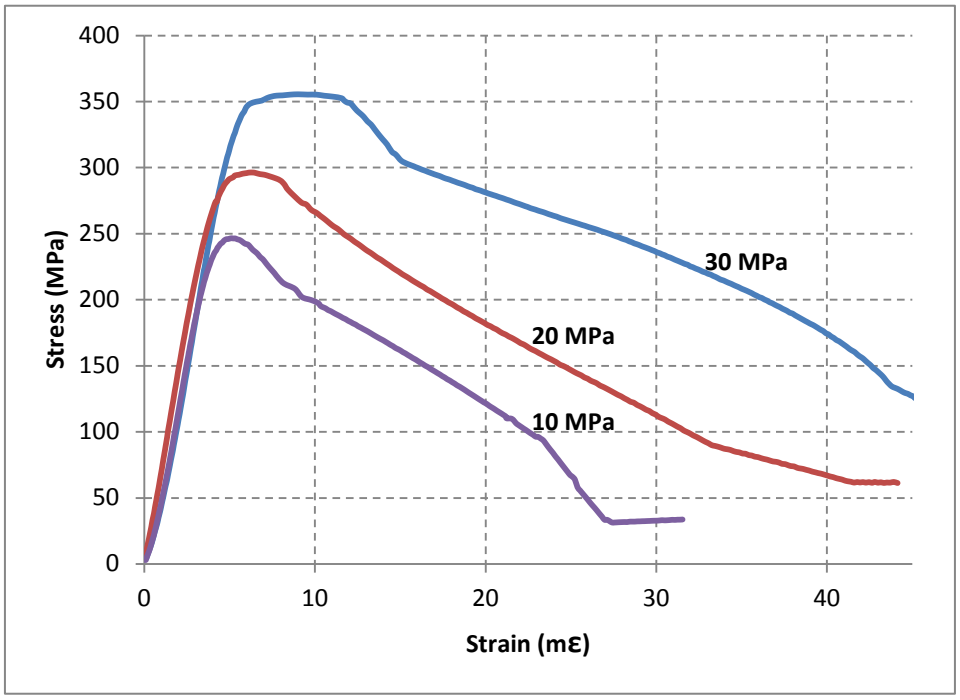


Figure 3.27: Norite tested at 140°C and various confinements

Figure 3.28 shows the stress-strain plots of norite tested at ambient temperature, 50°, 70°, 90°, 110°, 140°C and confining pressure of 10 MPa.

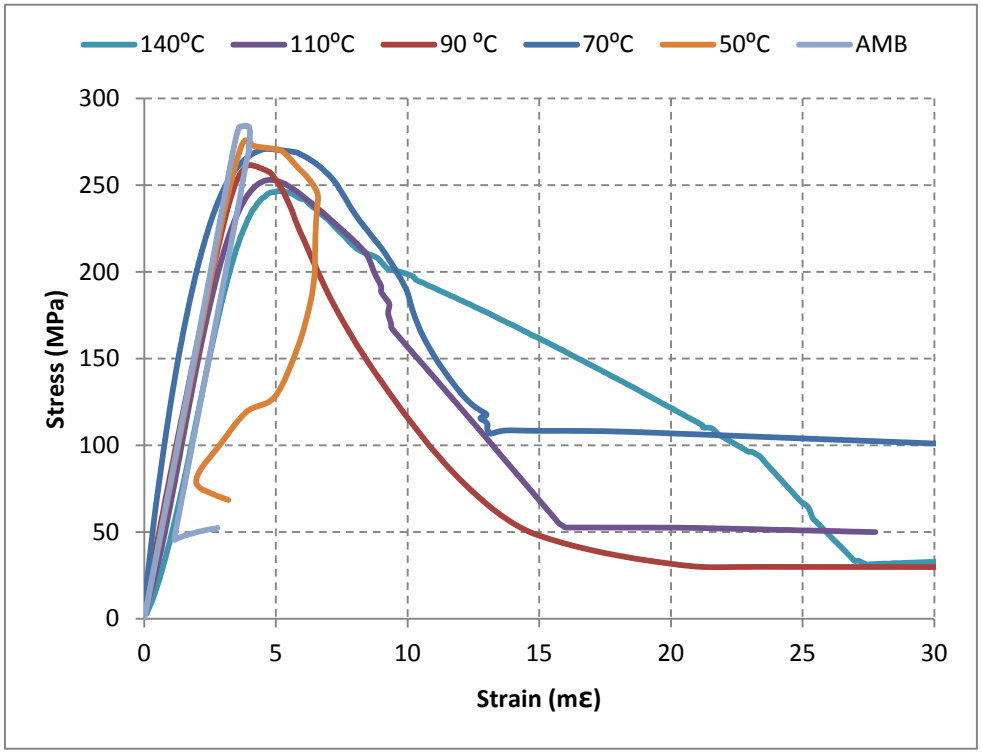


Figure 3.28: Norite tested at 10 MPa confinement and various temperatures

As can be seen in Figure 3.28, norite displayed Class II behaviour at ambient temperature and 50°C, while at higher temperatures Class I behaviour was observed.

Tables 3.7 shows the values of Young's modulus and Poisson's ratio for Norite at ambient, 50°C, 90°C, 140°C and confining pressures, 0, 10, 20 and 30 MPa. It can be seen that the Young's modulus and strength decrease with increasing temperature. For instance, when norite testing is compared at 10 MPa and ambient temperature with that of 10 MPa and 140°C, there is 10.7% and 13% reduction in Young's modulus and strength respectively.

Table 3.7: Young's modulus, Poisson's ratio and strength of norite

Confinements	**Young's modulus (GPa)**			
	20°C	50°C	90°C	140°C
0 MPa	65.0	64.5	64.1	63.6
10 MPa	79.6	77.7	74.3	71.1
20 MPa	81.8	78.5	76.0	74.9
30 MPa	83.2	79.6	77.3	75.7
	Poisson's ratio			
0 MPa	0.34	0.33	0.33	0.34
10 MPa	0.34	0.32	0.34	0.33
20 MPa	0.34	0.33	0.34	0.33
30 MPa	0.34	0.33	0.33	0.34
	Peak strength (MPa)			
0 MPa	163	161	160	159
10 MPa	284	275	262	247
20 MPa	325	312	302	296
30 MPa	386	369	362	356

In Table 3.7, there is no particular trend observed on the influence of temperature on the Poisson's ratio of norite. The Poisson's ratio ranges between 0.32 and 0.34 for all the tests irrespective of temperature and confinement increase. Similar observation was noticed for the other rock types.

3.4 Influence of temperature on Young's modulus and strength

Table 3.8 shows the percentage reduction in strength and Young's modulus of the tested rocks due to temperature increase from 20°C to 140°C. The results in Table 3.8 are for 10 MPa confinement.

Table 3.8: Reduction in strength and Young's modulus of the tested rocks due to temperature increase from 20°C to 140°C

REDUCTION	CR	LN	MA	N	PX
% reduction in strength	20.7	15.4	18.5	13.3	18.9
% reduction in Young's modulus	11.7	9.8	8.3	10.7	6.7

It can be seen from Table 3.8 that there is significant reduction in the strength and Young's modulus of the rocks, with Chromitite having the highest reduction values.

3.4.1 Regression analyses

A simple linear regression model ($y = mx + c$) was established for the temperature-dependent Young's modulus (E_t), where ambient Young's modulus (E_a) is the constant "c". The gradient "m" is determined from the Young's modulus versus temperature plot, Figure 3.28, for various rock types. Three specimens were tested per rock type per temperature (20°, 50°, 70°, 90°, 110°, and 140°C) at 10 MPa confining pressure and the average Young's modulus was used as the data points for the scatter plot. Therefore, the regression analysis is only valid at 10 MPa confining pressure and the specified temperatures. Further testing is required to verify the applicability of the regression equation to the other ranges of confinement and temperatures.

As Figure 3.29 shows, the correlation coefficients "R^2" range between 0.95 and 0.99, that is indicative of strong correlations between Young's modulus and temperature. The gradient "m" ranges between -0.058 and -0.100. As observed in Figure 3.29, the

intercept values (red circles) are values of $E_{t=0}$, which are higher that E_a (that is $E_{t=20}$). In order to correct for this, a value of -0.055 is used in equation 3.5.

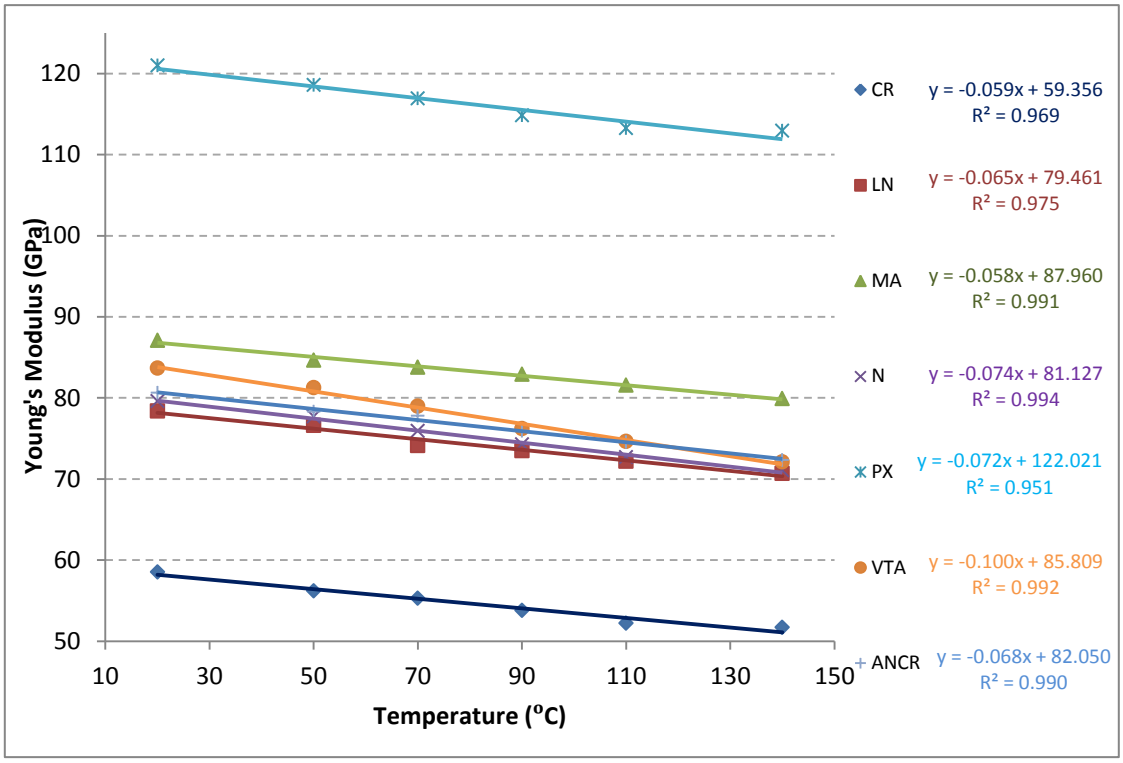


Figure 3.29: Young's modulus and temperature relationship for various rock types

The data provided in Table 3.7 and Figure 3.29 is utilised to develop a simple linear regression model (y = mx + c) between temperature and Young's modulus considering that the temperature will increase as mining goes deeper. The ambient Young's modulus (E_{amb}) becomes the constant "c". The gradient "m" is evaluated for each rock type in Figure 3.29. Therefore, the following general equation can be written to estimate the Young's modulus for a particular rock subject to increasing temperatures:

$$E_t = -m\,(T - T_{amb}) + E_{amb} \qquad (3.5)$$

Where ; E*t* is the temperature dependent Young's modulus (GPa)

T is any temperature between 20°C and 140ºC ($T \geq T_{amb}$)

T_{amb} is the ambient temperature (in this case 20°C)

It should be noted that E_{amb} is the Elastic modulus taken from Table 3.7 at 20ºC and not the zero intercept provided in Figure 3.29. The "m" value is rock type dependent. For example, norite (N) has E_{amb} magnitude of 79.6 GPa (Table 3.7) and m value of -0.074 (Figure 3.29). Further research is required to check the sensitivity of "m" value to confinements other than 10 MPa.

Although the ambient temperature used in equation 3.5 is 20°C, it is assumed that specimens tested at 20°C ± 5°C would still be accommodated. This is based on the information provided by Kruger and Shongwe (2004), who reported that the average annual temperature of South Africa for 1960 to 1990 and 1991 to 2003 as 18.18°C and 18.48°C respectively. This temperature given is that of outdoor. It implies that the ambient room temperature used in in equation 3.5 falls within acceptable range.

The comparison of the Young's modulus determined from actual laboratory testing and the one estimated using equation 3.5 is given in Figure 3.30. Only two of the rocks are provided as examples in Figure 3.30. The percentage difference between the laboratory determined values and the ones calculated from equation 3.5 is negligible as shown in Figure 3.30 and Table 3.9.

Table 3.9: Percentage difference between laboratory measured and calculated Young's modulus

	50°C	70°C	90°C	110°C	140°C	Absolute average
CR	-0.97	-0.50	-1.12	-1.92	0.52	0.84
LN	0.26	-1.36	-0.44	-0.44	0.17	0.45
MA	-0.81	-0.51	-0.17	-0.39	-0.30	0.36
N	0.42	0.01	-0.19	-0.37	0.48	0.25
PX	-0.21	-0.41	-0.98	-1.12	0.52	0.54
VTA	0.76	0.42	-0.58	-0.03	0.61	0.40
ANCR	-0.37	0.73	0.11	0.04	-0.18	0.24

Note: Negative sign denotes underestimation, while positive denotes overestimation.

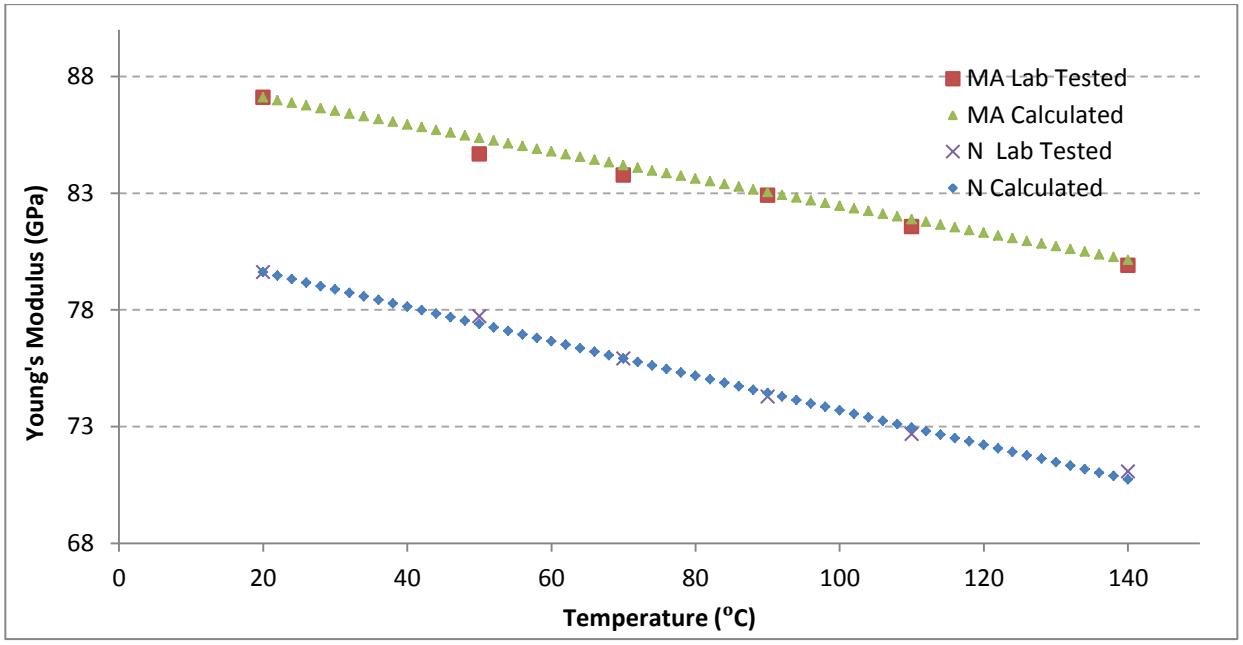


Figure 3.30: Comparison of laboratory tested and calculated Young's modulus for two rocks

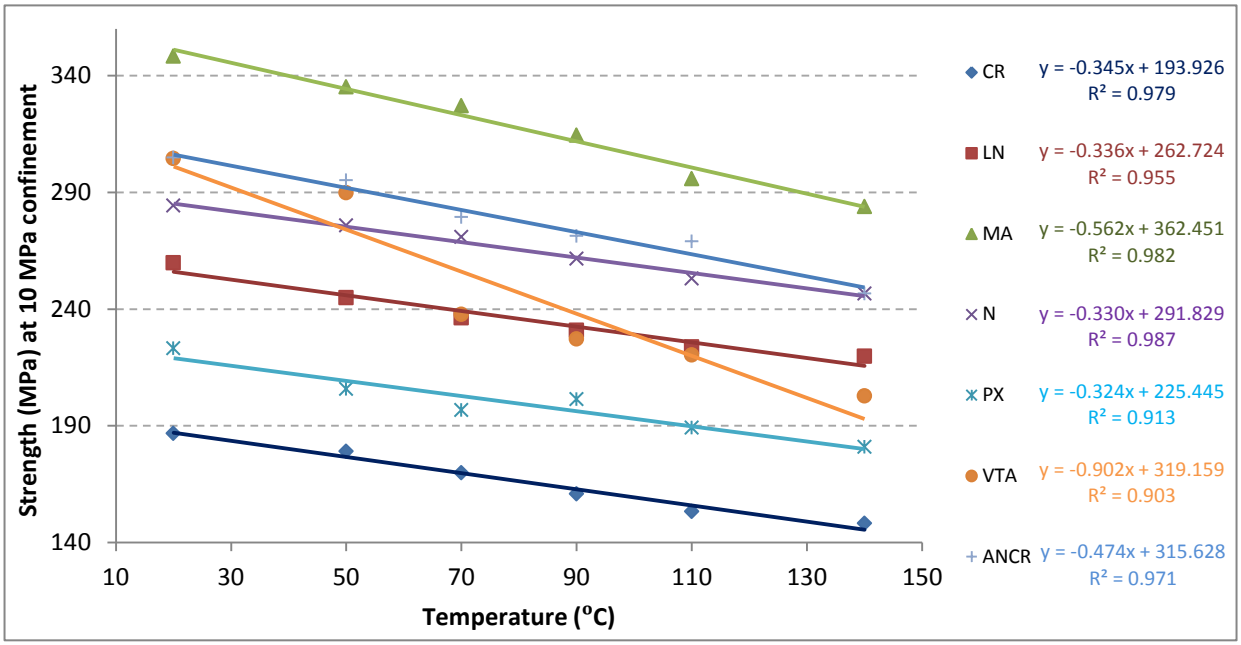


Figure 3.31: Strength behaviour against temperature at 10 MPa confinement

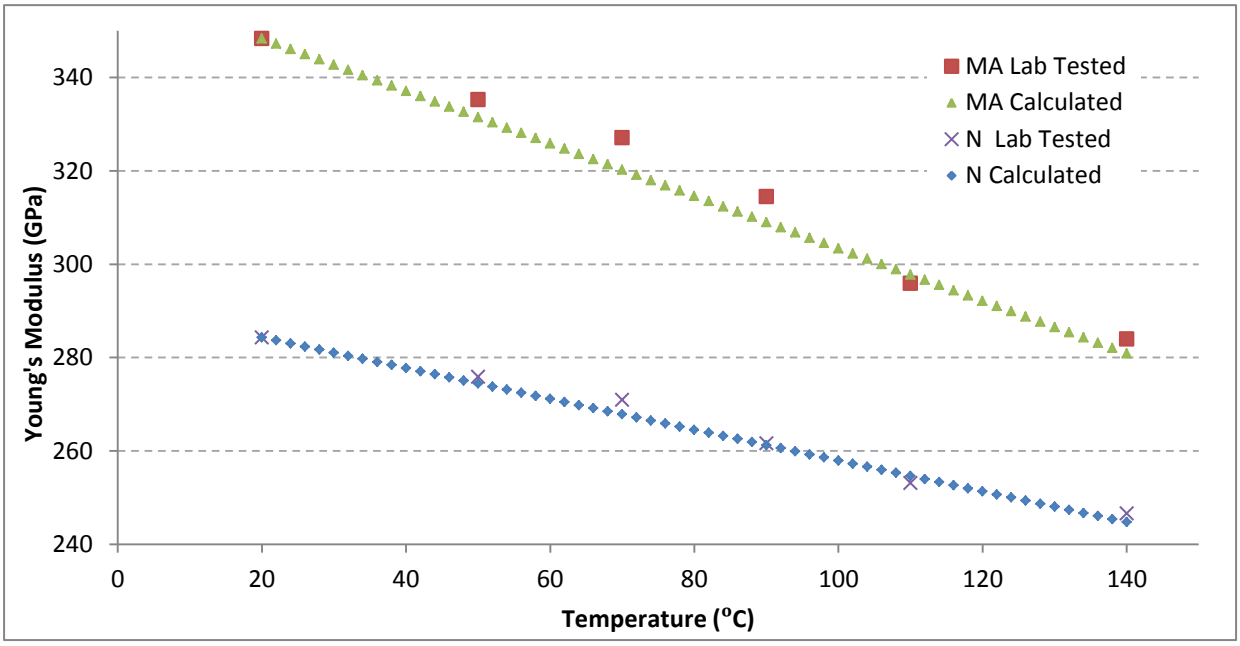


Figure 3.32: Comparison of laboratory tested and calculated strength for two rocks

The percentage difference for all rock types for the temperature range is between -1.92% and 0.76%. The highest percentage difference in absolute terms occurs with CR and the lowest is with ANCR. Following similar steps as explained for temperature-dependent Young's modulus, a linear regression model (equation 3.6) was also established for temperature-dependent peak strength from the plot in Figure 3.31.

$$\sigma_t = -m(T - T_{amb}) + \sigma_{amb} \quad (3.6)$$

Where ; σ_t is the temperature dependent strength (MPa)
T and T_{amb} are as explained in equation 3.5
σ_{amb} is the strength measured at ambient temperature

The comparison of the laboratory-measured strengths and the one estimated from equation 3.6 is given in Figure 3.32, while Table 3.10 shows the percentage differences. The variation between the laboratory values and the ones derived from the proposed equation 3.6 is again negligible, except for that of VTA. This variation could be attributed to the inconsistencies in the mineralogical composition of VTA or the presence of internal micro-cracks.

Table 3.10: Percentage difference between laboratory measured and calculated strength

	50°C	**70°C**	**90°C**	**110°C**	**140°C**	**Absolute average**
CR	1.48	0.19	-1.09	-1.57	1.89	1.04
LN	-2.03	-2.89	-2.39	-2.63	0.10	1.67
MA	1.12	2.09	1.75	-0.64	1.07	1.11
N	0.51	1.14	0.15	-0.60	0.75	0.53
PX	-3.68	-5.19	0.44	-2.53	-1.79	2.27
VTA	4.32	-9.01	-6.14	-1.21	3.39	4.01
ANCR	1.50	-0.66	-0.13	2.50	-0.56	0.89

It is suggested that equations 3.5 and 3.6 are used for determining the corresponding reduction in Young's modulus and strength respectively with

respect to virgin rock temperature as input values for numerical modelling and for subsequent underground rock engineering design.

3.5 Effect of temperature on cohesion and angle of internal friction.

The angle of internal friction and cohesion were calculated in section 3.3.3 from the results of triaxial tests. The angle of internal friction and cohesion were plotted against temperature in Figures 3.33 and 3.34 respectively. The data for anorthosite-chromitite (ANCR) and varitextured-anorthosite (VTA) were not included since the mottled-anorthosite and chromitite are already plotted. It is clear from Figures 3.33 and 3.34 that the angle of internal friction and cohesion drop in similar magnitudes with increasing temperature.

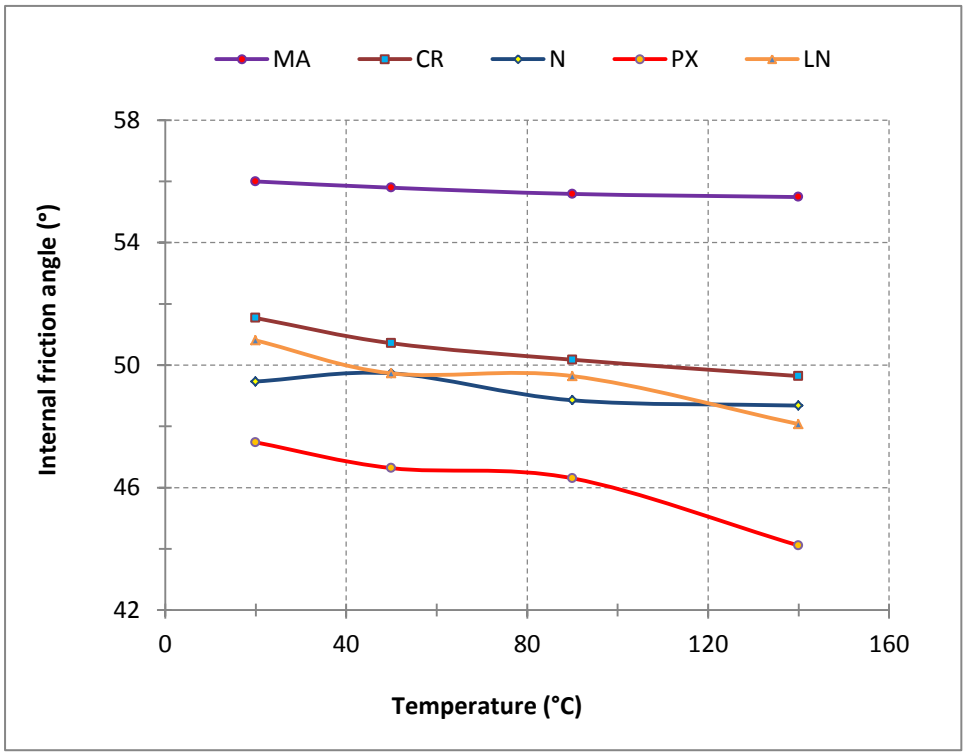


Figure 3.33: Angle of internal friction at various temperatures

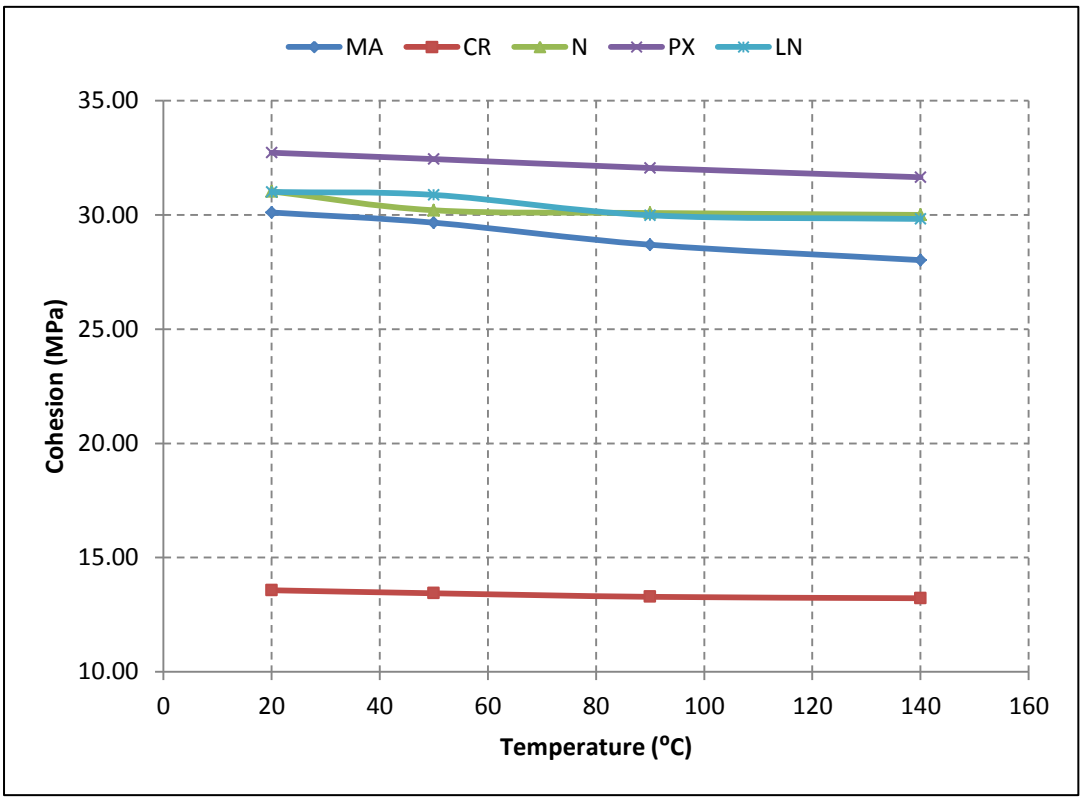


Figure 3.34: Cohesion at various temperatures

3.6 The determination unconfined Coefficient of Linear Thermal Expansion (CLTE)

The procedure for the determination of unconfined CLTE is as follows:

A. Sample preparation; Black/white markers were attached on the longitudinal direction of the cylindrical core specimens as shown in Figure 3.35a. White markers were used for specimens with dark-coloured minerals, while black markers were used for specimens with light-coloured minerals for sharp colour contrast. The markers are spaced 15mm apart. Two holes were drilled in each of the specimen for the insertion of temperature probe. The reason for having the two holes is for monitoring temperature magnitudes at the lower and upper parts of the specimens to

see any significant variation. Eventually, the average of both probes were used for analysis.

B. The specimen is then placed in the oven and heated at a constant rate of 2°C/minute. This heating rate was chosen to avoid any cracking due to stress produced by thermal gradient, as suggested by Richter and Simmons (1974). The control of heat was done with the aid of variac attached to the heating element in the oven (Figure 3.36). Temperature increase was monitored through two digital thermometers that are connected to the temperature probes on the specimen. Having two thermometers increases the accuracy temperature measurements. The thermometers have indicators showing the targeted temperature, the actual specimen temperature during testing and time as seen in Figure 3.36.

C. The thermal strain is measured with a video extensometer (version LC/XY) that is capable of measuring strain at any temperature. The principle of strain measurement uses the identification of barycenter (the distances between two markers, see Figure 3.37, that depends on the position of markers on the specimen in real time. The length from the centers of markers are measured with a Vernier caliper and are provided as an input during the calibration stage prior to the commencement of testing. The video extensometer software then caliculates thermal strain, εt, which is the ratio of the change in length to the original length due to heat.

D. The specimen had to be lit up with an external light source positioned directly in front of the transparent glass of the oven for illumination purposes and better contrast. The camera was levelled carefully on the axis of the specimen and measurement of strain starts at the trigger of the temperature control switch of the variac (Figure 3.36). The strain and time were continuously recorded in a text file on the computer. A more detailed description of thermal strain measurement using the video extensometer is provided in appendix A4.



Figure 3.35: Rock specimens with markers for a) axial and b) transverse thermal strain measurements

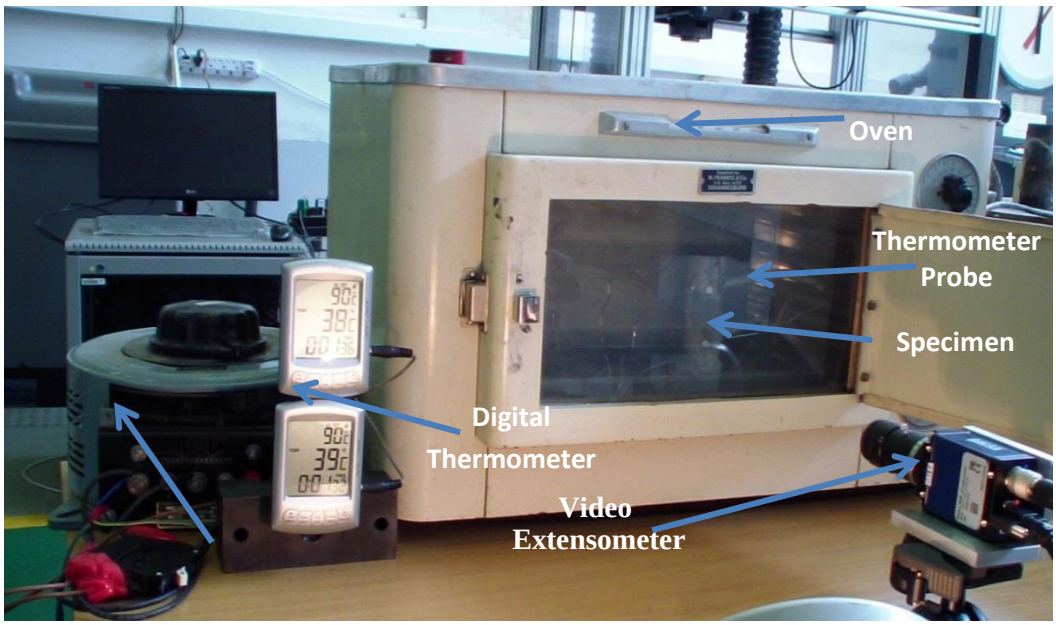


Figure 3.36: Experimental set-up for thermal strain measurements

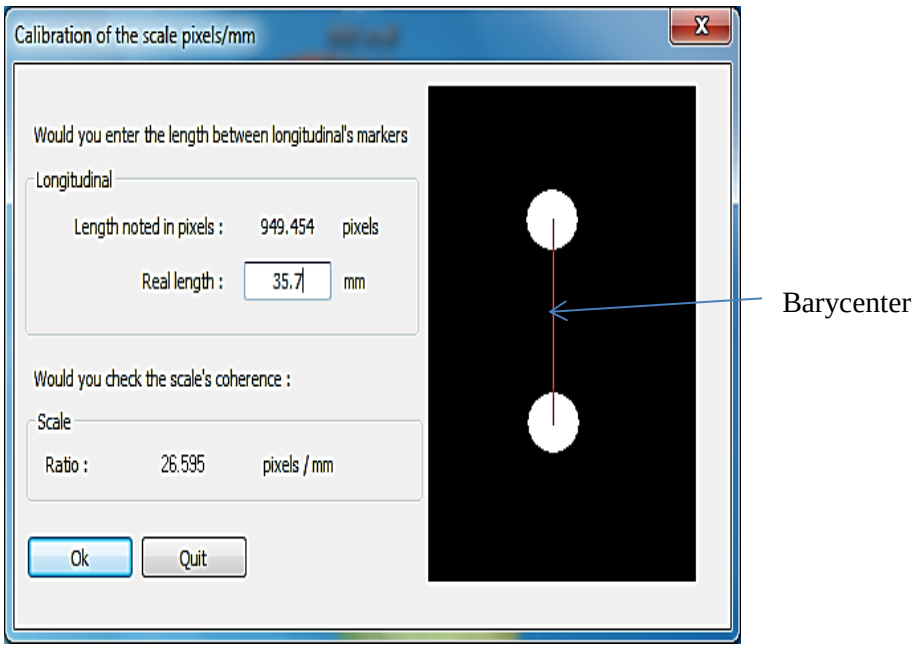


Figure 3.37: Illustration of barycenter

The temperature of the samples before being heated was approximately 25°C. Samples were then heated up to temperatures of 50°, 70°, 90°, 110°, and 140°C. As mentioned earlier (section 3.6 (B)), heating rate of 2°C/minute was used, which means that the temperatures of 50°, 70°, 90°, 110°, and 140°C were reached in approximately 1500, 2100, 2700, 3300 and 4200 seconds respectively (Figure 3.37). When the required temperature is achieved, the temperature is kept constant for about 20 minutes to allow for even distribution of heat within the oven and the specimen. However, this final stage causes no further thermal strain increment; therefore, the data from the final stage onwards is not included in the graphs. In order to avoid the influence of previous heating cycle on the results, separate specimens were used for each test at temperatures of 50°, 70°, 90°, 110°, and 140°C.

The CLTE of the samples at different temperatures is calculated using equation 2.3 in section 2.3 of Chapter 2.

Sample calculation for mottled anorthosite

Thermal strain at 110°C = -0.000740 (-ve sign means expansion)

Initial temperature = 25°C

Final temperature = 110°C

Change in temperature = (110-25)°C = 85°C

Therefore,

$$\alpha_l = \frac{|-0.000740164|}{110 - 25} = 8.71\ x\ 10^{-6}$$

Figure 3.38 shows the plot of axial strain against time for mottled anorthosite, while Table 3.11 shows the values of CLTE for all the specimens tested under unconfined condition. The graphs of other samples are presented in appendix A5. The absolute values of thermal strain are used for plotting, though going by rock engineering convention, expansion is negative. It should be noted that at the on-set of heating, anomalous expansion/contraction was observed, which makes some of the values to be in the positive and negative range. As heating continues, specimen becomes more stable and exhibits expansion. In addition, due to testing in unconfined condition, the expansion is not as linear as those obtained in confined condition.

While comparing the values of CLTE in confined and unconfined condition, it is observed that the applied confining pressure of 3 MPa during the expansion test lowers the CLTE coefficient. For example, the CLTE for mottled anorthosite for temperatures of 50°, 70°, 90°, 110°, and 140°C under unconfined and confined conditions are 8.13, 8.32, 8.58, 8.71, 9.14 and 6.80, 6.91, 7.59, 8.00, 8.79; respectively (Figure 3.21 and Table 3.11).

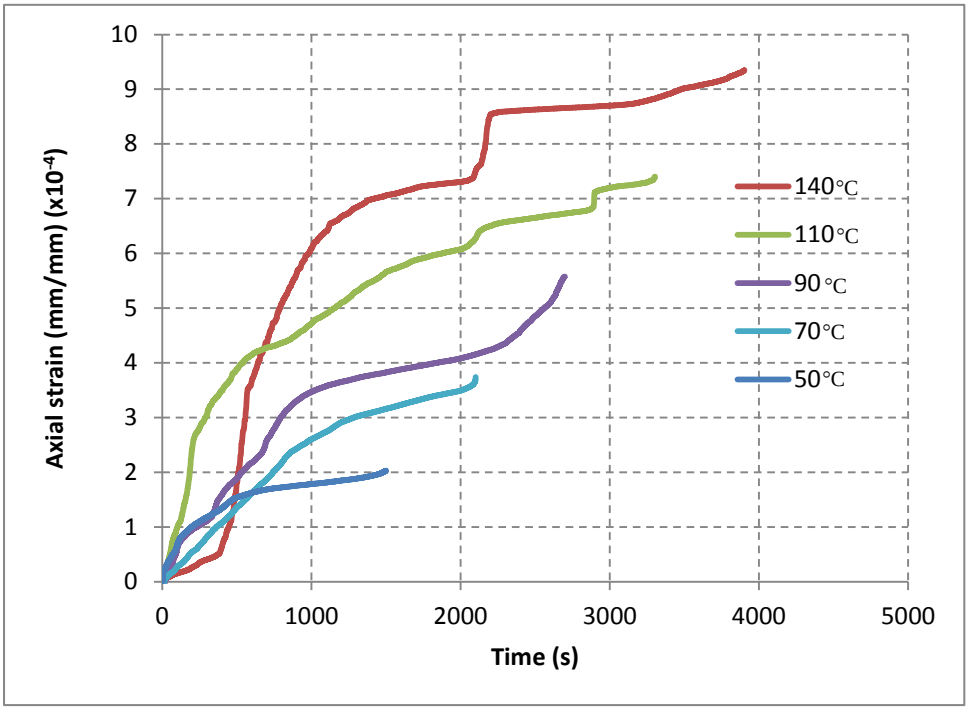


Figure 3.38: Axial strain versus time for mottled anorthosite at different temperatures

Table 3.11: The coefficient of linear thermal expansion (α_l) -unconfined

TEMPERATURE (°C)	CLTE (*10^{-6})/K								
	CR	N	GN	LN	VTA	GF	MA	PX	G
50	7.93	8.25	7.80	8.06	8.00	7.74	8.13	8.14	7.91
70	8.14	8.44	8.00	8.24	8.22	7.87	8.32	8.30	8.11
90	8.37	8.63	8.22	8.49	8.41	7.96	8.58	8.54	8.31
110	8.57	8.75	8.48	8.64	8.62	8.03	8.71	8.73	8.59
140	8.94	9.16	9.33	9.09	9.14	9.02	9.14	9.05	9.24

3.7 Dilations angles of BIC rocks

The dilation angle of five rock specimens are determined from triaxial test carried out on the BIC rocks at confining pressure of 10 MPa and temperature ranging

from ambient (approximately 20°C) to 140°C. The tests were done in the MTS hydraulic servo-control testing machine described in section 2.4.2.1 of the literature review.

Axial and circumferential strains were measured with extensometers (Figure 2.31-Chapter 2). Volumetric strain was plotted against the axial strain and the slope of the plot is used in calculating a set of three dilation angles; the pre-peak, post-peak and residual dilation angles. The volumetric strain was calculated by summing the axial strain and twice the circumferential strain. The point of the pre-peak was taken where the volumetric strain changes from positive to negative up to the peak stress, while that of the post-peak was taken from the peak stress up to 10% stress drop from the peak value. The residual dilation angle was calculated from strain values at the stage where the rocks have the lowest load-bearing capacity. The dilation angles were derived from equation 2.17.

A sample of the stress /axial/volumetric strain and volumetric-axial strain graph is given in Figure 3.39 for chromitite tested at confining stress of 10 MPa and temperature 70°C. Volumetric strain versus axial strain graph in Figure 3.39 is reproduced in Figure 3.40 for easy reference. Figure 3.41 shows the plot of pre-peak, post-peak and residual dilation angles against temperature for chromitite. The plots of pre-peak, post-peak and residual dilation angles for other rock types are given in Appendix A6. Figure 3.42 illustrates the post-peak dilation angles for all rocks tested.

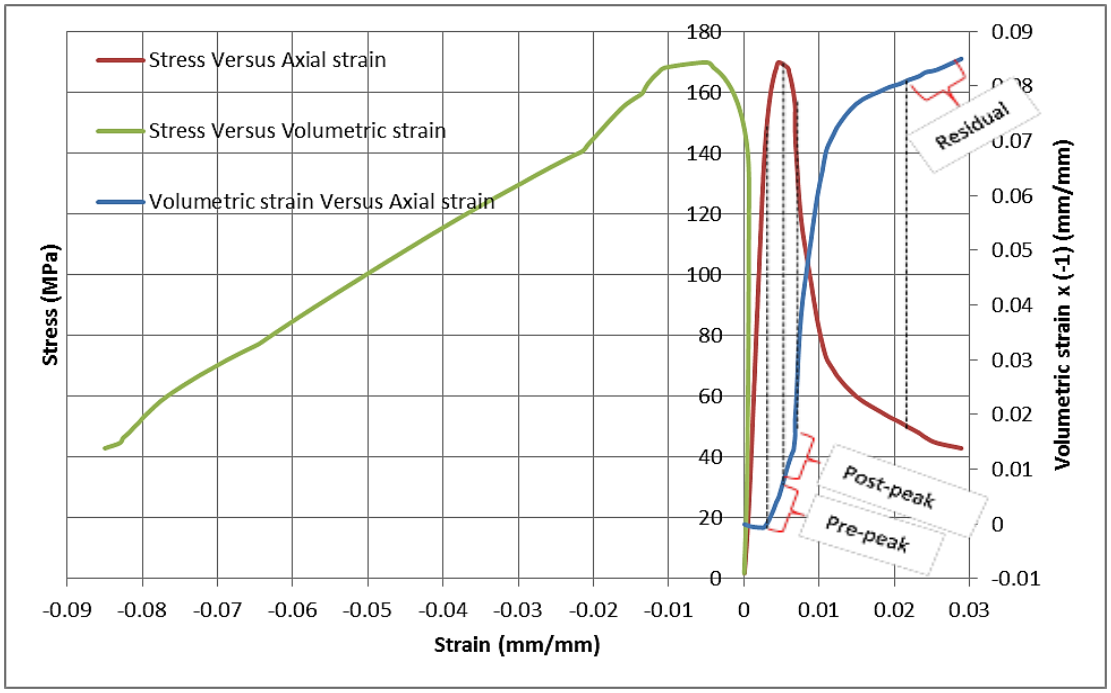


Figure 3.39: Plot of stress/axial/volumetric strain for chromitite at 70°C /10 MPa

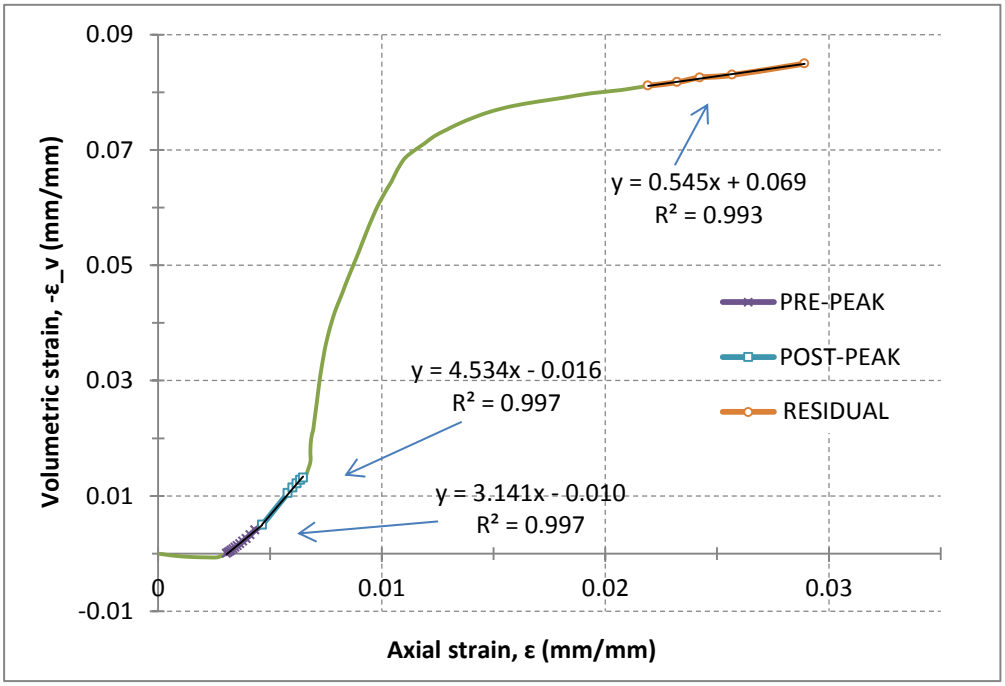


Figure 3.40: Plot of volumetric-axial strain for chromitite

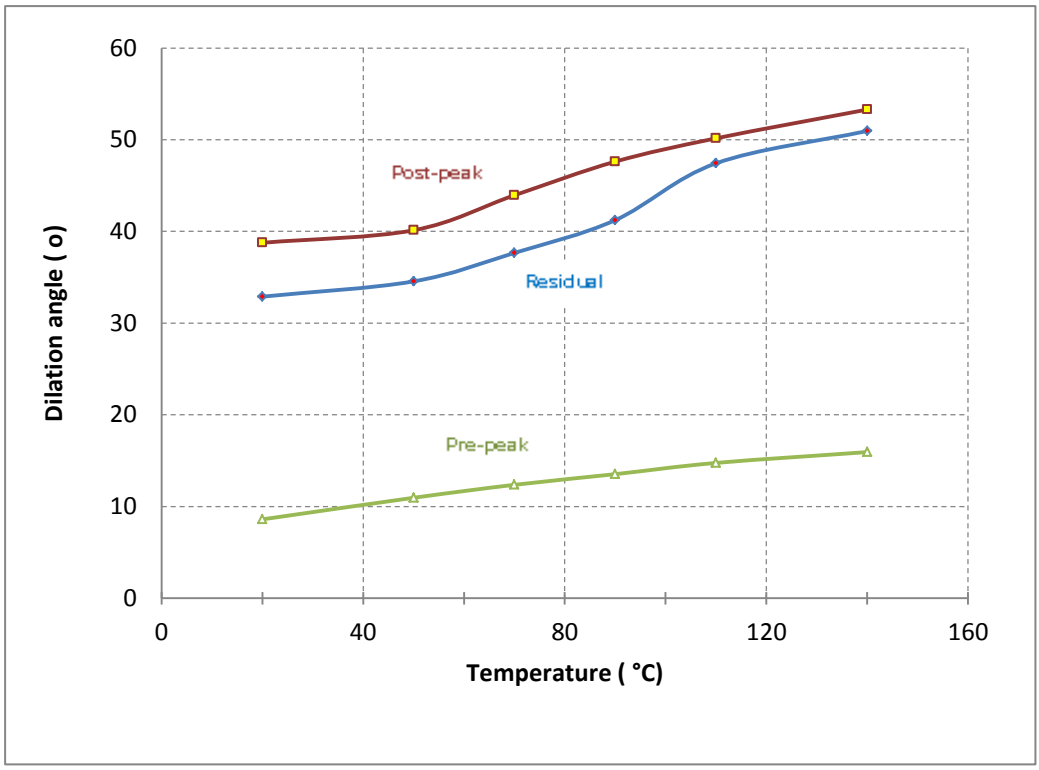


Figure 3.41: Plot of dilation angle against temperature for chromitite

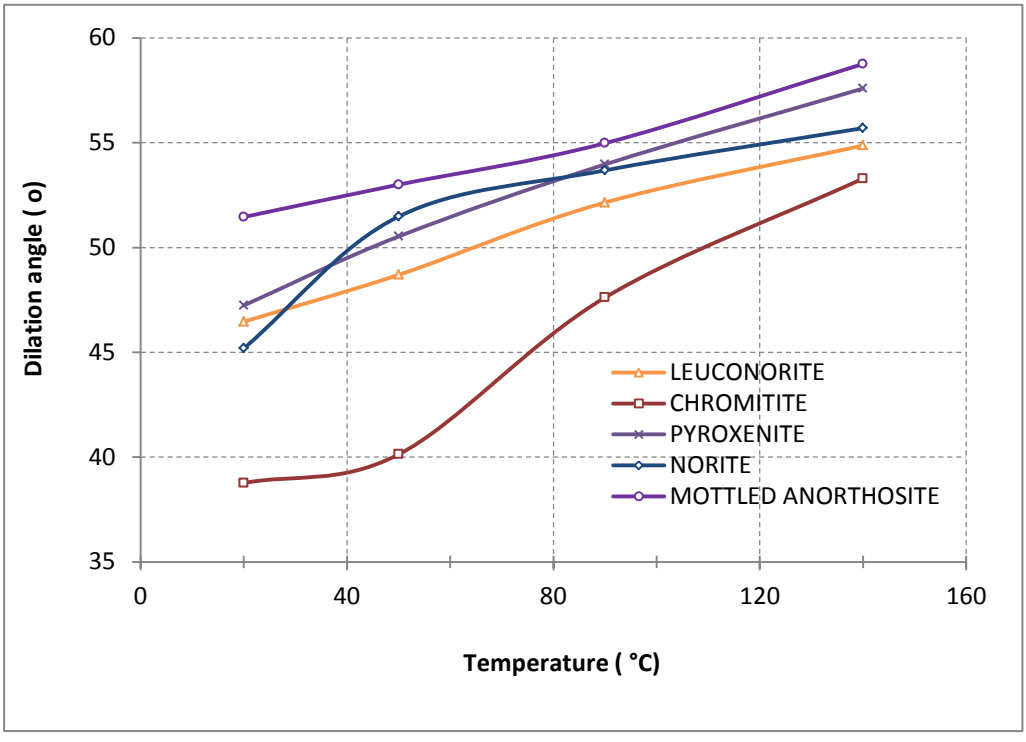


Figure 3.42: Effect of temperature on post-peak dilation angle of BIC rocks

The general trend is that increase in temperature causes increase in dilatancy at pre-peak, post peak and residual stage of rock deformation as shown in Figures 3.41 and 3.42. The values of the pre-peak dilation angles for chromitite are considerably smaller than the post-peak and residual dilation angles. The same observation goes for the other rock types. This is partly due to the fewer cracks that are not interlinked at pre-peak stage, while at peak and post-peak stage; more cracks are generated as a result of increasing axial load and heat energy. The load and heat energy result in the weakening of the bonds within the grains of the rock samples and contributes to higher volumetric expansion. Of all the samples tested, chromitite has the lowest dilation angle, as evident in Figure 3.42; this could be due to its lower strength and Young's Modulus (Figures 3.28 and 3.30). Chromitite has weaker bonding within the grain boundaries and thus has lower volumetric expansion when loaded under confined condition. This shows that temperature contributes to crack initiation, generation and extension, which caused reduction in the strength of the rocks. It is an indication that as mining depth increases in platinum mines, temperature and stress related failures would also increase. The laboratory measurement of the coefficient of thermal expansion also indicated that there was volumetric expansion of the heated rocks, which is directly related to the thermal cracks induced by the heat energy (thermal stress). The thermal cracks were also observed in the microscopic analyses of the heated rocks that are cooled afterwards and viewed under the microscope. This situation could exist when the immediate walls of excavations at deep levels are cooled through ventilation.

3.8 Influence of temperature and loading on P- and S-wave velocities

Two types of non-destructive tests were carried out on nine BIC rock types to examine their response in terms of their P-wave velocity (V_p) and S-wave velocity (V_s). The first test is the temperature test, where temperature is increased from approximately 20°C to 140°C. The second test is the compression test, in which the P- and S-wave velocities are determined with axial stresses of 10, 20 and 100 MPa on the specimens. The diameter of all the test specimens is 42 mm while the

lengths vary. Both tests were done individually on the same specimen. In order to ensure efficient and uniform energy transfer from/to transducers, lubricating oil was applied to the ends of the specimens prior to placement in between the transducers.

3.8.1 Temperature-ultrasonic tests

The dimensions and mass of the specimens were measured and recorded (Table 3.12). The ultrasonic tests were firstly performed on the specimens prior to heating, to determine the P- and S-wave velocities in ambient condition. The experimental set-up is shown in Figure 3.43. After the ambient ultrasonic measurements, the specimens were kept for 2 hours in the oven at 145°C. It was not possible to position the transducers inside the oven and carry out the ultrasonic test for two reasons. Firstly, there was not enough space to allow coupling of transducers onto the specimens.

The second and more important reason is that cables of the transducers would have been affected by high level of heat. Therefore, the specimens were taken out of the oven and immediately placed for ultrasonic measurement. Although, the oven is positioned close to the ultrasonic testing apparatus, (Figure 3.43), approximately 5°C is lost due to the movement of specimen and time interval required for measurements.

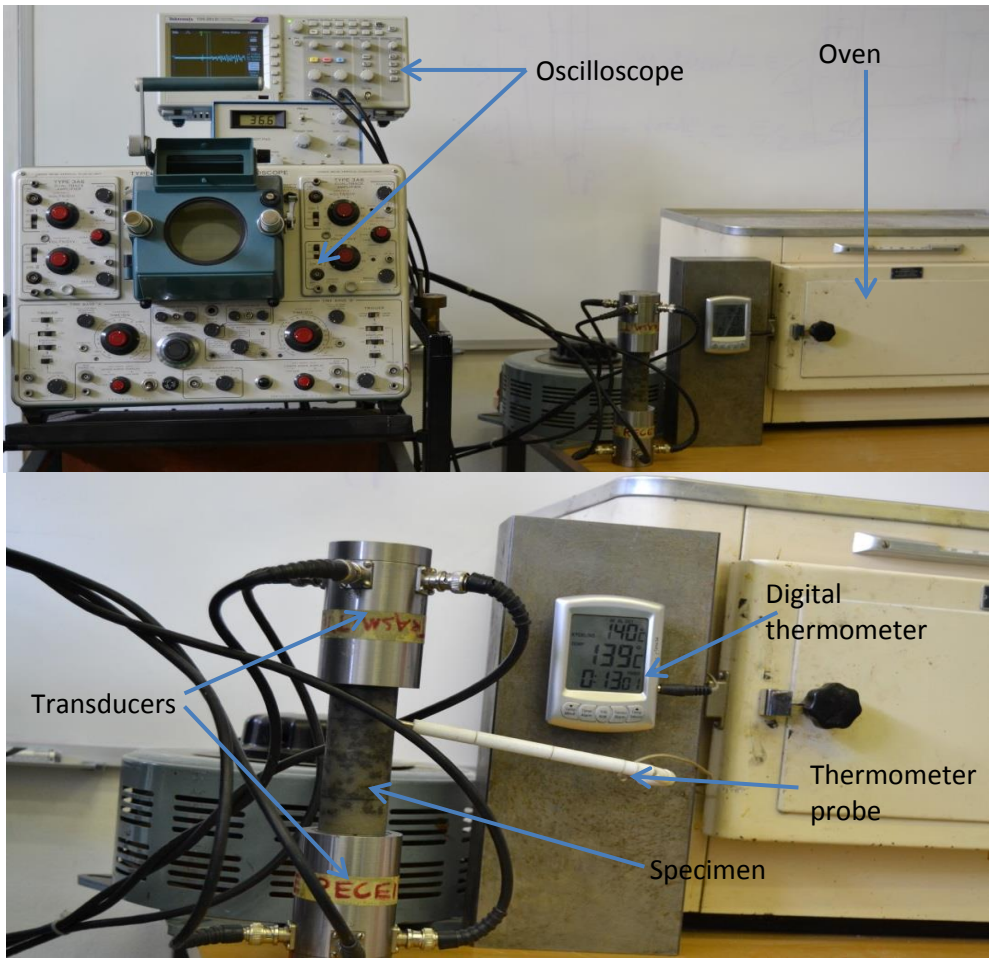


Figure 3.43: Experimental set-up for temperature-ultrasonic tests

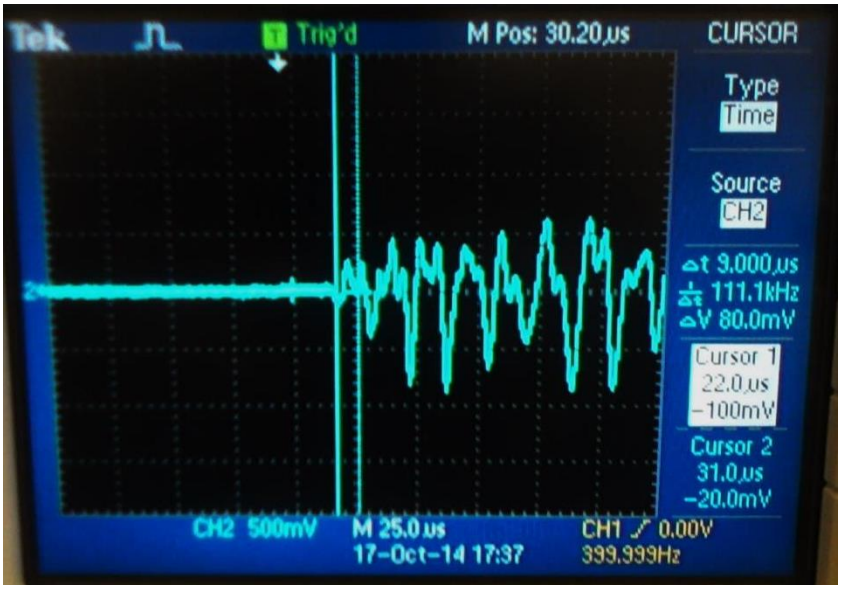


Figure 3.44: Sample screen shot of P-wave measurement at 140°C for MA

The P- and S-wave velocities were calculated from the measured specimen lengths and travel times. Figure 3.44 shows a sample screen shot of P-wave measurement at 140°C for MA. The P- and S-wave travel times are provided in Table 3.12, while Figure 3.44 shows the plots of P- and S-wave velocities versus temperature.

Table 3.12: Specimen dimensions and velocities (temperature-ultrasonic tests)

Specimens	Diameter (mm)	Mass (g)	Length (mm)	P-wave		S-wave	
				V_{amb} (m/s)	$V_{140\,^{o}C}$ (m/s)	V_{amb} (m/s)	$V_{140\,^{o}C}$ (m/s)
CR	36.4	371.2	90.6	3020	2831	1294	1105
N	36.3	271.8	90.6	3356	3124	1485	1461
LN	36.0	265.1	90.6	3775	3624	1849	1536
GN	36.3	289.3	90.7	4535	4123	2212	1778
MA	36.2	265.9	95.5	4775	4341	1802	1647
G	36.4	256.1	95.0	3958	3800	2065	1863
GF	36.2	264.2	96.1	4004	3696	1961	1922
VTA	36.4	260.2	96.0	3556	3310	1745	1524
PX	36.2	294.9	90.5	3771	3352	1588	1534

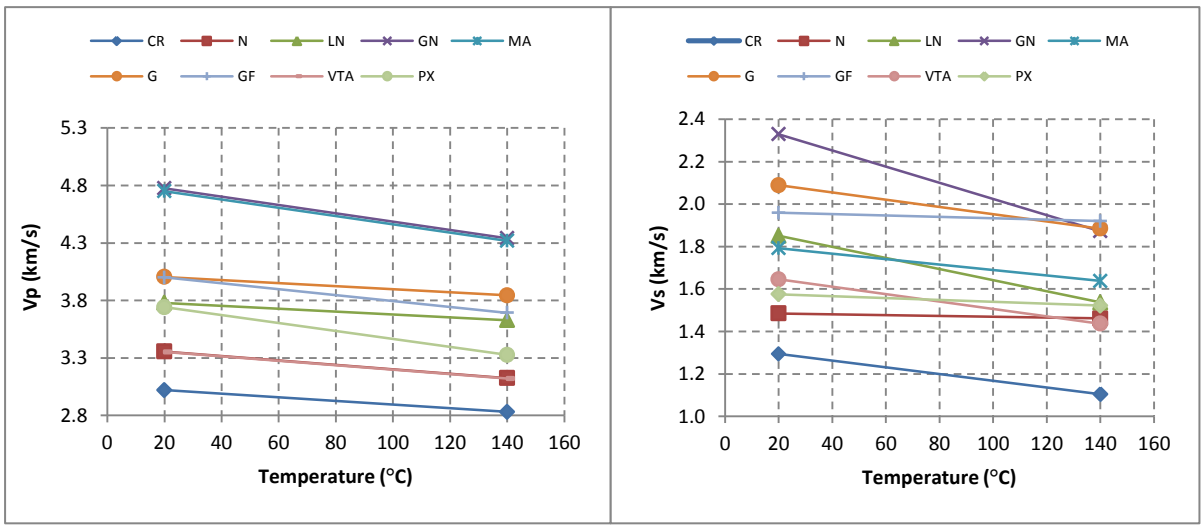


Figure 3.45: V_p and V_s versus temperature for temperature-ultrasonic tests

As observed in Table 3.12, the P- and S-wave velocities at ambient temperature are higher than at 140°C. This is attributed to the thermal expansion of the rocks.

The expansion of rocks causes further generation of micro-cracks, which results in the attenuation of waves. This attenuation delays the arrival of the ultrasonic signals. The increase in the wave travel time at 140°C translates to reduction in the P- and S-wave velocities (Figure 3.45).

3.8.2 Compression-ultrasonic tests

The compression-ultrasonic tests were done by the use of ultrasonic test apparatus in the MTS servo-controlled testing machine (Figure 3.46). The specimens were axially stressed at 10, 20 and 100 MPa (which fall within 50 to 75% of the UCS of most rocks tested except for chromitite) to examine the effect of loading on the P- and S-wave velocities. The axial stresses applied to chromitite are limited to 10, 20 and 30 MPa due to lower UCS of chromitite. The tests were repeated three times and the average travel times are provided in Table 3.13.

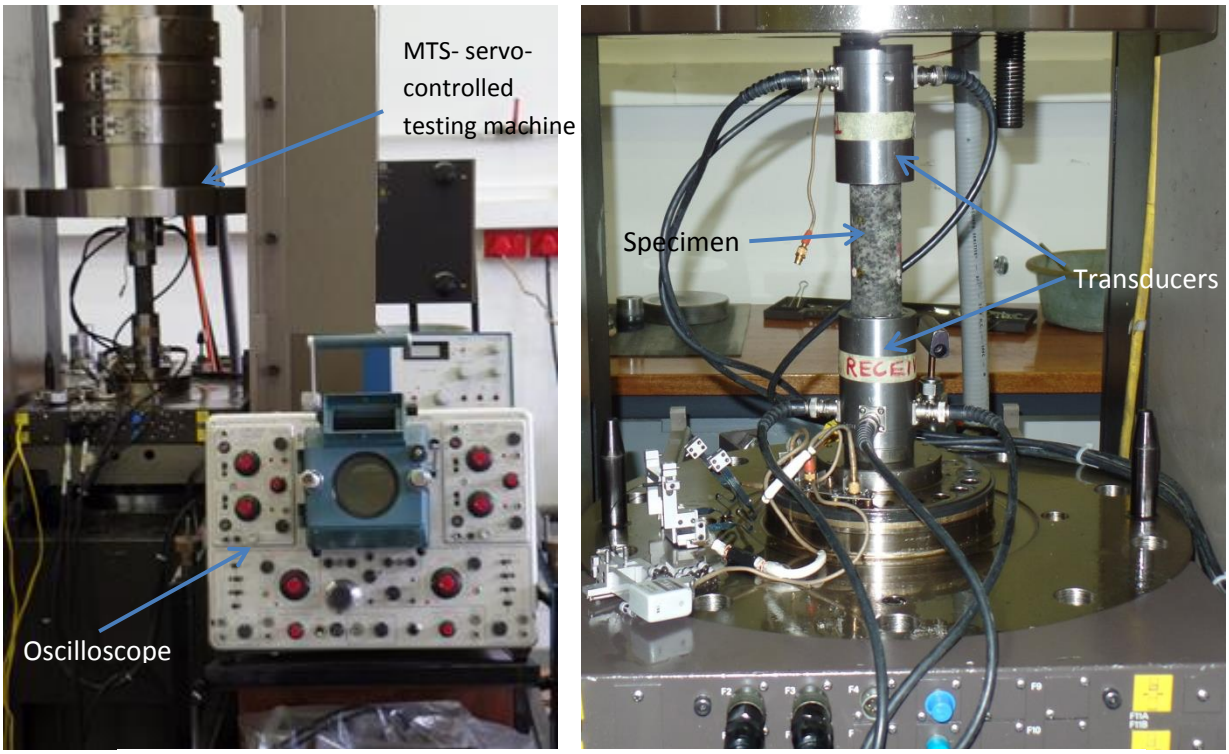


Figure 3.46: Experimental set-up compression-ultrasonic experiment

As Table 3.13 shows, increasing axial stress results in the reduction of the travel times. The plots of V_p and V_s versus axial stress for compression-ultrasonic tests are provided in Figure 3.47. It is obvious from these plots that V_p and V_s increases with increasing axial stress. This is caused by the compaction of the specimens along the direction of wave-velocity measurement due to the axial loading. As explained in the literature review section of this thesis, compaction lowers the arrival time and invariably increases wave velocities. It is noteworthy that the gradient of the graph (Figure 3.47) is higher between 10 and 20 MPa axial stress and reduces between 20 and 100 MPa. At lower axial stress, pre-existing microcracks and pores close up completely at the initial stages, as a result of the compaction and shortening of the specimen. The result is similar to the one obtained by Fortin *et al* (2011) although their test was under triaxial condition with 20 MPa confining pressure.

Examining the results of the temperature-ultrasonic and compression-ultrasonic experiments, one can conclude that temperature and stress have clear influence on P-, S-wave velocities. This would change the behaviour of rocks in the underground environment, particularly with increasing mining depth.

Table 3.13: P-and S-waves travel time for compression-ultrasonic tests

	P-wave						S-wave					
Specimens	T_{p1} (µs)	V_{p1} (m/s)	T_{p2} (µs)	V_{p2} (m/s)	T_{p3} (µs)	Vp_3 (m/s)	T_{s1} (µs)	Vs_1 (m/s)	T_{s2} (µs)	V_{s2} (m/s)	T_{s3} (µs)	Vs_3 (m/s)
CR	28	3236	27	3356	25	3624	65	1394	60	1510	55	1647
N	24	3775	23	3939	21	4314	50	1812	48	1888	43	2107
LN	20	4530	19	4768	17	5329	42	2157	40	2265	37	2449
GN	18	5039	17	5335	16	5669	38	2387	35	2591	34	2668
MA	19	5026	18	5306	17	5618	51	1873	45	2122	42	2274
G	20	4750	19	5000	17	5588	40	2375	36	2639	34	2794
GF	23	4178	21	4576	19	5058	46	2089	42	2288	38	2529
VTA	25	3840	24	4000	22	4364	51	1882	44	2182	40	2400
PX	23	3935	22	4114	20	4525	54	1676	48	1885	44	2057

Note: T_{p1}, T_{p2}, T_{p3} and T_{s1}, T_{s2}, T_{s3} are the P- and S-wave travel times for the applied stress of 10, 20 and 100 MPa, while V_{p1}, V_{p2}, V_{p3} and v_{s1}, V_{s2}, V_{s3} are the equivalent velocities.

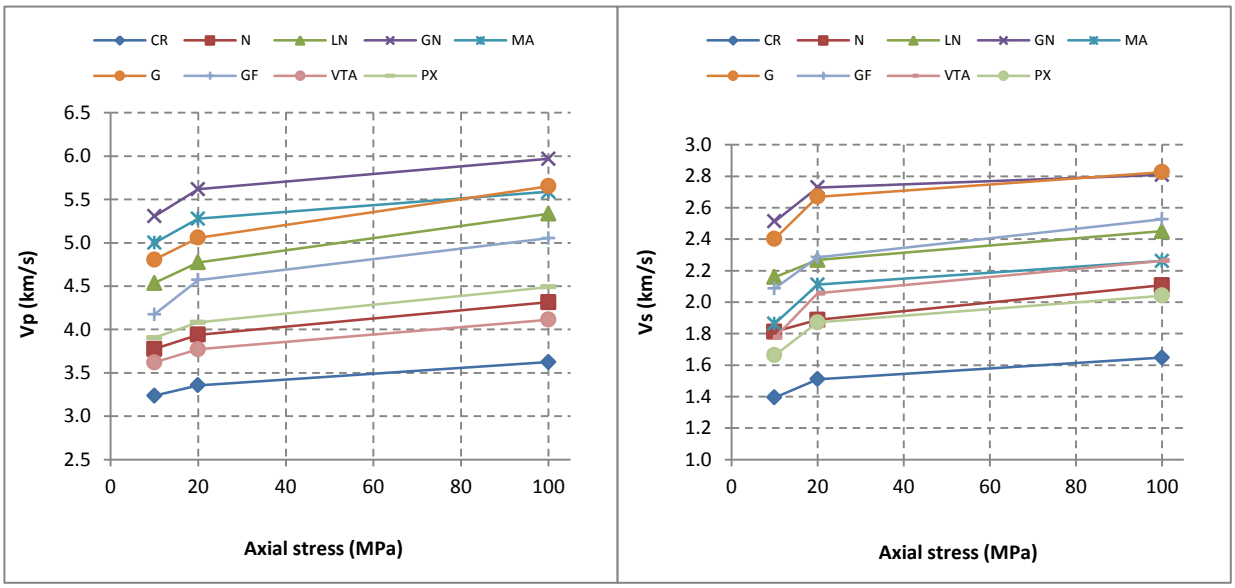


Figure 3.47: V_p and V_s versus axial stress for compression-ultrasonic tests

3.9 Chapter summary

In the laboratory experiments, 20°C is taken as the laboratory ambient temperature, while 50°C, 90°C, and 140°C correspond approximately to the virgin rock temperatures in the platinum mines at depths of 1073 m, 2835 m and 5037 m respectively. It is observed from the stress-strain behaviour of the samples tested under confined and unconfined conditions that increase in temperature results in the reduction of the Young's modulus and peak strength, while the dilation angle increases. P- and S-wave velocities of the specimens reduce with increasing temperature. Mathematical models, which relate reduction in Young's modulus and peak strength to temperature, were developed. Results show that any rock engineering design based on testing of rocks in ambient condition could be misleading as mining goes deeper, particularly in areas with high geothermal gradient. Therefore, it is imperative that rock engineers take cognizance of the influence of temperature in the design of deep mines in the future.